Publ. Astron. Soc. Japan (2018) 70 (1), R2 (1–44)
doi: 10.1093/pasj/psx123
Advance Access Publication Date: 2017 December 21
Invited Review

Invited Review

Cosmic magnetism in centimeter- and meter-wavelength radio astronomy

Takuya Akahori,[1,6,*] Hiroyuki Nakanishi,[1] Yoshiaki Sofue,[2] Yutaka Fujita,[3] Kiyotomo Ichiki,[4] Shinsuke Ideguchi,[5] Osamu Kameya,[6] Takahiro Kudoh,[7] Yuki Kudoh,[8] Mami Machida,[9] Yoshimitsu Miyashita,[10] Hiroshi Ohno,[11] Takeaki Ozawa,[12] Keitaro Takahashi,[10] Motokazu Takizawa,[13] and Dai G. Yamazaki[12,14]

[1]Graduate School of Science and Engineering, Kagoshima University, 1-21-35 Korimoto, Kagoshima, Kagoshima 890-0065, Japan
[2]Institute of Astronomy, The University of Tokyo, 2-21-1 Osawa, Mitaka, Tokyo 181-0015, Japan
[3]Graduate School of Science, Osaka University, 1-1 Machikaneyama, Toyonaka, Osaka 560-0043, Japan
[4]Kobayashi-Maskawa Institute, Nagoya University, Furo-cho, Chikusa-ku, Nagoya, Aichi 464-8602, Japan
[5]Department of Physics, UNIST, 50 UNIST-gil, Eonyang-eup, Ulju-gun, Ulsan 44919, Republic of Korea
[6]Mizusawa VLBI Observatory, National Astronomical Observatory of Japan, 2-12 Hoshigaoka, Mizusawa, Oshu, Iwate 023-0861, Japan
[7]Faculy of Education, Nagasaki University, 1-14 Bunkyo-machi, Nagasaki, Nagasaki 852-8521, Japan
[8]Faculty of Sciences, Chiba University, 1-33 Yayoi-cho, Inage-ku, Chiba, Chiba 263-8522, Japan
[9]Faculty of Sciences, Kyushu University, 744, Motooka, Nishi-ku, Fukuoka, Fukuoka 819-0395, Japan
[10]Department of Physics, Kumamoto University, 2-39-1 Kurokami, Kumamoto, Kumamoto 860-8555, Japan
[11]Tohoku Bunkyo College, 515 Katayachi, Yamagata, Yamagata 990-2316, Japan
[12]National Astronomical Observatory of Japan, 2-21-1 Osawa, Mitaka, Tokyo 181-8588, Japan
[13]Department of Physics, Yamagata University, 1-4-12 Kojirakawa-mach, Yamagata, Yamagata 990-8560, Japan
[14]Institute for University Education and Student Support, Ibaraki University, 2-1-1 Bunkyo, Mito, Ibaraki 310-8512, Japan

*E-mail: takuya.akahori@nao.ac.jp

Received 2017 May 12; Accepted 2017 September 5

Abstract

The magnetic field is ubiquitous in the universe. Though it plays an essential role in various astrophysical phenomena, its real origin and evolution are poorly known. This article reviews the understanding of the latest research concerning magnetic fields in the interstellar medium, the Milky Way Galaxy, external galaxies, active galactic nuclei, clusters of galaxies, and the cosmic web. Particularly, the review is concentrated in the achievements that have been provided by centimeter- and meter-wavelength radio observations. The article also introduces various methods for analyzing linear polarization data, including synchrotron radiation, Faraday rotation, depolarization, and Faraday tomography.

Key words: magnetic fields — methods: observational — polarization — radio continuum: general — techniques: polarimetric

1 Introduction

1.1 Magnetized universe

Magnetism plays substantial and often essential roles in astronomical objects. Most known celestial objects, the Earth, planets, the Sun, stars, interstellar space and clouds, the Milky Way Galaxy, galaxies, accretion disks and active galactic nuclei (AGN), and clusters of galaxies, are known to be magnetized. An exception might be the universe, where the cosmological isotropy principle has denied the cosmological-scale uniform field, which defines the north and south of the universe.

Magnetic-field strength, B, is roughly related to object size, R. Figure 1 depicts the global distribution of magnetic fields in the $\log B$–$\log R$ plot. An inverse relation, $B \sim (R/10\ \mathrm{kpc})^{-1}\ \mu\mathrm{G}$, is seen in the plot. It may also be noticed that the stars and pulsars roughly obey a squared-inverse relation, $B \sim 10^{12}(R/10\,\mathrm{km})^{-2}\,\mathrm{G}$, suggestive of frozen-in amplification during stellar collapses.

The strongest magnetic field observed so far in the universe reaches $\sim 10^{13}$ G, for magnetars among neutron stars. It is several orders of magnitude stronger than that achieved in laboratories. Magnetic fields in the interstellar medium (ISM) are on the order of several μG, and those in the intra-cluster medium (ICM) are often observed as having the strength of about a μG. The largest-scale, and hence the weakest, non-ordered magnetic fields may permeate the intergalactic medium (IGM) in the large-scale structure of the universe, whilst the study of them is a challenging subject for cosmology as well as for polarization technology in radio and far-infrared astronomy.

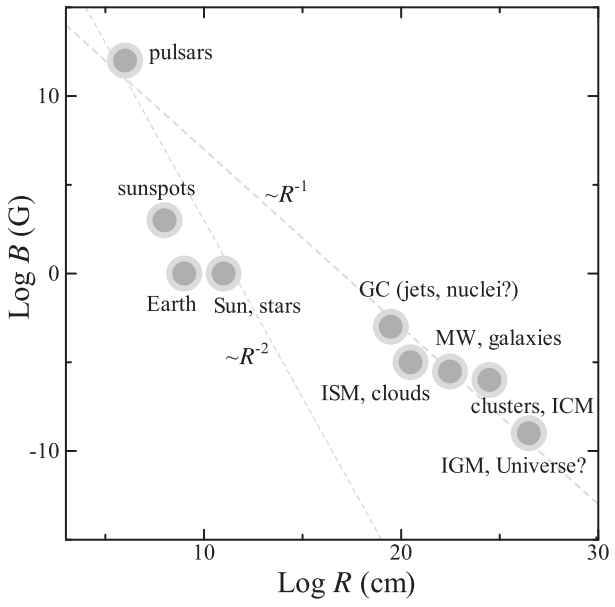

Fig. 1. Cosmic magnetic fields from the strongest to weakest, for compact to large-scale objects in the universe. The horizontal and vertical axes represent the object size, R, and the magnetic field strength, B, respectively. Dashed lines indicates power-laws with indices of -1 and -2.

Magnetic fields induce fundamental astrophysical processes such as particle acceleration, non-thermal radiation, polarization, and an impact on the activities of astronomical objects through field tension, reconnection, instability, and turbulence. This rich, diverse nature of magnetic phenomena is explained by common theories of magnetism, though various magnetic effects often make their appearance complicated.

Magnetic fields often help the research of other science subjects. For instance, understanding galactic magnetic fields (GMFs) assists the study of interstellar physics such as the formation of molecular clouds and stars. That for spiral galaxies assists the investigation of the origin of spiral arms. Magnetic fields around accretion disks assist high-energy cosmic jets. Inter-galactic magnetic fields (IGMFs) in the ICM and IGM are one of the keys to understanding the acceleration mechanism of the high-energy cosmic rays (CRs). The deepest magnetic fields may preserve information about the early universe, so that they will assist studies of the epoch of reionization, the cosmic microwave background polarization, and ultimately the inflation and the Big Bang of the universe.

1.2 History of cosmic magnetism research

The dawn of the contemporary magnetic view of the universe occurred when Karl G. Jansky by chance detected the Milky Way's radio emission in 1931. At the time, magnetic fields had been known only in the Earth and the Sun, and considered in high-energy astrophysics. The emission was proved to be originating from synchrotron radiation by the interaction of CR electrons and magnetic fields (Ginzburg & Syrovatskii 1965, 1969), revealing that the Milky Way is a huge magnetized disk embedded in a stellar gravitational potential.

Measurements of radio emission from the sky were extensively employed in the 1960s to estimate GMF strengths. Observers obtained the emission in meter wavelengths, and hence mostly synchrotron radiation. Radio intensities in the North Galactic Pole were used to estimate the mean radio emissivity in the galactic disk and were used to calculate field strength by assuming the equipartition of

energy densities between CRs and magnetic fields. The field strength in the solar neighborhood was known to be of the order of a few μG.

Linearly polarized radio waves provided progress in the study of cosmic magnetism in the 1970s. They supplied more fundamental information on magnetic fields such as three-dimensional configuration of magnetic lines of force. Galactic polarized emission indicated local field configurations, while Faraday depolarization made the analysis too complicated to reach a definite solution. Linear polarization observations of pulsars and extragalactic radio sources made the study of cosmic magnetism easier, more effective, and quantitative, and are today the major tool in studying the GMF by using their Faraday rotation measures (RM) (e.g., Gardner & Whiteoak 1966).

In the 1980s, linear polarization mapping of nebulae, galaxies, and radio lobes made it possible to derive their internal field configurations using Faraday *RM* analyses. The following, various topologies of GMF configuration in the Milky Way and external galaxies were recognized (Sofue et al. 1986):

- R: Ring, or toroidal field,
- BSS: BiSymmetric spiral field,
- ASS: AxiSymmetric spiral field, and
- V: Vertical, poloidal, or dipole field.

We follow these abbreviations in this paper. In addition, we also use

- MSS: Multi-Symmetric Spiral field, including QSS (Quadri-Symmetrical spiral),

which was proposed recently (Stepanov et al. 2008). One may also classify an irregular field configuration as

- T: Turbulent, flocculent, striated, ordered, or random field.

In the 1990s, through extensive development combined with sophisticated *RM* analyses of extragalactic radio sources, the study of cluster magnetic fields also became one of the most promising subjects.

In the 2000s, high-sensitivity direct polarization mappings of Abell clusters of galaxies revealed dynamical properties of the ICM. Polarization and magnetization stronger than that expected from some magneto-hydrostatic conditions were found. High-sensitivity observations also provided the *RM* grid, which is an *RM* map consisting of pixels of *RM*s for compact background polarized sources. The *RM* grids have revealed magnetic field structures of various objects including supernova remnants, the Milky Way, and external galaxies.

In the last decade, various new methods of *RM* analysis and techniques to measure radio polarization have been proposed and applied to a large number of radio sources. These include depolarization analysis and Faraday tomography, both of which deal with high frequency-resolution, multi-wavelength measurements of radio polarization.

1.3 Layout of this paper

The purpose of this article is to review the current understanding and achievements in the studies of astrophysical and astronomical magnetism. The paper concentrates on low-frequency radio astronomy at centimeter to meter wavelengths, because the wavelengths are suited to observe synchrotron radiation and Faraday rotation for many astronomical objects. Although it is obvious that high-frequency radio, optical, and infrared polarization observations are also the basic tools for investigating interstellar and galactic magnetic fields, these topics are beyond the scope of this paper. This paper also includes a thorough review of the various methods to analyze linear polarization data from radio observations, where sophisticated measurement technologies are often employed.

The sections in this review are as follows. Section 2 proposes a universal view on the theory of magnetism. Section 3 describes the methods to measure and analyze linearly polarized radio emission, particularly highlighting new methods such as depolarization and Faraday tomography. Section 4 summarizes magnetic fields in the ISM. Section 5 reviews magnetic fields in the Milky Way Galaxy. Section 6 highlights magnetic fields in external galaxies. Section 7 focuses on cosmic jets like AGN jets and activities related to magnetized nuclear disks. Section 8 describes new magnetic views of clusters of galaxies. Section 9 discusses cosmological implications of *RM* and linear polarization observations and analyses. Section 10 summarizes this paper.

2 Basic theory of cosmic magnetism

2.1 Overview of the origin and evolution

From the cosmic-scale point of view, the origin of cosmic magnetic fields can be roughly classified into two major ideas. One is the primordial origin; magnetic field was formed in the early universe and permeated the interstellar and intergalactic spaces. The primordial fields were incorporated in forming celestial bodies, and amplified during the contraction. The other is that the seed field was created inside a celestial body, e.g., a star, by a local electric current, and was amplified by dynamo and other amplification mechanisms. The amplified field was then expelled into circum-body, interstellar, and intergalactic spaces by winds, explosions, outflows, and so on. Here, the escaping flux may make larger-scale magnetic fields, though the mechanism, particularly its efficiency to create cluster-scale field in the

Hubble time, is not well examined. Also, there remains a question whether the mechanism can create regular configurations of magnetic fields in galaxies such as those in the BSS topology. Although primordial models suffer from a lack of smaller-scale irregular magnetic fields seen in various objects, the above difficulties may be avoided if there is a primordial field.

The following two major mechanisms have been considered for the amplification and regulation of cosmic magnetic fields. One is the primordial origin, where a field trapped in an object is wound up by the differential rotation of the object. The other is the dynamo mechanism provided by turbulence, convection, circulation, and/or differential rotation in a celestial object. Both are coupled to each other in most cases. Note that even without differential rotation, magnetic fields can be locally amplified by turbulence in the gas (ISM, IGM) and embedding objects (clouds, galaxies) due to their rotation and collisions. This mechanism can efficiently create strong fields on scales of the order of cloud sizes in the local interstellar space, keeping the global field configuration.

2.2 Magnetohydrodynamics and simulation

2.2.1 MHD equation

In the circumstances considered in this paper, magnetic fields are practically frozen into partially or fully ionized gas such as the ISM, ICM, and the gas of AGN jets, because of the large magnetic Reynolds number and small resistivity. Such magnetized gas can be treated under the approximation of magnetohydrodynamics (MHD). The MHD approximation is applicable even to interstellar "neutral" gas such as molecular and HI clouds, because a small fraction of particles ionized by CRs moves with the neutral gas by collisional resistivity.

The basic MHD equations are written as

$$\frac{\partial \rho}{\partial t} + \nabla \cdot (\rho \boldsymbol{v}) = 0, \tag{1}$$

$$\rho \frac{\partial \boldsymbol{v}}{\partial t} + \rho(\boldsymbol{v} \cdot \nabla)\boldsymbol{v} + \nabla P = \frac{1}{c}\boldsymbol{J} \times \boldsymbol{B} + \rho \boldsymbol{a}, \tag{2}$$

$$\frac{\partial U}{\partial t} + \nabla \cdot \left[\left(\frac{\rho \boldsymbol{v}^2}{2} + \frac{\gamma}{\gamma - 1} P \right) \boldsymbol{v} + \frac{c}{4\pi} \boldsymbol{E} \times \boldsymbol{B} \right] = \rho \boldsymbol{v} \cdot \boldsymbol{a} + Q, \tag{3}$$

$$\frac{\partial \boldsymbol{B}}{\partial t} = \nabla \times (\boldsymbol{v} \times \boldsymbol{B}) - c \nabla \times (\eta \boldsymbol{J}), \tag{4}$$

where U is the internal energy,

$$U = \frac{\rho v^2}{2} + \frac{B^2}{8\pi} + \frac{P}{\gamma - 1}, \tag{5}$$

$\boldsymbol{J}$ is the current density,

$$\boldsymbol{J} = \frac{c}{4\pi} \nabla \times \boldsymbol{B}, \tag{6}$$

and ρ, $\boldsymbol{v}$, P, c, $\boldsymbol{B}$, $\boldsymbol{a}$, γ, $\boldsymbol{E}$, and η are the density, velocity, gas pressure, light speed, magnetic field, external force, specific heat ratio, electric field, and resistivity, respectively.

The characteristic condition of the MHD approximation is that a typical timescale of plasma dynamics is longer than a period of plasma oscillation. In other words, the MHD approximation is applicable if the size of the system is much larger than the mean free path in the direction perpendicular to magnetic field. The plasma's effective mean free path is determined by the Larmor radius, which is in most cases smaller than the system size even in galactic halos and galaxy clusters possessing very weak magnetic fields and large mean free paths. Therefore, the MHD approximation is a reasonable assumption for the ISM and ICM. The MHD condition is analogous to a fluid approximation for the fluid dynamics, i.e., the scale length is much larger than the mean free path and the typical timescale of the system is much longer than the collision timescale.

2.2.2 History and issues of MHD simulation

The first application of MHD simulation to astrophysical magnetic phenomena concerned magnetic reconnection during solar flares (e.g., Ugai & Tsuda 1977). MHD simulations were then applied to the Parker instability (Parker 1971) in order to understand protostar jets and molecular-cloud formation (e.g., Uchida & Shibata 1984; Matsumoto et al. 1988). In the 1990s, the importance of the magnetic instability was pointed out in differentially rotating systems (Balbus & Hawley 1991), and several authors have studied it in accretion disks (e.g., Hawley et al. 1995).

In the 2000s, relativistic MHD codes were developed (Koide et al. 2002), and general relativistic MHD codes (GRMHD) have been written (e.g., Gammie et al. 2003). In simulations of supernovae, further advanced GRMHD codes are developed, which include various physical processes such as the Einstein equation, self-gravity of the system, neutrino transports, and so on (e.g., Shibata & Sekiguchi 2005). Radiative transfer has also been incorporated in MHD codes in the optically-thick regime (e.g., Turner 2004).

As for larger scales, MHD simulations of the cosmological structure formation were performed both with a grid-base code (uniform-grid or adoptive mesh refinement) and smoothed particle hydrodynamics (e.g., Ryu et al. 2008; Dubois & Teyssier 2008; Dolag et al. 2008; Dolag & Stasyszyn 2009; Xu et al. 2009; Donnert et al. 2009; Schleicher et al. 2010; Stasyszyn et al. 2010; Marinacci et al. 2015). The galactic magnetic fields have been studied

under the cosmological structure formation (e.g., Beck et al. 2013a; Pakmor et al. 2014).

Nowadays, several open MHD codes for astrophysics are available, e.g., Zeus (Stone & Norman 1992), Athena (Stone et al. 2008), CANS+ (Matsumoto et al. 2016), and so on. An MHD simulation has become a commonly used method in astrophysics, and has been one of the most powerful tools to study magnetic fields in the universe. On the other hand, modern simulations get complicated by incorporating many astrophysical processes such as star formation, supernova, galaxy formation, AGN feedback, and so on, as well as microscopic physics such as CR acceleration and plasma conduction/dissipation. These factors can also affect the magnetic field evolution and structure. Moreover, they increase numerical uncertainty. It is thus necessary for modern MHD simulations to verify the numerical result by, for example, performing the same simulations with different spatial resolutions.

Finally, a large computational cost is an unavoidable problem when one attempts to carry out a massive simulation. For example, a three-dimensional, radiative MHD simulation of an accretion disk was recently achieved (Takahashi et al. 2016). The simulation considered 4.5 million numerical grid points, and took 0.5 million time-steps, or more than one month of CPU hours, with 512 cores of K-computer in RIKEN, one of the world's top 10 supercomputers in 2017. Even with such a cost, this process simulated disk evolution for only 0.3 s in real time. Therefore, it is critical in modern MHD simulations to not only develop high-precision and robust codes but also accelerate the calculation.

2.3 Dynamo and magnetic field

Astrophysical fluid is mostly ionized or partially ionized, including neutral gas such as H I and molecular clouds, and hence electrically conducting. Its flow tends to be magnetized spontaneously by self-excited electric current. If the flow is magnetized and the field tension is not too strong to prevent the flow motion itself, the flow drags magnetic fields, stretches them, and increases the magnetic flux density—this is called dynamo action. This process converts part of the kinetic energy into magnetic energy.

Dynamo action produces magnetic energy on scales (i) smaller than the energy-carrying eddy scale (small-scale dynamo), and (ii) larger than the energy-carrying eddy scale (large-scale dynamo). The small-scale dynamo basically produces isotropic structure, but no helicity, while the large-scale dynamo can form anisotropy and helicity, which are further significant in stratified media such as a galactic gaseous disk.

In the early 1900s, it was already recognized that regular (laminar) flow becomes irregular (turbulent) flow in incompressible viscous fluids (e.g., liquid water) with a large Reynolds number,

$$Re = \frac{UL}{\nu}, \tag{7}$$

where U and L are the characteristic velocity and length, and ν is the kinematic viscosity coefficient. Kolmogorov (1941) proposed that the statistical nature of high-Re flow motions is locally isotropic, similar, and universal in the inertial range ($L_{\rm d} \ll L \ll L_{\rm f}$), where the subscripts f and d refer to the forcing (energy injecting) and energy-dissipating scales, respectively. With this hypothesis, dimensional analysis gives the flow kinetic energy spectrum,

$$E(k) = C_{\rm K}\varepsilon^{2/3}k^{-5/3}, \tag{8}$$

where ε is the energy dissipation rate, $k = 2\pi/l$ is the wavenumber for the physical scale l, and $C_{\rm K}$ is the normalization constant. Assuming that the dissipation-scale wavenumber, $k_{\rm d}$, is much larger than the forcing-scale wavenumber, $k_{\rm f}$, i.e., $k_{\rm d} \gg k_{\rm f}$, the Reynolds number can be written as

$$Re \approx \frac{3\sqrt{3}}{2} C_{\rm K}^{3/2} \left(\frac{k_{\rm d}}{k_{\rm f}}\right)^{4/3} \tag{9}$$

(see, e.g., Brandenburg & Nordlund 2011). The above nature can be summarized as follows: a flow with large Re easily results in turbulence and such a flow has a broad ($k_{\rm d}/k_{\rm f} \propto Re^{3/4}$) inertial range.

In addition to the Reynolds number $Re = u_{\rm rms}/(\nu k_{\rm f})$, the magnetic Reynolds number $Re_{\rm M} = u_{\rm rms}/(\eta k_{\rm f})$ is another important parameter on the transition from laminar to turbulent flows. Here $u_{\rm rms}$ is the characteristic rms velocity of turbulence. Laboratory experiments show that the laminar/turbulent transition occurs around $Re_{\rm crit} \sim 2000$–4000, where $Re_{\rm crit}$ is the critical Reynolds number. Meanwhile, the critical magnetic Reynolds number, $Re_{\rm M,crit}$, depends on the magnetic Prandtl number $Pr_{\rm M} = \nu/\eta = Re_{\rm M}/Re$. Numerical simulations of small-scale dynamo suggest that $Re_{\rm M,crit}$ is $\sim$50–500 and rather constant for $Pr_{\rm M} > 1$ (the resistive scale lies in the viscous scale) (Schekochihin et al. 2005). As $Pr_{\rm M}$ decreases below unity (the resistive scale lies in the kinetic inertial range), the range of laminar flows (i.e., $Re_{\rm M,crit}$) sharply increases.

In small-scale dynamo, eddy cascading proceeds from larger to smaller eddies, and terminates at the smallest spatial scale at which kinetic energy is dissipated into thermal energy due to the viscosity and/or resistivity. Here, following the same analogy of the kinetic inertial range $k_\nu/k_{\rm f} \approx Re^{3/4}$, the magnetic inertial range depends on $k_\eta/k_{\rm f} \approx Re_{\rm M}^{3/4}$.

Magnetic fields at smallest scales first grow exponentially by the stretching of field lines therein. Then, larger-scale magnetic fields are amplified like an inverse cascade. The growth proceeds gradually and is called the linear growth. Finally, dynamo amplification is saturated when the magnetic energy and kinetic energy are comparable to each other. The timescale and efficiency of dynamo amplification depend on various physical parameters such as not only Re, $Re_{\rm M}$, and $Pr_{\rm M}$, but also the plasma β (the ratio between thermal pressure and magnetic tension) and the rms Mach number (the ratio between flow velocity and sound velocity).

As for large-scale dynamo, its onset occurs on scales with very large magnetic Reynolds numbers and is essentially independent of $Pr_{\rm M}$. A well-known large-scale dynamo is the Parker dynamo mechanism in a galactic disk. Under the gravity perpendicular to the disk, the mechanism inflates a perturbed GMF into the halo and forms a Ω-shape magnetic-field. As a result of the buoyancy and expansion, as well as the angular momentum conservation, it begins to rotate in the opposite direction of the galactic rotation, where the differential rotation of the disk and local epicyclic motion are the driving force, which stretches the field lines, and increases the net field strength. In this mechanism, the local field strength increases, but averaged field strength and configuration do not change. The convective instability plays a key role in evolution of large-scale dynamo (e.g., Käpylä et al. 2008). Also, the magneto-rotational instability (MRI) acts similarly to the Parker instability for amplifying the local field strengths (e.g., Machida et al. 2013), while it does not change the global configuration.

2.4 Turbulence and magnetic field

2.4.1 MHD turbulence

The classical theory of hydrodynamic turbulence is expanded to MHD. The induction equation (4) introduces the magnetic diffusivity (resistivity), η, and the magnetic Prandlt number, $Pr_{\rm M} = \nu/\eta$, which satisfy $\eta \ll \nu$ and $Pr_{\rm M} \gg 1$ in the ideal MHD approximation. In hydrodynamic turbulence, kinetic energy is transferred due to eddy cascade. In MHD, on the other hand, such energy transfer is reduced by the ratio of a parallel Alfvén transit time $(1/k_{||}v_{\rm A})$ for the Alfvén velocity,

$$v_{\rm A} = \frac{B_{||}}{\sqrt{4\pi\rho}} \tag{10}$$

(ρ is the plasma mass density), to a perpendicular eddy shearing rate $(l_\perp/v_\perp)$. This Alfvén effect is important in a magnetized system (e.g., Diamond et al. 2010). For a weakly magnetized isotropic cascade, the energy spectrum is rescaled as,

$$E(k_\perp) = C_{\rm IK}(\varepsilon v_{\rm A})^{1/2}k^{-3/2}, \tag{11}$$

where $C_{\rm IK}$ is the normalization constant (Iroshnikov 1964; Kraichnan 1965). As for a strongly magnetized system in which there is a large-scale anisotropy, the relation is rescaled as

$$E(k_\perp) = C_{\rm GS}(\varepsilon k_{||}v_{\rm A})^{1/2}k_\perp^{-2}, \tag{12}$$

where $C_{\rm GS}$ is the normalization constant (Goldreich & Sridhar 1995, 1997). Transition between strongly and weakly magnetized systems appears when the parallel Alfvén wave transit time is equal to the perpendicular eddy turnover time (the critical balance). The energy spectrum under the critical balance can be written as

$$E(k_\perp) = C_{\rm GS}\varepsilon^{2/3}k_\perp^{-5/3}. \tag{13}$$

Interestingly, the slope is identical to the Kolmogorov slope (e.g., Diamond et al. 2010).

2.4.2 Structure function and intermittency

The structure function (SF) is useful to quantify the amplitude of spatial structures at the scale $r = |\boldsymbol{r}|$. For a physical quantity $A(\boldsymbol{x})$ at $\boldsymbol{x}$, the nth order SF, $S_n(r)$, is defined as the nth order statistical moment of the difference:

$$S_n(r) = \langle \delta A(r)^n \rangle, \tag{14}$$

$$\delta A(r) = |A(\boldsymbol{x}+\boldsymbol{r}) - A(\boldsymbol{x})|, \tag{15}$$

where $\langle ... \rangle$ means the ensemble average. We often quantify the SF exponent, ξ_n, assuming $S_n(r) \propto r^{\xi_n}$.

For example, the velocity SF is given by

$$S_n(r) = \langle \delta v(r)^n \rangle = C_n \varepsilon^{n/3} r^{n/3}, \tag{16}$$

where C_n is the normalization constant. The equation $\xi_n = n/3$ appears in Kolmogorov turbulence as follows (e.g., Diamond et al. 2010). In a sequential cascading of eddies, the mth sequence takes place during the eddy turnover time $t_m = l_m/v_m$, and its energy is transferred to the energies of eddies in the next sequence with $\varepsilon_m \sim E_m/t_m \sim (v_m)^3/l_m$. For high-$Re$ incompressible fluid, the momentum equation becomes a first-order differential equation and it can be parametrized such as $x \to \delta\hat{x}$, $t \to \delta^{1-\alpha/3}\hat{t}$, and $v \to \delta^{\alpha/3}\hat{v}$, where α is an arbitrary scaling exponent. Thus, the velocity SF, $\langle \delta v(r)^n \rangle$, gives $\xi_n = n\alpha/3$. Since energy transfer from large to small scales is spatially isotropic and ε is scale invariant, $\varepsilon_m/\varepsilon_0 \sim (v_m^3/l_m)/(v_0^3/l_0) = \delta_m^\alpha/\delta_m = \delta_m^{\alpha-1}$ and $\alpha = 1$. Therefore, $\xi_n = n/3$.

In generic turbulence, energy-transfer is not spatially isotropic, and intermittent energy-transfer exists in space and time, i.e., $\xi_n \neq n/3$. Based on experiments and simulations, the phenomenological She–Leveque relation is proposed:

$$\xi_n = \frac{n}{9} + C\left[1 - \left(1 - \frac{2/3}{C}\right)^{n/3}\right] \tag{17}$$

(She & Leveque 1994; Brandenburg & Nordlund 2011). Here, C is interpreted as the co-dimension of the dissipative structures; $C \sim 2$ with one-dimensional tube-like dissipative structures for weakly compressible or incompressible turbulence, and $C \sim 1$ with two-dimensional sheet-like dissipative structures for compressible or highly supersonic turbulence.

In MHD, the relation between the SF exponent and turbulence properties is still under discussion. For instance, the Iroshnikov–Kraichnan scaling gives the exponent of the longitudinal velocity SF as $\xi_n = n/4$. MHD turbulence simulations with modest, $Pr_{\rm M} \sim 1$, indicated an energy spectrum close to the Iroshnikov–Kraichnan relation, but showed $\xi_n = n/3$ (Haugen et al. 2003).

3 Method and analysis of measurements of magnetic fields

3.1 Measurement of Stokes parameters

If an electromagnetic wave travels in the z-direction in the Cartesian three-dimensional coordinates, electric and magnetic fields oscillate in the xy plane. The functions of the electric field can be defined as

$$E_x(t) = E_{x0}(t)e^{i\{2\pi\nu t + \delta_x(t)\}}, \tag{18}$$

$$E_y(t) = E_{y0}(t)e^{i\{2\pi\nu t + \delta_y(t)\}}, \tag{19}$$

where the phase difference is $\delta_x(t) - \delta_y(t) = n\pi$ (n: integer) for a linearly polarized wave and $\pm\pi/2 + 2n\pi$ for a circularly polarized wave.

Radio receivers are generally designed to detect either linear or circular polarization. Orthogonal dipoles detect horizontal and vertical components of linearly-polarized radio waves. The Stokes parameters are given by time-averaged auto-correlation and cross-correlation of $E_x(t)$ and $E_y(t)$ as expressed below using the following matrix:

$$\begin{pmatrix} I \\ Q \\ U \\ V \end{pmatrix} = \begin{pmatrix} 1 & 0 & 0 & 1 \\ 1 & 0 & 0 & -1 \\ 0 & 1 & 1 & 0 \\ 0 & -i & i & 0 \end{pmatrix} \begin{pmatrix} \langle E_x E_x^* \rangle \\ \langle E_x E_y^* \rangle \\ \langle E_y E_x^* \rangle \\ \langle E_y E_y^* \rangle \end{pmatrix}. \tag{20}$$

Here, $\langle E_i E_j^* \rangle$ represents the auto/cross correlation. The Stokes parameter I corresponds to the total intensity of radiation. Fractions of $\sqrt{Q^2 + U^2}/I$ and V/I indicate degrees of linear and circular polarization, respectively. The polarization angle χ is given by $\chi = \arctan(U/Q)/2$.

Similarly, right-handed and left-handed helical antennae detect right and left circularly-polarized radio waves. Defining the electric field of right and left circularly-polarized components as $E_r(t)$ and $E_l(t)$, Stokes parameters are given as follows:

$$\begin{pmatrix} I \\ Q \\ U \\ V \end{pmatrix} = \begin{pmatrix} 1 & 0 & 0 & 1 \\ 0 & 1 & 1 & 0 \\ 0 & i & -i & 0 \\ -1 & 0 & 0 & 1 \end{pmatrix} \begin{pmatrix} \langle E_r E_r^* \rangle \\ \langle E_r E_l^* \rangle \\ \langle E_l E_r^* \rangle \\ \langle E_l E_l^* \rangle \end{pmatrix}. \tag{21}$$

These expressions show that either a diagonal linearly polarized feed or a diagonal helical feed can measure all Stokes parameters. The linearly polarized feed is widely used to realize broad-band observation (Das et al. 2010) and it is sensitive to the circular polarimetry, which is necessary to detect the Zeeman effect (Mizuno et al. 2014). If an antenna mount is alt-azimuth, circular polarization is advantageous because it is not necessary to rotate the feed even though the parallactic angle of the object changes during an observation (Conway & Kronberg 1969).

The above description of the derivation of polarimetry is an ideal case where no leakage exists between two polarized components. However, there is non-negligible leakage between two polarized components in an actual observation, which has to be eliminated. Measured signal voltages v_x' and v_y' are written with intrinsic values v_x and v_y as

$$\begin{aligned} v_x' &= v_x + D_x v_y, \\ v_y' &= v_y + D_y v_x, \end{aligned} \tag{22}$$

where subscripts x and y denote horizontal (h) and vertical (v) polarizations, or right-hand (r) and left-hand (l) polarizations, respectively. The second terms including D_x and D_y are called D-terms, and indicate leakage. These D-terms are calibrated by observing calibrators that have well-known polarizations.

3.2 Synchrotron radiation and Faraday rotation

Synchrotron radiation and Faraday rotation are conventional tools of radio astronomy used to study cosmic magnetic fields (for a text book, see Rybicki & Lightman 1979). Synchrotron radiation is emitted from relativistic charged particles gyrating around magnetic fields. Assuming isotropic distribution of relativistic electrons and their

energy spectrum of the form,

$$N(\gamma)d\gamma = \mathcal{N}(r)\gamma^{-p}d\gamma, \tag{23}$$

where γ is the Lorentz factor, $\mathcal{N}(r)$ is the proportional constant at the position r, and p is the spectral index, the synchrotron emissivity can be written as

$$\epsilon(r) \propto \mathcal{N}(r)B_{\perp}(r)^{(1+p)/2}\nu^{(1-p)/2}, \tag{24}$$

where $B_{\perp}$ is the strength of magnetic fields perpendicular to the line-of-sight (LOS) and ν is the frequency. The synchrotron intensity at frequency ν is often fitted with a power-law form:

$$I_{\nu} \propto \nu^{-\alpha}. \tag{25}$$

The spectral index is thus related to the electron energy spectral index as $p = 2\alpha + 1$.

Assuming a reasonable distribution of $\mathcal{N}(r)$ and the size of emission region, we can estimate the value of $B_{\perp}$ and its orientation on the sky from the synchrotron intensity. The equipartition between total energy densities of CRs and that of the magnetic field ($\epsilon_B = \epsilon_{\rm CR}$) is often used, and the magnetic field strength is estimated as follows (e.g., Akahori et al. 2016):

$$B_{\rm eq}[{\rm G}] = \frac{4\pi(2\alpha+1)(K_0+1)I_{\nu}E_{\rm p}^{1-2\alpha}(\nu/2c_1)^{\alpha}}{(2\alpha-1)c_2c_4}, \tag{26}$$

where

$$c_1 = \frac{3e}{4\pi m_{\rm e}^3c^5} = 6.26428\times10^{18}\ [{\rm erg}^{-2}\ {\rm s}^{-1}\ {\rm G}^{-1}], \tag{27}$$

$$c_2 = \frac{c_3}{4}\frac{p+7/3}{p+1}\Gamma\left[\frac{3p-1}{12}\right]\Gamma\left[\frac{3p+7}{12}\right], \tag{28}$$

$$c_3 = \frac{\sqrt{3}e^3}{4\pi m_{\rm e}c^2} = 1.86558\times10^{-23}\ [{\rm erg\ G}^{-1}\ {\rm sr}^{-1}], \tag{29}$$

$$c_4 = [\cos i]^{(p+1)/2}, \tag{30}$$

K_0 is the ratio of the number densities of protons and electrons, $E_{\rm p}$ is the proton rest energy (938.28 MeV), l is the LOS length, i is the inclination angle of the magnetic field with respect to the sky plane ($i = 0$ in the case of face-on view), e is the elementary charge, $m_{\rm e}$ is the electron mass, and c is the velocity of light.

When a linearly-polarized electromagnetic wave passes through magneto-ionic media, its polarization angle rotates as

$$\chi(\lambda^2) = \chi_0 + RM\lambda^2, \tag{31}$$

where χ_0 is the initial polarization angle and λ is the wavelength. This phenomenon is called Faraday rotation and the coefficient RM is the rotation measure;

$$RM\ ({\rm rad\ m}^{-2}) \approx 811.9\int\left(\frac{n_{\rm e}}{{\rm cm}^{-3}}\right)\left(\frac{B_{||}}{\mu{\rm G}}\right)\left(\frac{dr}{\rm kpc}\right), \tag{32}$$

where $n_{\rm e}$ is the density of free electrons, $B_{||}$ is the strength of magnetic fields parallel to the LOS, and RM is defined to be positive if the magnetic field points toward the observer. Therefore, once we observe a polarized source and obtain the RM, we can estimate the integral of $n_{\rm e}B_{||}$. RM can be obtained if polarization angles are measured at more than one wavelength.

In summary, we can guess the magnetic field parallel to the LOS from the RM. Considering inverse Faraday rotation with the RM, the intercept of χ–λ^2 plots gives the intrinsic polarization angle. We can guess the magnetic field perpendicular to the LOS from the synchrotron intensity and the intrinsic polarization angle. Synchrotron radiation is hence an important observable for constructing the three-dimensional magnetic field model. However, only an average over the emission region is obtained and the spatial distribution along the LOS is difficult to evaluate.

3.3 Depolarization

Depolarization is a phenomenon in which we observe a polarization degree that is weaker than that at the origin. If polarizations with different polarization angles are observed simultaneously, depolarization takes place. Such a situation appears in several ways and is categorized as follows (see, e.g., Sokoloff et al. 1998 for more details):

- **Wavelength independent depolarization:** Consider an observation of a magnetized medium emitting polarization; depolarization can take place if the magnetic fields perpendicular to the LOS are not aligned with each other in the medium. This depolarization does not depend on the wavelength of polarization.
- **Differential Faraday rotation depolarization:** In the above situation, even if the magnetic fields perpendicular to the LOS are aligned with each other, depolarization can take place when non-zero RM, i.e., the net magnetic fields parallel to the LOS, is present along the LOS in the medium. In such a case, polarizations emitted at different depths experience different Faraday rotation, so that they can cancel each other out.

- **Beam depolarization:** If RM is not uniformly distributed in the medium and/or in front of the medium, depolarization can take place because polarizations inside an observing beam experience different Faraday rotation. This depends on the observing beam size.
- **Bandwidth depolarization:** The degree of Faraday rotation depends on the wavelength. Therefore, depolarization can take place when one integrates broad-band polarizations.

Burn (1966) formulated depolarization in several simple situations. For example, in the case of matter with uniform electron density and uniform magnetic fields, the polarization degree Π of that matter for a specific LOS can be written as

$$\Pi(\lambda^2) = \Pi_0(\lambda^2)\frac{\sin\left(RM\lambda^2\right)}{RM\lambda^2}\exp 2i\left(\chi_0 + \frac{1}{2}RM\lambda^2\right), \quad (33)$$

where Π_0 is the intrinsic polarization degree. This case is differential Faraday rotation depolarization.

Another example is beam depolarization. We suppose that RM distribution inside a beam area follows a Gaussian with the standard deviation of σ_{RM}. In the case where this RM source itself is an emitter of polarization, Π can be written as

$$\Pi(\lambda^2) = \Pi_0(\lambda^2)\frac{1-\exp\left(-2\sigma_{RM}^2\lambda^4\right)}{2\sigma_{RM}^2\lambda^4}, \quad (34)$$

and is called internal Faraday dispersion depolarization. Otherwise, in the case where this RM source is a foreground of a polarized source, Π can be written as

$$\Pi(\lambda^2) = \Pi_0(\lambda^2)\exp\left(-2\sigma_{RM}^2\lambda^4\right), \quad (35)$$

and is called external Faraday dispersion depolarization.

Figure 2 shows the Burn law (Arshakian & Beck 2011), which indicates that the degree of depolarization depends on the frequency. Wide frequency coverage is hence essential to capture the feature of depolarization. The fact that depolarization is weaker at higher frequencies implies that the observed polarization degree can be larger for higher redshift sources, because depolarization happens at their rest-frame (higher) frequencies.

Depolarization is thought to have the capability to inform three-dimensional magnetic field structures both along the LOS and within an observing beam. For example, depolarization depends on the amount of magnetic helicity, which has been claimed to be a tool for determining magnetic helicity in galaxies (e.g., Oppermann et al. 2011; Brandenburg & Stepanov 2014). However, it is hard to recognize depolarization without wideband polarimetric data, which are not easy to obtain. Therefore, application of depolarization diagnostics to real observations has been limited. Future radio telescopes should facilitate wideband polarimetric observations and break through the situation in order to advance the study of cosmic magnetism.

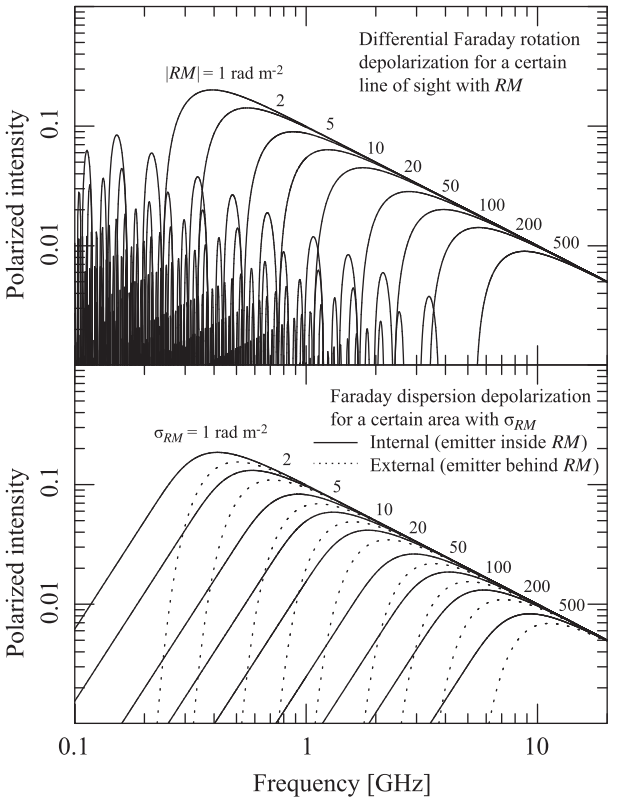

Fig. 2. Depolarization of differential Faraday rotation (top) and dispersion (bottom). See Arshakian and Beck (2011) for the original figures and details.

3.4 Faraday tomography

Faraday tomography is a decomposition technique proposed by Burn (1966) and extended by Brentjens and de Bruyn (2005). An observed polarized intensity is an integration of the synchrotron emissivity $\epsilon(r)$ along the LOS, and it can be decomposed as

$$P(\lambda^2) = \int_0^\infty \varepsilon(r)e^{2i\chi(r,\lambda^2)}dr = \int_{-\infty}^{\infty} F(\phi)e^{2i\phi\lambda^2}d\phi, \quad (36)$$

where

$$\chi(r,\lambda^2) = \chi_0(r) + \phi(r)\lambda^2, \quad (37)$$

is the polarization angle at an observer, $\chi_0(r)$ is the intrinsic polarization angle at r, and $\phi(r)$ is the Faraday depth in rad m^{-2}. $F(\phi) \equiv \varepsilon(\phi)e^{2i\chi_0(\phi)}dr/d\phi$ is the Faraday dispersion function (FDF) or the Faraday spectrum, which represents the sum of the emissivity through the regions with a specific value of ϕ. Note that we changed the integration variable from r to $\phi(r)$, resulting in the form of Fourier transformation with conjugate variables ϕ and λ^2.

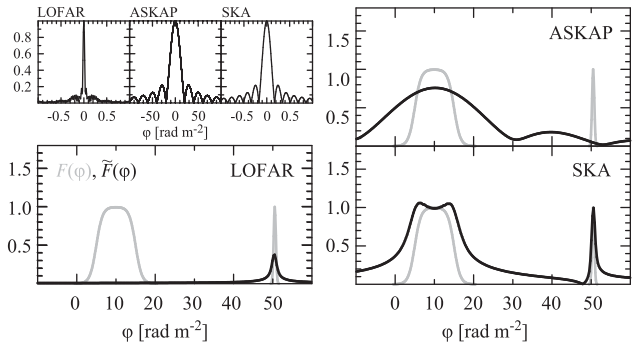

Fig. 3. (Top left) Rotation measure spread function. (Other panels) Model (gray) and reconstructed (black) Faraday spectra (Akahori et al. 2014b). Frequency coverages of LOw Frequency ARay (LOFAR) and Australian SKA Pathfinder (ASKAP) are only sensitive to thin (compact source) and thick (diffuse source) Faraday structures, respectively, while seamless, broad bandwidth of the Square Kilometre Array (SKA) can provide sensitivities for *RM* structures of O(1–1000) rad m^{-2}.

In theory, $F(\phi)$ can be precisely derived from $P(\lambda^2)$ by the inverse Fourier transformation. This is not the case, however, because the observable $P(\lambda^2)$ is available only for a limited range of λ^2. Using a window function $W(\lambda^2)$ for observable wavelengths, the reconstructed FDF, $\tilde{F}(\phi)$, can be written as

$$\tilde{F}(\phi) = \frac{1}{\pi}\int_{-\infty}^{\infty} W(\lambda^2)P(\lambda^2)e^{-2i\phi\lambda^2}d\lambda^2. \tag{38}$$

Using the convolution theorem, this equation becomes

$$\tilde{F}(\phi) = K^{-1}R(\phi) * F(\phi), \tag{39}$$

$$R(\phi) = K\int_{-\infty}^{\infty} W(\lambda^2)e^{-2i\phi\lambda^2}d\lambda^2, \tag{40}$$

$$K = \left[\int_{-\infty}^{\infty} W(\lambda^2)d\lambda^2\right]^{-1}, \tag{41}$$

where $R(\phi)$ is called the rotation measure spread function (RMSF).

If the window function is unity for all λ^2, $R(\phi)/K$ is reduced to the delta function $\delta(\phi)$ and the reconstruction is perfect. However, in reality, $P(\lambda^2)$ is unphysical for negative values of λ^2, and coverage of positive λ^2 is imperfect in observation. Thus, the RMSF has a finite width depending on wavelength coverage, as shown in figure 3.

The full width at half maximum (FWHM) of the RMSF corresponds to the resolution in the Faraday depth space. Considering the case where $W(\lambda^2) = 1$ for $\lambda^2_{\rm min} \le \lambda^2 \le \lambda^2_{\rm max}$ and otherwise $W(\lambda^2) = 0$, the FWHM is given by

$$\mathrm{FWHM\,(rad m^{-2})} = \frac{2\sqrt{3}}{\Delta\lambda^2(\mathrm{m}^2)}. \tag{42}$$

This indicates that the resolution is determined by the λ^2-space coverage, $\Delta\lambda^2 = \lambda^2_{\rm max} - \lambda^2_{\rm min}$. In particular, going up to a longer wavelength expands the λ^2 coverage effectively, though it tends to suffer from depolarization more seriously. Differential Faraday rotation depolarization can be significant when the polarization angle rotates by π within a source extended in Faraday depth space. Hence the maximum observable width in the Faraday depth space is

$$L_{\phi,\rm max}(\mathrm{rad\,m^{-2}}) \approx \frac{\pi}{\lambda^2_{\rm min}(\mathrm{m}^2)}. \tag{43}$$

In order to make Faraday tomography feasible, the two frequency conditions above need to at least be improved.

The simple inverse transformation mentioned above cannot perfectly reconstruct the true FDF due to the presence of the side lobe in the RMSF. An effective method to reduce the side lobe, called *RM* CLEAN, was proposed by Heald, Braun, and Edmonds (2009). *RM* CLEAN was shown to work, if multiple polarized sources are separated by more than the FWHM of RMSF from each other in Faraday depth space (Kumazaki et al. 2014; Sun et al. 2015a; Miyashita et al. 2016).

Another technique to estimate the true FDF is QU-fitting. We compare a model of polarized intensity with an observed one, where we can avoid performing incomplete inverse transformation. We explore the best-fitting model parameters using, for example, the Markov Chain Monte Carlo method. This exploration can be extended to various models, and we can argue the best model among them using, for example, Akaike's Information Criterion (AIC) or Bayesian Information Criterion (BIC):

$$\mathrm{AIC} = -2\log L + 2k, \tag{44}$$

$$\mathrm{BIC} = -2\log L + k\log n, \tag{45}$$

where L is the biggest likelihood, k is the number of parameters, and n is the number of data. These criteria evaluate not only the adaptability of a model to the data but also the simplicity of the model. The above QU-fitting approach showed better results than *RM* CLEAN in a recent benchmark challenge (see Sun et al. 2015a for details).

Faraday tomography is a powerful tool for studying the Faraday structure along a LOS, and is superseding classical *RM* study. Indeed, multiple polarized sources and their Faraday depths have been successfully resolved, even though they were not spatially resolved in radio/polarization images (O'Sullivan et al. 2012; Ozawa et al. 2015). The FDF intrinsically contain rich information about distributions of magnetic fields, thermal electrons, and CR electrons along the LOS, in the sense that the FDF indicates the synchrotron polarization as a function of Faraday depth. Thus, if we can understand how to extract such information from the FDF, the Faraday tomography technique maximizes its potential.

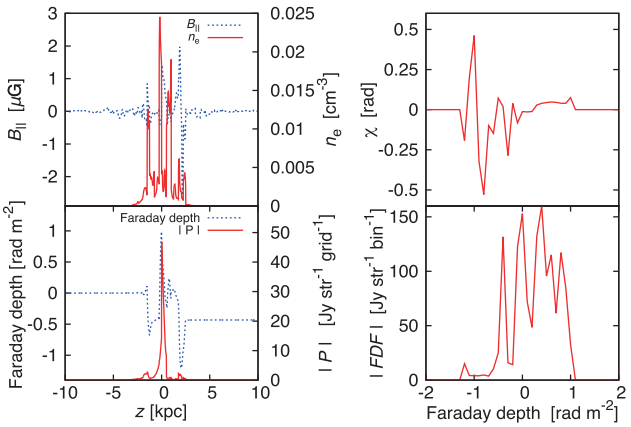

Fig. 4. Faraday spectrum of a simulated face-on spiral galaxy (Ideguchi et al. 2014b). (Top left) Distributions of the LOS component of magnetic fields and the thermal electrons, (bottom left) distributions of the polarized intensity and Faraday depth, (top right) the polarization angle, (bottom right) the absolute Faraday spectrum. (Color online)

The interpretation of the FDF is, however, not straightforward, mainly because there is no one-to-one correspondence between the Faraday depth and the physical distance. Hence the structure in physical space is not directly obtained from the FDF. Particularly, the presence of turbulent magnetic fields makes the interpretation difficult. There are some attempts to consider the effects of turbulence on the FDF of galaxies using simple models (e.g., Bell et al. 2011; Frick et al. 2011; Beck et al. 2012). It is found that the effect of turbulence appears as many small components in FDF, called the "Faraday forest."

Ideguchi et al. (2014b) studied the realistic form of the galactic FDF using the Galactic model produced by Akahori et al. (2013). They found very complicated FDFs and Faraday forests, which cannot be approximated by Gaussian or other simple analytic functions (figure 4). The complexity is mainly due to the stochasticity of turbulence in magnetic fields and gas density. Ideguchi et al. (2017) studied the FDF of face-on galaxies using a simpler model than former works. The turbulent magnetic field was expressed as a random field with single coherence length. They showed that the stochasticity can be significantly reduced if we consider a beam size about 10 times larger than the coherence length squared, and that the global properties of galaxies such as coherent magnetic fields and characteristic scales of turbulence could be extracted from the Faraday spectrum. These studies are also important for model functions of the QU-fitting and base functions of the compressed sensing.

4 Interstellar medium

Magnetic fields play an important role in the kinematics and energetics of the ISM. While magnetic fields assist the contraction of molecular clouds through transporting the angular momentum outward, they prevent the contraction against the self-gravity. Magnetic fields affect the evolution of H II regions and are essential for radio emission from supernova remnants (SNRs) and pulsar wind nebulae (PWN), both known as sources of Galactic CRs. It is considered that magnetic fields relate directly to filamentary and loop structures in the ISM. In this section, we review magnetic fields in various discrete objects in the ISM.

4.1 Thermal/pressure equilibrium

The ISM is composed of gases, dusts, CRs, magnetic fields, and radiation fields. The steady-state gaseous ISM is in pressure equilibrium among various species with multiple temperatures, e.g., warm and cold neutral materials (Field et al. 1969). Ionized gas is in pressure equilibrium with the UV radiation field from OB stars, while low-temperature gas containing dust is balanced in pressure with the starlight radiation field. The kinetic energy of the turbulent ISM is converted to magnetic energy through the dynamo action, reaching a pressure equilibrium between the gas and the magnetic field. The magnetic pressure is further in equilibrium with the pressure of interstellar CRs, which are accelerated and supplied by shock-compressed SNR shells and pulsar magnetospheres.

The condition for the stationary ISM is, therefore, ascribed to the equilibrium among the energy densities (which are equivalent to the pressures) of gases in various phases, magnetic fields, CRs, and the starlight UV radiation field:

$$u_{\rm mag} \sim u_{\rm CR} \sim u_{\rm gas} \sim u_{\rm H\,II} \sim u_{\rm H\,I} \sim u_{\rm MC} \sim u_{\rm UV}, \tag{46}$$

where $u_{\rm mag}$, $u_{\rm CR}$, $u_{\rm gas}$, $u_{\rm H\,II}$, $u_{\rm H\,I}$, $u_{\rm MC}$, and $u_{\rm UV}$ are the energy densities of the magnetic field, CR, gas (either in ionized gas, H I, or molecular gas clouds), and UV radiation. In typical interstellar conditions, except for giant molecular clouds and dense molecular cores, the gravitational energy is neglected as a reasonable approximation.

If one of the equilibrium conditions is broken, the ISM becomes unstable, resulting in local expansion, contraction, and/or ejection. The region containing such unstable ISM is regarded as an active region. Generally, astrophysical activity is defined as the state that the local condition is significantly displaced from the thermal/dynamical equilibrium, as often recognized in expanding H II regions, SNRs, jets and/or various types of instabilities, including the Parker magnetic inflation.

4.2 Local magnetic field

The local interstellar magnetic field is simply estimated from the synchrotron radio emissivity toward the Galactic poles, assuming that the magnetic and CR energy densities corresponding to the observed frequency are in equilibrium. Taking an LOS depth of ∼200 pc in the poles, where the brightness temperature after subtracting the 2.7 K due to the CMB is measured to be ∼10 K at 1 GHz, the field strength is estimated to be ∼3 μG. This leads to $u_{\rm mag} \sim 10^{-12}$ erg ~ 1 eV cm^{-3} (Sofue 2017).

A slightly stronger magnetic field, several μG, has been found in the local ISM at ∼100–200 pc from the Sun along the HI arch in the Aquila Rift, where a correlation analysis between the HI column density and Faraday *RM* of extragalactic radio sources were obtained to yield the LOS magnetic strength through HI filaments (Sofue & Nakanishi 2017).

More direct measurements of the local magnetic field have been obtained by linear polarization observations of 0.4 to 1.4 GHz all-sky continuum surveys (Reich 2007 for a review). They obtained the local magnetic field of a few μG from an analysis of the polarization intensities, degrees, and depolarization, as well as the Faraday screen effects at different frequencies.

The current estimations of the local magnetic field yielded a strength of a few μG, corresponding to an energy density of ∼1 eV cm^{-3}. These values are comparable to the energy densities of the ISM of $u_{\rm gas} \sim 1$ eV cm^{-3} with $n_{\rm gas} \sim 1$ cm^{-3} and turbulent velocity ∼5 km s^{-1} observed in the solar vicinity, indicating that the local magnetic field and gas are in pressure equilibrium.

4.3 Molecular clouds

Stars are formed in molecular clouds in which large-scale magnetic fields are observed. The direction of the magnetic fields in the clouds has been studied with linear polarization of thermal millimeter/sub-millimeter dust emission and extinction of light from background stars. The polarized thermal emission probes the high-density region of the molecular cloud (e.g., Rao et al. 1998; Girart et al. 2006), and the optical polarized light from background stars is sensitive to the magnetic fields in the ISM (e.g., Goodman et al. 1990; Chapman et al. 2011). Recent observations show the strong correlation between the directions of magnetic fields of the interstellar gas and those for the cores in the molecular clouds (Li et al. 2009). Since the weak magnetic fields are easily distorted by turbulence in the clouds, this result strongly suggests that the magnetic energies are larger enough than the random kinetic energies in molecular clouds.

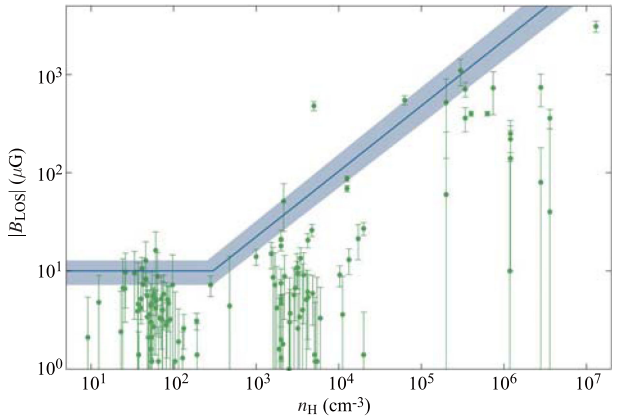

Fig. 5. Correlation between the hydrogen density and the LOS magnetic field strength (by the Zeeman effect) in molecular clouds (taken from Crutcher 2012). (Color online)

The magnetic field strength in molecular clouds is often estimated with the Chandrasekhar–Fermi method (Chandrasekhar & Fermi 1953) assuming that the velocity fluctuation of the clouds is related to the Alfvén waves that were assumed by the fluctuation of the magnetic field lines observed from polarized light. This method estimates the strength of the magnetic fields along the plane of sky. The method tends to overestimate the field strength; some molecular clouds show that their magnetic energies are larger than the gravitational energies (Alves et al. 2008; Chapman et al. 2011; Franco & Alves 2015).

The Zeeman effect is used to measure the strength of magnetic fields along the LOS (Crutcher 2012; figure 5). According to the observations of the OH and CN Zeeman effect, the magnetic energies in the molecular clouds or cores are estimated to be slightly smaller than the gravitational energies of the clouds or cores on average (e.g., Crutcher 1999; Troland & Crutcher 2008).

The magnetic field strength in molecular clouds is also estimated from the difference of line widths of neutral and ionized molecular lines (Li & Houde 2008), assuming that the ions have a steeper turbulent energy spectrum than that of the neutrals on the ambipolar diffusion scale. The line-width method can measure the strength of the magnetic field component on the plane of the sky. The magnetic field strengths obtained by the line width are consistent with those estimated from the Zeeman effect (e.g., Hezareh et al. 2010).

4.4 Star formation and magnetic field

In molecular clouds, the energy equipartition among turbulence, magnetic field, and self-gravity is roughly satisfied. Once the self-gravity dominates over the others, stars are formed. If the magnetic force is strong enough

to prevent the gravitational collapse in the clouds, stars are not formed. In this case, one of the important physical processes is the ambipolar diffusion (e.g., Nakano & Nakamura 1978; Basu & Mouschovias 1994; Mouschovias & Ciolek 1999). Since the magnetic field is frozen only to the ionized gas, neutral gas can pass through the magnetic field and contract by gravity. When the contraction makes gravity strong enough to collapse, stars begin to be formed (e.g., Basu & Ciolek 2004; Kudoh et al. 2007).

Since the ambipolar-diffusion time is normally larger than the free-fall time, stars are formed slowly in the molecular cloud if magnetic force is dominated, even though the ambipolar diffusion is enhanced by small-scale turbulent or large-scale flows in the molecular clouds (e.g., Fatuzzo & Adams 2002; Li & Nakamura 2004; Kudoh & Basu 2011). The suppression of the star formation by the magnetic field may explain the low star-formation rates and efficiencies in the clouds, although there are no direct evidence that the magnetic force dominates the gravity in the molecular clouds.

Once the collapse happens for the star formation, the magnetic field plays an important role in removing the angular momentum of the contracting gas (e.g., Mestel & Spitzer 1956; Mouschovias & Paleologou 1980; Nakano 1989) and forming outflows (e.g., Uchida & Shibata 1985; Pudritz & Norman 1986; Kudoh et al. 1998; Tomisaka 2002; Machida et al. 2008). The outflows from young stars can be the origin of turbulence in molecular clouds (Nakamura & Li 2007).

4.5 H II region

Heiles and Chu (1980) first estimated the magnetic field strength in H II regions from the Very Large Array (VLA) measurement of the Faraday rotation of extragalactic radio sources. The typical value of magnetic field strength in H II regions is between several μG to 12 μG (e.g., Sun et al. 2007; Gao et al. 2010). Heiles, Chu, and Troland (1981) measured magnetic field strengths in the H II regions S117, S119, and S264 as ranging from 1 μG to 50 μG.

Gray et al. (1999) achieved polarimetric imaging around the W3/W4/W5/HB3 in the Perseus Arm in order to study the ISM in the Milky Way. The images were obtained at 1420 MHz with an angular resolution of 1′ over more than 40 deg^2 with the Dominion Radio Astronomy Observatory Synthesis Telescope. They identified (i) mottled polarization arising from random fluctuations in a magneto-ionic screen in the vicinity of the H II regions themselves, and (ii) depolarization arising from very high *RM*s and *RM* gradients.

Harvey-Smith, Madsen, and Gaensler (2011) studied the LOS magnetic field in five large-diameter Galactic H II regions. Using the Faraday rotation with background polarized radio sources, they estimated the field strengths in the regions from 2 μG to 6 μG, which is similar to the values in the diffuse ISM. Using the same method, Rodriguez, Gomez, and Tafoya (2012) estimated the LOS-averaged magnetic field of 36 μG in an H II region, NGC 6334A, in the Milky Way. This value is consistent with the former trial estimation of this source, 40 μG (Kahn & Breitschwedt 1989).

Interaction processes between H II regions and adjacent molecular clouds in strong magnetic fields have been studied by many researchers (e.g., Yusef-Zadeh 1986). Using the IRAM 30 m telescope, Serabyn and Gusten (1991) observed the interacting region between H II region G0.18−0.04 and an associated molecular cloud. They showed that the magnetic field seems to work as a braking force on the cloud in the interaction. Krumholz, Stone, and Gardiner (2007) developed a three-dimensional MHD code for simulating the expansion of an H II region into a magnetized gas. They showed that the magnetic fields distort the H II region and reduce the strength of the shock. Gendelev and Krumholz (2012) extended the simulation to a blister-type H II region driven by stars on the edge of magnetized gas clouds. They found that magnetized blister H II regions can inject the energy into clouds. Pellegrini et al. (2007) found that the magnetic field in M 17 is strong enough to halt the expansion of the H II region. However, observational results of the magnetic fields in blister H II regions are still very limited.

4.6 Supernova remnant

The ejecta of a supernova interact with a high-density circumstellar medium and create shocks observed as a SNR. The shock waves can convert an SNR's kinetic energy of $\sim 10^{51}$ erg into not only the thermal energy of ionized plasma around the SNR but also various non-thermal energies and radiation. SNR shocks are thought to be the most plausible site of Galactic CR acceleration (Blasi 2013), and also excite Galactic turbulence. Magnetic fields play crucial roles in all these phenomena.

SNRs are found in the Milky Way and Local Group galaxies with angular sizes from minutes to degrees and ages from 10^2 to 10^5 yr. Green (2009) listed 294 SNRs in the Milky Way, based on bright and large characteristic shell-like structures in radio survey images.[1] The radio spectral index α (subsection 3.2) is in the range of $\alpha \sim 0.3$–0.8 in the Green catalog. The mean is close to $\alpha \sim 0.5$ or the CR electron energy spectral index $p = 2\alpha + 1 \sim 2$, which can be broadly explained as a test particle, strong shock case of the diffusive shock acceleration (DSA), $p = (r + 2)/(r - 1) \sim 2$,

[1] ⟨http://www.mrao.cam.ac.uk/surveys/snrs⟩.

where r is the shock compression ratio (see, e.g., Blandford & Eichler 1987 for a review). There is also evidence of electron acceleration based on the detection of synchrotron X-rays from shells of young SNRs (Koyama et al. 1995; Bamba et al. 2003).

In general, $O(100)\,\mu$G magnetic fields have been measured from radio total and polarized intensities. In some bright SNRs, $\sim$mG has been observed, indicating amplified magnetic fields (see, e.g., Reynolds et al. 2012; Gelfand et al. 2015; Haverkorn et al. 2015). Observations of non-thermal X-ray emissions in young SNRs provide evidence of magnetic field amplification in the shock regions (e.g., Bell 2004; Uchiyama et al. 2007; Inoue et al. 2012; Ressler et al. 2014). Radio observation can also provide information of shock microphysics. Barniol Duran, Whitehead, and Giannios (2016) recently found that the product of the energy fractions of non-thermal electrons (ε_e) and magnetic fields (ε_B) is around $\varepsilon_e\varepsilon_B \sim 0.001$ of the total shocked fluid energy for radio SNRs in the Magellanic Clouds.

The structure of magnetic fields in SNRs have been studied in the literature (e.g., Reynolds et al. 2012; Gelfand et al. 2015; Haverkorn et al. 2015). Reynolds et al. (2012) suggested that radial and tangential magnetic fields are generally predominant in young and old SNRs, respectively. Moreover, toroidal magnetic fields exist in some SNRs and they are interpreted as the fields associated with the shock-swept, past stellar wind of the progenitor (Uyaniker et al. 2002). It is, on the other hand, not clear how global Galactic magnetic fields and circumstellar magnetic fields affect the magnetic fields of SNRs (e.g., Purcell et al. 2015; Sun et al. 2015b; West et al. 2016) and how turbulence alters their properties (Bandiera & Petruk 2016). These questions will be addressed with more spatially-resolved samples. Moreover, understanding foreground/background structures are essential to resolve the structure of the targets. Broad-band polarimetry will be a key strategy for distinguishing them.

Finally, supernovae themselves are also interesting targets for radio observation. The lack of radio emission from Type Ia supernovae has been argued; no-radio detection in a near ($\sim$6.4 Mpc) extragalactic Type Ia SN 2011fe ruled out a symbiotic progenitor system and a system with a high accretion rate on to a white dwarf (Chomiuk et al. 2012). Another important topic is dust obscuration; Horiuchi et al. (2011) found that the measured core-collapse supernova (CCSN) rate is a factor of 2 smaller than that predicted from the massive-star formation rate. While optical observations suffer from dust obscuration, radio observations may have an advantage in finding a missing CCSN hidden in the inner region of the host galaxy and solve the problem.

4.7 Pulsar wind nebulae

A pulsar generates a relativistic, magnetized outflow called a pulsar wind. It appears as a transition from a cold, magnetic-energy-dominated flow into a hot, particle-energy-dominated flow around a strong termination shock. Relativistic particles in the downstream of the shock emit non-thermal radiations, which are identified as PWN (see, e.g., Reynolds et al. 2012; Gelfand et al. 2015). Magnetic reconnection is thought to play a key role in accelerating particles in PWN. There are models of magnetic reconnection before/at/after the termination shock.

Radio PWN are often seen around young (10^4–10^5 yr) pulsars. Pulsars can be kicked by a supernova explosion and hence often have high velocities of up to and beyond 1000 km s^{-1}, but some young pulsars can be still inside the SNR created by the progenitor explosion. In very young ($<10^4$ yr) SNR, there are two streams inside PWN. The first zone is between the pulsar and the wind termination shock, where the wind energy is radiation-dominated. The second zone is beyond the termination shock up to the outer bow shock, where the wind energy is particle-dominated. Radio synchrotron emission is bright at the second zone in general. PWN have radio spectral indices in the range $\alpha \sim 0.0$–0.3, which is shallower than those of SNRs and is too flat to be explained by simple models of diffusive shock acceleration (e.g., Tanaka & Takahara 2010).

Observations of inverse Compton emission in gamma-rays suggest a wide range of nebular magnetic fields, from $\sim 5\,\mu$G to >1 mG (de Jager & Djannati-Ataï 2009; Reynolds et al. 2012). Orientation of magnetic fields in PWN can be studied with polarization; some PWN show a broadly toroidal magnetic field (Kothes et al. 2006) and some others show complex or tangled appearance (Wilson & Weiler 1976). Kothes et al. (2006) suggested that these variations result from differences in viewing angle with respect to the pulsar's spin axis.

The number of detected PWNs is small compared to SNRs. This lack of samples remains an outstanding problem. The PWN magnetic field configuration will be best studied through depolarization and Faraday tomography with wideband data, and by dense RMs of background sources.

A binary pulsar provides an opportunity to observe an inter-binary plasma very close to the neutron star magnetosphere. For instance, Bogdanov et al. (2011) observed a strongly-magnetized wind compared to that seen further from the neutron star, and constrained possible models for magnetic reconnection in the pulsar wind. A binary pulsar also gives us an opportunity to observe eclipses and such eclipses have been observed in $\sim$50 binary pulsars (see Gelfand et al. 2015, references therein). We can measure

changes in the dispersion observed during the eclipse of a binary pulsar (Gelfand et al. 2015), which makes it possible to study the density and magnetic field structure of the intervening plasma.

4.8 Loop structure

Galactic H I survey data exhibit a lot of filamentary structures, some of which were called "worms" crawling out of the galactic plane (Heiles 1984). Some of them, vertically extending from the galactic plane, are interpreted as a part of expanding shells. Recent works show that such filamentary structures can be produced in the shock-compressed diffuse ISM and the orientation of H I filaments is controlled by the directions of shock propagation and magnetic field (Inoue & Inutsuka 2016). Meanwhile, some part of filamentary structures are thought to be magnetically floating loops generated by the Parker instability, which is thought to work in the galactic dynamo (Parker 1971). Candidates of such magnetic floating loops have been found in nearby galaxies such as M 31 (Beck et al. 1989), NGC 253 (Sofue et al. 1994), and IC 342 (Beck 2015).

Fukui et al. (2006) identified two Galactic molecular loops, named Loops 1 and 2, from wide-field imaging observations of the ^{12}CO ($J = 1$–0) line with the NANTEN 4 m telescope in Chile. The molecular loops are located within 1 kpc of the galactic center and their length and width were measured as several hundred pc and 30 pc, respectively. The total mass and kinetic energy of the molecular loops were estimated to be $1.7 \times 10^5\,M_\odot$ and 0.9×10^{51} erg, respectively. This energy is comparable to the energy supplied by a single supernova explosion, though it may not be able to convert all the energy to the loop. Therefore, they concluded that the magnetic floatation is a more plausible mechanism to explain the physical characteristics of the molecular loop. Fujishita et al. (2009) extended this study and found another more massive molecular loop, called Loop 3, which had estimated total mass and kinetic energy of $3.0 \times 10^6\,M_\odot$ and 1.7×10^{52} erg, respectively. This observational evidence supports that molecular loops are formed by magnetic fields.

Kamaya et al. (1996) demonstrated that Parker instability can be easily triggered by a single supernova explosion forming an Ω-shaped structure based on two-dimensional MHD simulations. Takahashi et al. (2009) conducted two-dimensional MHD simulations and found that loop-like structures can be formed through the Parker instability. They showed that the molecular loops emerging from the low-temperature layer are similar to the dark filaments observed in the solar surface. Moreover, Machida et al. (2009) conducted three-dimensional MHD simulations of the gas disk in the galactic center and found that buoyantly rising magnetic loops are formed at a typical height of 200 pc from the galactic plane. The typical length and width were 0.1–2 kpc and 50–300 pc, respectively, which are consistent with physical parameters of the molecular loop found in the galactic center.

Loop 3 is considered to be a loop in an earlier evolutionary phase than Loops 1 and 2. Torii et al. (2010) carried out sensitive CO observations for the footpoints of Loops 1 and 2, where gas is expected to be accumulated by the falling motion along the loops, and found a sharp intensity gradient characterized by a U shape, which suggests the existence of a shock caused by the falling gas. The gas density and temperature are found to be higher at these footpoints because of the shock heating. The $b - v$ diagram shows footpoints found as a U shape, an L shape or a mirrored-L shape, which can be explained by a simple kinematic model incorporating the expansion of the loop and the galactic rotation (Kudo et al. 2011).

The Aquila Rift is also thought to be another magnetically floating loop. Sofue and Nakanishi (2017) studied the RM of radio sources behind the arch of the Aquila Rift to show that the magnetic field with a strength of 10 μG is aligned along the Aquila Rift arch, and they suggested that it is formed by the Parker instability. Sofue and Nakanishi (2017) studied the *RM* of radio sources behind the arch of the Aquila Rift to show that the magnetic field with a strength of 10 μG is aligned along the Aquila Rift arch, and they suggested that it is formed by the Parker instability.

5 The Milky Way

The GMF (galactic magnetic field) in the Milky Way is introduced in this section. We first briefly summarize properties of the diffuse ionized medium (DIG), because the GMF is tightly related to the DIG. We then review the GMFs towards the galactic plane, towards the halo or high galactic latitudes, and towards the galactic center, in this order. Regular magnetic fields and random magnetic fields are introduced separately, since their origins and properties are different. Hereafter, for convenience, we define the galactic plane (the galactocentric cylindrical coordinate $|z| \lesssim 1$–2 kpc), the galactic halo ($|z| > 1$–2 kpc), high galactic latitudes (the galactic latitude $|b| > 50^\circ$), and the galactic center ($|r| < 1$ kpc).

5.1 Properties of diffuse ionized gas

Observations of pulsars allow us to estimate the DIG's electron density through pulsar dispersion measures (DMs). Cordes and Lazio (2002, 2003) developed the NE2001 model, which is currently the standard model of three-dimensional distribution of the electron density in the Milky

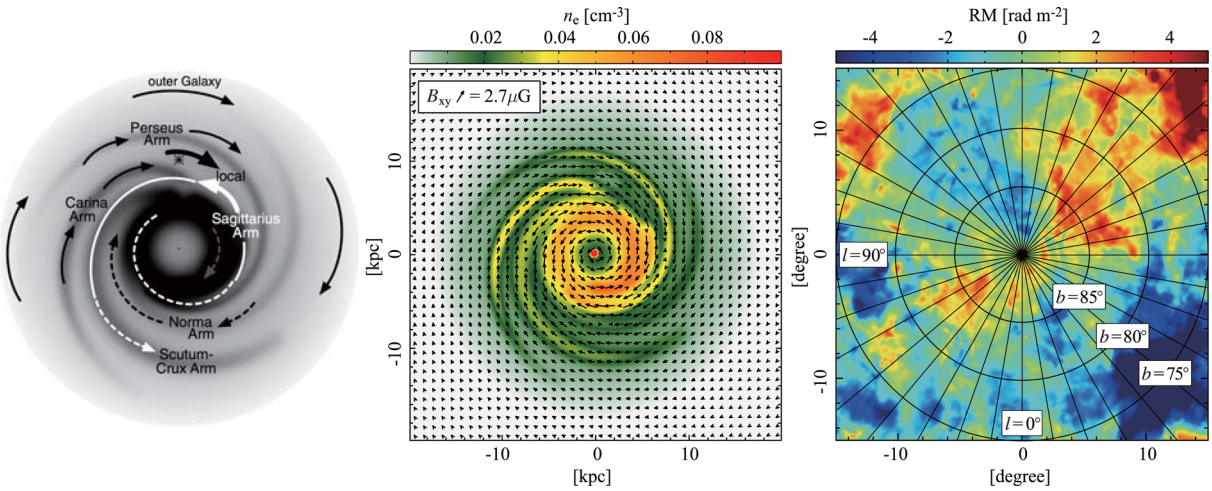

Fig. 6. (Left) Sketch of the magnetic field in the disk of the Milky Way based on *RM* observations (Van Eck et al. 2011). (Middle) The color shows the modified NE2001 thermal electron density, and arrows depict the ASS+RING disk magnetic fields (Sun et al. 2008). (Right) *RM* toward high galactic latitudes based on a model of regular and turbulent components (electron density and magnetic fields) of the Milky Way (Akahori et al. 2013). (Color online)

Way (see also Schnitzeler 2012 for recent work). Gaensler et al. (2008) proposed a modification of the parameters for the so-called thick disk component, the scale height (modified from 0.97 kpc to 1.8 kpc) and the mid-plane electron density (modified from 0.034 cm^{-3} to 0.014 cm^{-3}), which better reproduce both *DM* and emission measure (EM) toward high galactic latitudes. Figure 6 shows the modified NE2001 model.

Due to the presence of turbulence, local electron density fluctuation also exists. The electron volume filling factor, ∼0.05–0.5, which quantifies the clumpiness, has been estimated from *DM*s and emissions/absorptions (e.g., Peterson & Webber 2002; Berkhuijsen et al. 2006; Hill et al. 2008; Gaensler et al. 2008; Sun et al. 2008).

The plasma β_0, the ratio of the gas pressure to the magnetic pressure due to the regular magnetic field, is one of the key parameters which characterize magnetic turbulence. The gas pressure can be derived from observations of electron temperature, T_e. According to Hα observations, the distribution of T_e can be approximated by $T_e(R, z) = 5780 + 287R - 526|z| + 1770z^2$, where T_e is in units of K and the galactocentric cylindrical coordinates R and z are in kpc (Sun et al. 2008). With observations of magnetic field strength, the plasma β_0 is expected in the range of ∼0.01–100 and becomes smaller away from the galactic plane (Akahori et al. 2013).

The rms Mach number $M_{rms} \equiv u_{rms}/c_s$, the ratio of the rms speed of random flow motions u_{rms} to the sound speed c_s, is another key parameter which characterizes magnetic turbulence. A weak constraint on the plausible range of M_{rms} is only provided by previous Hα observations toward high galactic latitudes. Hill et al. (2008) studied the distribution of EM, and found that $M_{rms} \sim 1.4$–2.4 for $|b| > 10^\circ$ and M_{rms} is smaller at higher galactic latitudes. Studies of polarization gradients also broadly constrain $M_{rms} \sim 0.5$–2 (Gaensler et al. 2011; Burkhart et al. 2012). There is so far no observational evidence which motivates the introduction of a large-scale gradient of u_{rms} toward high galactic latitudes. A simple approximation would be a uniform rms speed with $u_{rms} \sim 15$–$50\,\mathrm{km\,s^{-1}}$ (or $M_{rms} \sim 0.5$–2).

5.2 Magnetic fields in galactic plane

5.2.1 Regular magnetic field

The large-scale field in the galactic disk has been studied using *RM*s of pulsars and extragalactic radio sources (Beck 2001; Han & Wielebinski 2002; Haverkorn 2015 for review), and using total and polarized synchrotron intensities of the galactic synchrotron emission as well as *RM*s (Haverkorn et al. 2004; Jaffe et al. 2010; Jansson & Farrar 2012; Beck et al. 2016). Also, the GMF has been constrained through observation of near-infrared star light polarization (e.g., Nishiyama et al. 2010; Pavel 2011; Pavel et al. 2012).

The total magnetic field strength including regular and random components has been constrained from the synchrotron radio intensity by assuming equipartition between the energy density of CRs and that of magnetic fields. According to Beck (2001), the total magnetic field strength is estimated to be ∼6 μG. Jaffe et al. (2010) simulated total and polarized synchrotron intensities using a GMF model which consists of coherent, isotropic random, and anisotropic random ("ordered" or "striated") components.

They found that the peak strength of the coherent component is ∼1–3 μG, and found that the relative energy density ratio of these components is roughly 1 : 5 : 3.

The GMF orientation has been studied using *RM*s of pulsars and extragalactic radio sources. Studies of nearby pulsars show that the local field is directed toward the galactic longitude $l \sim 70^\circ$–90° and the field strength is ∼2–3 μG (e.g., Manchester 1974; Thomson & Nelson 1980). A large-scale GMF model in the galactic disk, where the R or BSS configuration is assumed, is determined so that the observed distribution of *RM*s is reproduced. The studies suggest at least one field reversal interior to the solar circle (e.g., Simard-Normandin & Kronberg 1980; Sofue & Fujimoto 1983; Rand & Kulkarni 1989). By using large data sets of *RM*s compiled by Taylor, Stil, and Sunstrum (2009) (37543 sources, figure 9) and Kronberg and Newton-McGee (2011) (2257 sources), it has been possible to develop the GMF model which consists of a disk field and a halo field. Pshirkov et al. (2011) found that the spiral-field models fit the observed *RM* distribution better than the ring-field model, and also found that the disk field is symmetric with respect to the galactic plane and in contrast the halo field is antisymmetric.

Pulsar *DM*s and *RM*s allow us to evaluate the GMF orientation at different positions in the galactic disk, because the distance to a pulsar is estimated from *DM* (e.g., Vallée 2005, 2008). Han et al. (2006) estimated the mean LOS component of the GMF within regions near the tangential points of the spiral arms and the inter-arms, using the mean slope of the *DM*–*RM* plot, $\langle B_\parallel \rangle = 1.232 \langle \Delta RM / \Delta DM \rangle$, for 554 *RM*s of pulsars, where ΔRM and ΔDM are differences in *RM*s and *DM*s, respectively. The obtained distribution of $\langle B_\parallel \rangle$ suggests that the large-scale magnetic fields in the spiral arms are counterclockwise, but in the inter-arm regions the fields are clockwise. As a result, they suggest that the large-scale GMF has a BSS configuration. The GMF structure derived from *RM*s of pulsars which include new data and that of extragalactic sources is presented in Han et al. (2015).

Several attempts have been made to determine the large-scale field in the arm and inter-arm regions (e.g., Brown et al. 2007; Nota & Katgert 2010; Van Eck et al. 2011). Van Eck et al. (2011) developed an empirical model of the GMF in the disk using a multi-sector model. In this model, the galactic disk is divided into three sectors: A ($100^\circ < l < 260^\circ$), B ($260^\circ < l < 360^\circ$), and C ($0^\circ < l < 100^\circ$). They considered some models in each sector. The best-fitting parameters of each model are determined independently so as to reproduce the observed *RM*s of both pulsars and extragalactic sources. They do not use any boundary matching condition between the sectors to see whether there are any common features among the sectors. In the galactic outer region (sector A), the ring field model without field reversals reproduces the *RM* variation along the galactic longitude better than the spiral model. In sectors B and C, the large-scale field in the inner disk follows the spiral arms, i.e., the spiral magnetic field with a pitch angle of $11^\circ.5$ except for the innermost and the outermost regions, in which azimuthal field is assumed. They conclude that the large-scale GMF is predominantly clockwise while a single reversed region exists in the inner Galaxy (left-hand panel of figure 6).

One field reversal interior to the solar circle is a common feature between observational studies on the GMF. However, the existence of more field reversals is still controversial. One of the difficulties in determining the GMF orientation is an effect of SNRs and H II regions. Since these sources significantly affect *RM*s and *DM*s (Clegg et al. 1992; Mitra et al. 2003; Nota & Katgert 2010), their influence has to be reduced as much as possible. The theoretical explanation of field reversals is also under debate, as described in section 6. Furthermore, it seems difficult to represent the large-scale GMF by the beautiful spirals or rings that have been used. Men, Ferrière, and Han (2008) and Noutsos et al. (2008) examined whether the widely used models of the large-scale magnetic field (R, ASS, and BSS) are consistent with the observed data or not, but could not successfully reproduce the observations. These results suggest that the GMF has a more complex configuration and/or more complex random field components.

5.2.2 Turbulent magnetic field

The random field strength has been estimated from residual *RM*s (e.g., Jokipii & Lerche 1969; Thomson & Nelson 1980; Rand & Kulkarni 1989; Brown & Taylor 2001). A best-fitting model of the large-scale magnetic field is determined so that the variance of residuals $\langle (RM_{\rm obs} - RM_{\rm model})^2 \rangle$ is minimized, where $RM_{\rm obs}$ is *RM* from observation and $RM_{\rm model}$ is that derived from an assumed field model, and the brackets denote the averaging over all observed sources. If the residual is assumed to be caused by the random field component, the residual is expressed in terms of random walks (a single-size cell model) as $|RM_{\rm obs} - RM_{\rm model}| \propto (n_{\rm e} \delta B L) \sqrt{d/L}$, where $n_{\rm e}$ is the electron density, δB is the random filed strength, L is the cell size which corresponds to the outer scale of turbulence (the energy forcing scale), and d is the distance to a radio source. Rand and Kulkarni (1989) used *RM*s of 163 pulsars. They excluded pulsars with $|B_\parallel| > 2\,\mu$G in the region $0^\circ < l < 60^\circ$ affected by the North Polar Spur. They found that a concentric-ring model of the GMF reproduced the observed *RM* distribution better than a BSS model. As a result, they obtained the random field strength $\delta B \sim 5\,\mu$G

and the cell size $L \sim 55$ pc from the variance and the covariance of best-fitting residuals with the single-cell-size model.

As noted above, the residuals of *RM*s increase with pulsar distance; $|RM_{\rm obs} - RM_{\rm model}| \propto \sqrt{d}$. However, the obtained residuals do not show the expected correlation (Rand & Kulkarni 1989; Mitra et al. 2003). Since this lack of correlation suggests that the large-scale field is not represented by the beautiful spirals or rings, Ohno and Shibata (1993) evaluated the random field without using any large-scale field models. They used pairs of pulsars which are seen in almost the same directions on the sky. The electron density weighted magnetic field $B_\parallel$ in the region between the pair is obtained in terms of differences between their *RM*s (ΔRM) and *DM*s (ΔDM), $B_\parallel = \Delta RM/(0.81\Delta DM)\,\mu$G. The obtained correlation between $|B_\parallel|$ and ΔDM was interpreted by means of a Monte Carlo simulation with the single-cell-size model considering effects of random magnetic fields, electron density fluctuation, and finite angular separations of the pulsar pairs. They found the random field strength to be $\delta B \sim 4$–$6\,\mu$G with the cell size $L \sim 10$–100 pc.

Han, Ferriere, and Manchester (2004) also analyzed the random magnetic field using pulsar pairs. They sampled 1200 pulsar pairs from 490 pulsars and evaluated the power spectrum of the turbulent fields from the correlation between $|B_\parallel|$ and distance between paired pulsars. The obtained spectrum is $E_B(k) \propto k^{-0.37}$ over the scale range 0.5–15 kpc. This suggests that the power spectrum of the interstellar turbulent fields becomes flatter than the Kolmogorov spectrum at the scales larger than the outer scale ($\sim$10–100 pc).

Fluctuations of interstellar magnetic fields and electron density on scales smaller than $\sim$100 pc have been investigated through the second-order structure function (subsubsection 2.4.2) of *RM*s, $S_{2,RM}(\delta\theta)$ defined as $S_{2,RM}(\delta\theta) = \langle[RM(\theta) - RM(\theta+\delta\theta)]^2\rangle_\theta$, where θ is the position of a source in angular coordinates and $\delta\theta$ is the separation between sources. $S_{2,RM}$ is related to the power spectrum of random fields and density fluctuations (Simonetti et al. 1984; Minter & Spangler 1996); $S_{2,RM}(\delta\theta) \propto \delta\theta^{5/3}$ on scales smaller than the outer scale when the power spectrum of the ISM turbulence follows the Kolmogorov scaling (subsection 2.3).

Sun and Reich (2009) found that the slope of $S_{2,RM}$ varies depending both on the outer scale and the integral length of *RM*s. They found $S_{2,RM}(\delta\theta) \propto \delta\theta^{5/3}$ when the outer scale is comparable to the integral length. On the other hand, $S_{2,RM}$ has a shallower slope, $S_{2,RM}(\delta\theta) \propto \delta\theta^{2/3}$, when the integral length exceeds the outer scale, because the fluctuations are smeared out. We can estimate the outer scale from the scale at which $S_{2,RM}$ becomes flat. Haverkorn et al. (2008) evaluated $S_{2,RM}$ from *RM*s of extragalactic sources within an area of $253^\circ < l < 357^\circ$ and $|b| < 1.^\circ5$. They found that $S_{2,RM}$ in the Carina and Crux spiral arms have a flat slope, and estimated that the outer scale is smaller than $\sim$10 pc. This suggests that stellar sources are the main energy source of the turbulence in the spiral arms. Meanwhile, $S_{2,RM}$ in the inter-arm regions have a shallower slope than the Kolmogorov, suggesting an additional energy source on larger scales $\sim$100 pc.

Also, the spatial gradient of linearly polarized synchrotron emission is used to constrain the sonic Mach number of the ISM turbulence (Gaensler et al. 2011; Burkhart et al. 2012; see also synchrotron fluctuation by Lazarian & Pogosyan 2016, Herron et al. 2016, and Zhang et al. 2016). Iacobelli et al. (2014) found that the observational data from S-band Polarization All Sky-Survey is consistent with transonic turbulence through comparison with MHD simulations.

5.3 Magnetic fields toward high galactic latitudes

5.3.1 Regular magnetic field

Regular, coherent magnetic fields toward high galactic latitudes can be combinations of disk spiral (e.g., Prouza & Šmída 2003; Sun et al. 2008; Van Eck et al. 2011; middle panel of figure 6), halo toroidal (e.g., Takami & Sato 2010; Sun & Reich 2010; Pshirkov et al. 2011; Mao et al. 2012a), and halo poloidal (or X-) fields (e.g., Giacinti et al. 2010; Jansson & Farrar 2012). By definition, the spiral field dominates the regular magnetic field near the galactic plane, while the toroidal field dominates above it. Transition from disk to halo fields arises at $\sim$1.25 kpc from the mid-plane.

*RM*s toward the galactic poles have been investigated in the literature. Using *RM* data from the NRAO VLA Sky Survey (NVSS), Taylor, Stil, and Sunstrum (2009) estimated non-zero vertical strengths of the GMF, about $-0.14 \pm 0.02\,\mu$G and $+0.3 \pm 0.03\,\mu$G toward the North Galactic pole (NGP) and South Galactic pole (SGP), respectively. Mao et al. (2010) used *RM* data from the Westerbork Radio Synthesis Telescope (WSRT) and the Australia Telescope Compact Array (ATCA), and found that the median value of *RM*s toward the SGP is $+6.3 \pm 0.5$ rad m^{-2} (corresponding to V field strength of $+0.31 \pm 0.02\,\mu$G), while that toward the NGP is 0.0 ± 0.5 rad m^{-2} ($+0.00 \pm 0.02\,\mu$G). The origin of this field anomaly is not resolved (see Akahori et al. 2013, for some discussion therein).

5.3.2 Turbulent magnetic field

Highly disturbed distributions of *RM* and polarization angle clearly indicate turbulent structures of the GMF (Sun et al. 2008; Taylor et al. 2009; Waelkens et al. 2009; Gaensler et al. 2011). Using the WSRT and ATCA data, Mao et al. (2010) claimed standard deviations of *RM* of $\simeq 9.2$ rad m^{-2} and 8.8 rad m^{-2} toward the NGP and SGP, respectively. They put an upper limit of $\sim 1\,\mu$G on the

strength of random magnetic fields at high galactic latitudes. Based on the latitude dependence of *RM*, Schnitzeler (2010) examined the galactic and extragalactic contributions to *RM* in the NVSS data. He estimated that the galactic contribution (including both the disk and halo components) is $\bar{\sigma}_{RM,\mathrm{MW}} \sim 6.8 \pm 0.1 (8.4 \pm 0.1)\,\mathrm{rad\,m^{-2}}$ and the extragalactic contribution (including those intrinsic to the polarized background radio sources and due to the IGM) is $\bar{\sigma}_{RM,\mathrm{EG}} \sim 6.5 \pm 0.1 (5.9 \pm 0.2)\,\mathrm{rad\,m^{-2}}$ for the northern (southern) hemisphere. Stil, Taylor, and Sunstrum (2011) examined the NVSS data in detail, and found that $S_{2,RM}$ at $\delta\theta \gtrsim 1^\circ$ has a value ∼100–200 rad m^{-2} towards the NGP and ∼300–400 rad m^{-2} towards the SGP.

The random, turbulent component has been modeled analytically using power-law spectra with random phases in Fourier space, i.e., uniform turbulence. For instance, Sun and Reich (2009) used the publicly-available HAMMURABI code (Waelkens et al. 2009), and adopted a Kolmogorov-like power spectrum with average amplitude 3 μG in a box of 10 pc in size. They found that $S_{2,RM}$ has a magnitude of up to a few $\times$ 100 rad m^{-2} at angular scales of $>10'$ at galactic latitudes $|b| \sim 70^\circ$.

Constant rms amplitudes for electron density fluctuations and turbulent magnetic fields, however, would not be justified, because the amplitudes should depend on β_0 and M_{rms} and they distribute broadly toward high altitudes. In addition, in turbulent flows, phases are not really random. Towards high galactic latitudes, the random components are the dominant contribution to the *RM*. Akahori et al. (2013) developed a sophisticated model of the Milky Way (right-hand panel of figure 6). While they modeled the regular component based on a number of observations, they used the data of three-dimensional MHD turbulence simulations and first considered latitude dependencies of β_0 and M_{rms} to model the random component.

Akahori et al. (2013) found that the observed medians of *RM*s toward the north and south galactic poles are difficult to explain with any of the many alternative GMF models. The standard deviation of observed *RM*s is clearly larger than that of simulated *RM*s. $S_{2,RM}$ of the observed *RM*s is substantially larger than that of the simulated *RM*s, especially at small angular scales. They suggested that reproducing the observed medians may require additional components or/and structures of the GMF that are not present in their models. They also pointed out the *RM* due to the IGMF may account for a substantial fraction of the observed *RM*.

5.4 Magnetic fields toward the galactic center

5.4.1 Magnetic fields around the galactic center

Magnetic fields around the galactic center are observed to be as strong as up to 2 mG, an order of magnitude stronger than those in the local galactic disk (Mezger et al. 1996). This region has many strong radio continuum sources, Sgr A, B, C, D, and E, along the galactic plane in the order of their flux densities (Altenhoff et al. 1978; Mezger et al. 1996; Morris & Serabyn 1996).

Sgr A consists of the non-thermal Radio Arc, the Bridge of thermal filaments, Sgr A East, Sgr A West, and Sgr A* (e.g., Mezger et al. 1996). Yusef-Zadeh, Morris, and Chance (1984) carried out VLA observations of Sgr A at 6 cm and 20 cm. Their results indicate that the Radio Arc consists of a system of narrow filamentary structures of lengths larger than 30 pc but typical widths as narrow as 1 pc. The filaments consist of two groups: one is the "Radio Arc" emitting non-thermal polarized emission, which is a bunch of numerous vertical filaments perpendicular to the galactic plane and which crosses the plane. The other is "arched" filaments emitting thermal radiation, which arises in the halo of Sgr A, diverges curving eastward, and joins the vertical filaments of the Radio Arc.

Linear polarization with a polarization degree of ∼20% is seen along the vertical filaments in the Radio Arc, and the filaments indicate high $RM \sim 10^3\,\mathrm{rad\,m^{-2}}$ (Inoue et al. 1984; Tsuboi et al. 1986; Sofue et al. 1987). The observed *RM* sharply increases along the Arc toward the galactic plane, but suddenly drops to zero near the plane due to strong beam and bandwidth depolarization. The observed *RM* is then followed by a negative steep increase toward the opposite side of the plane. Such a reversal of the *RM* value across the galactic plane means that the vertical magnetic field is pinched at the disk due to twisting rotation with respect to the off plane field. On the other hand, the thermal arched filaments show no linear polarization (Yusef-Zadeh & Morris 1988).

Morris, Uchida, and Do (2006) obtained a near-infrared image near the galactic center using the Spitzer Space Telescope at 24 μm, and found an intertwined double helix nebula with a length of 25 pc. Each of the two continuous helically-wound strands rounds about 1.25 full turns. They interpreted that this feature is explained as a torsional Alfvén wave propagating vertically away from the galactic plane.

The Radio Arc is a part of a larger-scale off-plane radio lobe over the galactic center (Sofue & Handa 1984). The height of the galactic center Lobe is 1.°2 from the galactic plane or about 200 pc in size. The formation mechanism is still controversial, whether it is produced by a vertical field twisted by the rotation of an accreting gas disk, due to inflation of giant loop of magnetic tube filled with ionized gas, or is a result of some explosive events at the center. The western ridge of the lobe apparently emerges from Sgr C and has a filament and polarization indicating existence of magnetic fields (Yusef-Zadeh & Morris 1988; Sofue 1989).

Anantharamaiah et al. (1991) conducted 90 VLA observation for a $2^\circ \times 2^\circ$ field and found many non-thermal filaments, all of which are perpendicular to the galactic plane. These structures trace a vertical (V; poloidal), or a dipole magnetic field (Morris & Serabyn 1996). LaRosa et al. (2000) enlarged the 90-cm VLA observation area for $4^\circ \times 5^\circ$ and catalogued over a hundred sources (including SNRs, filaments, threads, the Snake, and the Mouse) that show structures of a variety of magnetic structure types and activity near the galactic center.

An MHD model of the magnetic field structure near the galactic center was proposed by Uchida et al. (1985) and extended by Shibata and Uchida (1987). Assuming that magnetic fields are frozen into the interstellar gas, a differentially rotating and infalling gaseous disk can shear an initially poloidal field into a toroidal, and produce a twisted/helical field.

Far-infrared and submillimeter polarization observations suggested that magnetic fields are parallel to the galactic plane, indicating toroidal magnetic fields (e.g., Morris et al. 1992). Nishiyama et al. (2009, 2010) conducted wide-field near-infrared polarimetry of point sources in J, H, and K_s bands, and found that the magnetic fields near the galactic plane are almost parallel, but the fields are nearly perpendicular to the galactic plane at high galactic latitudes. It suggests transition from a toroidal to a poloidal magnetic field.

5.4.2 At Sgr A* and the black hole

Earth's nearest candidate supermassive black hole, whose mass is estimated to be $\sim 4 \times 10^6\,M_\odot$, lies at the exact center of Sgr A* (Ghez et al. 2008; Gillessen et al. 2009). If strong magnetic fields exist around the black hole, they can influence the dynamics of accretion, and can transport angular momentum from the infalling gas to relativistic jets.

Plante, Lo, and Crutcher (1995) detected strong magnetic fields of -3.0 ± 0.5 mG at $1'$ north of Sgr A* by measuring the Zeeman splitting of the H I absorption line. Bower et al. (2005) conducted polarimetric observations between 215 GHz and 230 GHz using the BIMA (Berkeley–Illinois–Maryland Association) array and detected a variable linear polarization from Sgr A*, suggesting a hot turbulent accretion flow. Macquart et al. (2006) observed an RM of $-4.4 \pm 0.3 \times 10^5$ rad m^{-2} at 82 GHz and 86 GHz using the BIMA array and detected polarization variability on a timescale of days for Sgr A*. They argued that such high Faraday rotation occurs external to the polarized source at all wavelengths, and it may imply an accretion rate $\sim(0.2$–$4) \times 10^8\,M_\odot$ yr^{-1}. Marrone et al. (2007) detected an unambiguous Faraday rotation of -5×10^5 rad m^{-2} in Sgr A* at 227 GHz and 343 GHz using SMA.

Johnson et al. (2015) conducted very long baseline interferometry (VLBI) observations at 1.3 mm and spatially resolved the linearly polarized emission from Sgr A*. They found evidence of partially ordered magnetic fields near the event horizon. This kind of high-frequency VLBI approach is important because the surrounding black hole region should have dense electron density and so electron scattering is large. There will be another way of researching the galactic center using the supposed thousands of pulsars in the central region, some of which may transport Faraday rotation information in the vicinity of the black hole.

In fact, Swift discovered a new soft gamma-ray repeater, SGR J1745−2900, near Sgr A* (Kennea et al. 2013), and the source was identified as an X-ray as well as a radio pulsar, PSR J1745−2900, which has a pulsation period of 3.76 s (e.g., Mori et al. 2013; Eatough et al. 2013a). Eatough et al. (2013b) reported multi-frequency radio measurements of the newly discovered pulsar and showed the pulsar's unusually large RM of $(-6.696 \pm 0.005) \times 10^4$ rad m^{-2}, which indicates a dynamically relevant magnetic field near the black hole.

Recently, it was found by IR precision astrometry observations that a small gas cloud, G2, is approaching Sgr A* (Gillessen et al. 2009). It seemed that emission enhancement would occur if G2 caused some perturbation in the accretion flow around the supermassive black hole. However, no significant microwave enhancement of Sgr A* was observed (Tsuboi et al. 2015). There are some possible explanations of this result. In the case that G2 is a gas cloud, one possible explanation of the lack of significant microwave enhancement is that the magnetic fields in the accretion flow are too strong to make bow shock waves in the accretion flow. If the Alfvén velocity around Sgr A* is faster than the velocity of the G2 cloud, 6000 km s^{-1}, the result suggests the lower limit of the magnetic field, 30 mG (Tsuboi et al. 2015). Kawashima, Matsumoto, and Matsumoto (2017) carried out MHD simulations of an accretion disk for Sgr A* to study the effect of pericenter passage of the G2 cloud. They found that magnetic fields in the accretion disk are enhanced by the G2 perturbation 5–10 years after the pericenter passage of G2. Since the enhancement boosts synchrotron emission from the disk and the outflow, the radio and the infrared luminosity of Sgr A* is expected to increase around A.D. 2020.

6 Galaxies

Studying the GMF in external galaxies is important for understanding how the GMF were formed and evolved in the universe as well as understanding the correlation between the GMF and various properties of galaxies such as the morphology, degree of star formation, supernova

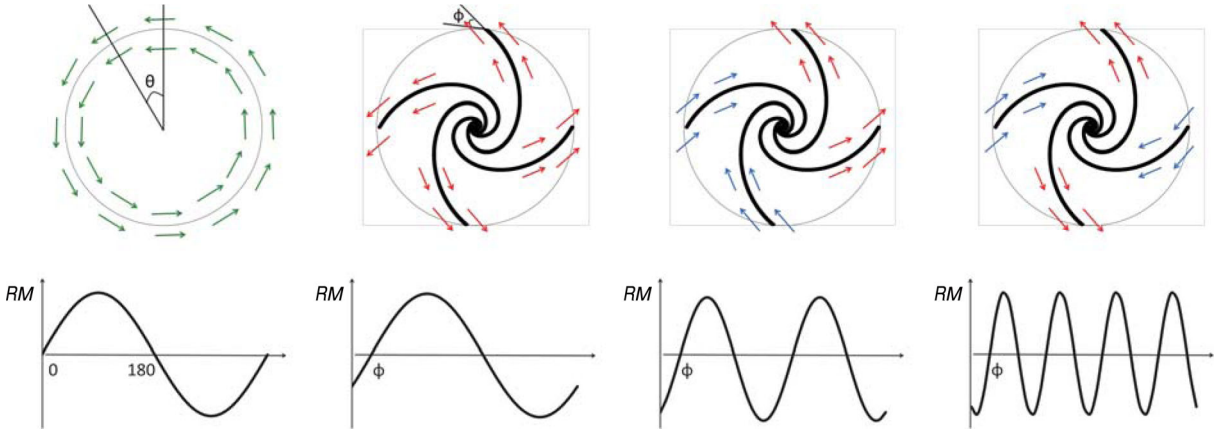

Fig. 7. From left to right, the panels show magnetic fields of Ring, ASS, BSS, and QSS. In the case of BSS and QSS, there are two and four reversals in the magnetic fields, respectively, but no reversal in the cases of Ring and ASS. (Color online)

and stellar wind feedbacks, AGN activity, and so on. In this section, we review the GMF in normal spiral galaxies and other galaxies in that order, and then summarize the cosmological evolution of the GMF. Similar to the Milky Way, the GMF in external galaxies can be described as a combination of large-scale regular fields and small-scale turbulent fields.

6.1 Normal spiral galaxies

Detection of synchrotron emission indicates the existence of magnetic fields as well as CR electrons in spiral galaxies. The magnetic field strength can be estimated by assuming the equipartition between the total energy densities of CRs and that of the magnetic field (see subsection 3.2). Applying such an equipartition assumption to the observational data for one of the well-studied nearby spiral galaxies, IC 342, the typical strength of the total magnetic field was estimated to be 15 μG assuming $K_0 = 100$, $i = 31^\circ$, $l = 1/\cos i$, and $\alpha = 1.0$ (Beck 2015). Basu, Roy, and Mitra (2012) argue that the condition of the equipartition is satisfied on a scale of >1 kpc while it does not hold on small scales (Stepanov et al. 2014).

The typical magnetic field strength is estimated to be 1–10 μJy by measuring the Faraday rotation. It is known that synchrotron and far-infrared luminosities for normal galaxies are well-correlated with each other (Condon et al. 1991) and that this correlation holds for high-redshift galaxies (Murphy 2009). Current possible scenarios of the origin of the radio–FIR correlation are (i) a calorimeter model (Voelk 1989) and (ii) an equipartition model (Niklas & Beck 1997). The former model suggests that a power of the radio emission is independent of the magnetic energy density in assuming that the lifetime of CR electrons is inversely proportional to the magnetic energy density.

6.1.1 Regular magnetic field

Polarization observation shows that magnetic fields are globally coherent along spiral arms with the same pitch angle (Fletcher et al. 2011). The global configuration of the coherent magnetic field is roughly classified into ASS and BSS fields. Typical examples of the ASS configuration are M 31 (Sofue & Takano 1981) and IC 342 (Graeve & Beck 1988). Typical cases for BSS are M 51 (Tosa & Fujimoto 1978) and M 81 (Sofue et al. 1980). Note that a clear magnetic spiral arm is sometimes found in the inter-arm region in such cases as that of NGC 6946 (Beck 2007).

The most simple example of the axisymmetric field is the R field, shown in the left-most panel of figure 7, though in most cases magnetic fields are aligned with spiral arms so that the R field is rarely observed. The other axisymmetric field is the ASS field, shown in the mid-left panel of figure 7. In the case of ASS, the magnetic field is symmetric about the galactic center and there is no field reversal. The mid-right hand panel of figure 7 shows the case of the BSS field, where single magnetic reversal is observed along an annulus. Recently, topology with more field reversals including the QSS (MSS) field, shown in the right-most panel of figure 7, is suggested for several galaxies (Stepanov et al. 2008).

The configuration of magnetic fields is identified by studying how the *RM* varies with the azimuthal angle about the galactic center. Azimuthal variations of *RM* in the cases of ASS, BSS, and QSS are shown in the bottom panels in figure 7. In the case of the R field, the *RM* sinusoidally changes with the azimuthal angle with a single reversal of positive and negative. Its maximum and minimum are symmetric about $RM = 0$. The *RM* of the ASS field changes in the same manner as that of the R field while the phase is shifted by a pitch angle of spiral patterns. In the case of BSS, the *RM* also changes sinusoidally but the *RM* reaches maximum (minimum) twice. In the case of QSS, the *RM*

changes sinusoidally but the *RM* reaches maximum (minimum) four times. The maximum and minimum are not necessarily symmetric about $RM = 0$ in the cases of BSS and QSS.

Observations of edge-on galaxies show that the magnetic field in the halo region is found to be X-shaped (Heesen et al. 2009). Possible explanations of such a vertical magnetic field are (i) galactic winds which blow the ISM up to the halo (Brandenburg et al. 1993) and (ii) a primordial magnetic field which runs vertically relative to the disk (Sofue et al. 2010).

Note that the large-scale BSS and V configurations of the GMF cannot be created by dynamo, but are considered to be created during the formation of primeval galaxies. On this primordial-origin hypothesis, the BSS and central vertical fields are interpreted as the fossil of an intergalactic field wound up by the primordial galaxy disk during its formation and contraction.

6.1.2 Random magnetic field

Depolarization seen in the spiral galaxy NGC 6946 implies that there are random (turbulent) magnetic fields of strength 10 μG and coherence length ~50 pc (Beck 2007). The regular magnetic field tends to align along spiral structure and ordered in the regions where turbulence is small. The turbulent field can be also described as a combination of the components parallel and perpendicular to the regular field. A high-resolution 5-GHz observation unveiled that the characteristic length of the parallel component is ~100 pc, while the perpendicular component is ~50 pc (Houde et al. 2013), indicating the existence of anisotropic turbulence.

External galaxies are by chance present in the LOS toward a background radio source. In such a case, polarization properties of the source can be altered by magnetic fields of the intervening galaxies. Mg II absorption observations indicate the existence of absorbers in front of about half of the SDSS galaxies including polarized sources such as radio galaxies and quasars (Zhu & Ménard 2013). Mg II surveys highlight the intervener's effects and allow us to investigate the strength, growth time, and coherence length of galactic dynamo in such galaxies as functions of redshift, beam covering fractions, and spatial sizes of the galaxies (Kronberg et al. 2008; Bernet et al. 2012, 2013). Investigation of such depolarizing intervening galaxies (DINGs) can allow the unbiased survey of magnetic fields in galaxies.

Figure 8 shows the relation between the total intensity spectrum index α and the polarization spectrum index β (Farnes et al. 2014a). There are two populations, an optically-thick AGN-core type ($\alpha \sim 0$) and an optically-thin radio-lobe type ($\alpha \sim 0.7$). The behavior of β depends on α; therefore, part of the depolarization takes place at the source because α should depend only on the source nature.

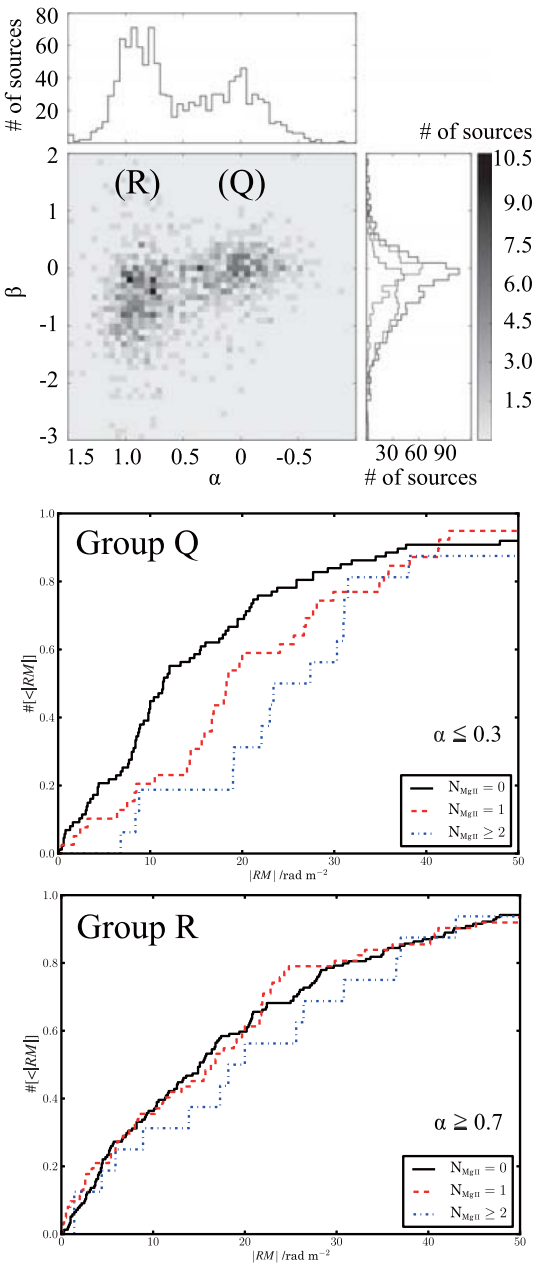

Fig. 8. (Top panel) Relation between the total intensity spectrum index α and the polarization spectrum index β for 951 sources (Farnes et al. 2014a), where the indices were derived from multiple observations between 400 MHz and 100 GHz. (Bottom two panels) Correlation between *RM* and the existence of foreground Mg II absorption systems (Farnes et al. 2014b). (Color online)

Meanwhile, Farnes et al. (2014b) suggested that there is a clear correlation between *RM* and the existence of foreground Mg II absorption systems for the AGN-core type (figure 8). Note that a DING's depolarization is caused by both regular and random magnetic fields. The latter may become more predominant at higher redshift, in accordance with the relatively longer timescale taken to form the latter.

Beck et al. (2013a) recently performed a sophisticated MHD simulation of an evolving (star-forming) galaxy, including effects of star formation, supernova magnetic seeding, and galactic wind. They demonstrated that the entire diffuse ionized gas in the galactic halo is magnetized by redshift $z \approx 0$. The magnetic field strength is at the level of a few μG in the halo center and of nG at the virial radius. The mean halo intrinsic *RM* peaks between $z \approx 4$ and $z \approx 2$ and reaches absolute values around 1000 rad m^{-2}. While the halo virializes towards $z \approx 0$, the intrinsic *RM* values decline to a mean value below 10 rad m^{-2}.

6.2 Other galaxies

6.2.1 Barred galaxies

Beck et al. (2002) investigated 17 barred galaxies and found a positive correlation between the mean radio intensity of the galaxy and the length of its bar structure. They also found a tight correlation between radio and far-infrared intensities. Such a relation is similar to that seen in non-barred galaxies, in which the relation is thought to have originated from star formation activity. Magnetic fields around the bar are stretched by shearing gas flow where the field strength is relatively large and aligned along the bar (Beck et al. 2005).

There have been a number of MHD simulations in barred galaxies. The bar-shaped gravitational potential is assumed to produce the bar structure. Kim and Stone (2012) carried out two-dimensional MHD simulations and showed that the magnetic field strength enhances the mass inflow rate to the galactic center. In the three-dimensional simulations, Kulesza-Żydzik et al. (2009, 2010) showed the formation of magnetic arms with low density around the bar. Kulpa-Dybeł et al. (2011, 2015) simulated galactic dynamo driven by CRs, and posited that the saturation level of magnetic field strength is 3–10 μG and the field structure forms the quadrupole-like symmetry with respect to the galactic plane.

6.2.2 Elliptical galaxies

Magnetic fields of elliptical galaxies have been observed based on the Faraday rotations of background radio sources behind elliptical galaxies (Perley et al. 1984; Leahy et al. 1986; O'Dea & Owen 1987; Laing & Bridle 1987; Taylor et al. 1990; Clarke et al. 1992). Elliptical galaxies have less cold-ISM forming stars and therefore little synchrotron emission from their halo regions.

Differential Faraday rotation along a LOS of the gaseous halo of a parent elliptical galaxy shows that the random magnetic field is dominant (Strom & Jaegers 1988). Meanwhile, Strom and Jaegers (1988) did not find evidence of large-scale magnetic fields in the elliptical galaxy. The random magnetic field is thought to be generated by turbulent motions which are driven by Type I supernovae and the stellar motion relative to the ISM (Moss & Shukurov 1996).

6.2.3 Dwarf galaxies

Dwarf galaxies are low-mass systems that have rotational velocities which are relatively smaller than those of spiral galaxies. Therefore, the small-scale dynamo is thought to be more significant than large-scale dynamo in the sense that the Ω-effect is weak. Observations of IC 10 and NGC 6822, both small and low-mass galaxies, support this idea since large-scale magnetic fields are not identified (Chyży et al. 2003).

Larger dwarf galaxies such as the Large Magellanic Cloud (LMC) and NGC 4449, however, seem to have regular magnetic fields due to α–Ω dynamo since they have large-scale spiral structures (Chyży et al. 2000; Gaensler et al. 2005). Whereas a regular magnetic field is found in the Small Magellanic Cloud (SMC), it is unlikely to be generated with the large-scale dynamo because of its asymmetric configuration (Mao et al. 2008). Additionally, Mao et al. (2012b) found that the H I filament in the southeast of the LMC is directed to the SMC and suggested that it formed $\sim$1 Gyr ago due to the tidal interaction between the LMC and SMC. The tidal interaction is thought to be one of the possible mechanisms that form a coherent magnetic field as found in the dwarf galaxy NGC 2976 (Drzazga et al. 2016).

6.3 Cosmological evolution

The cosmological primordial fields and the turbulent seed fields are considered to be the seed for global fields of galaxies. The advantage of the primordial field model is that global magnetic fields naturally pervade the galactic disk and that global structures such as R, ASS, BSS, and V fields are explained without contradiction (e.g., Sofue et al. 2010).

Magnetic fields generated at the inflation epoch are estimated to be $<10^{-9}$ G, observed by the CMB polarization (see section 9). During the reionization epoch, these magnetic fields are attenuated to be 10^{-10} G, and the scale of the coherent length is estimated to be about a kpc (e.g., Subramanian 2016; Pandey et al. 2015). Magnetic fields generated by the Biermann battery effect (Biermann 1950) are up to 10^{-21} G and have pc-scale coherent length (Kobayashi et al. 2007). In either case, it is necessary to amplify the weak seed fields to explain the present magnetic fields of galaxies.

Bernet et al. (2008) studied quasars in the redshift range between 0.6 and 2.0, and found that quasars with strong

Mg II line have large rotation measurements. This observational fact implies that Mg II absorption is attributed to halos of normal galaxies in the LOS to the quasar and such normal galaxies have large magnetic fields (see also Farnes et al. 2014b).

There are roughly three theoretical ways to study the cosmological evolution of the GMF. First, Arshakian et al. (2009) studied the evolution of magnetic fields in galaxies based on a dynamo theory. They suggested that μG turbulent magnetic fields can be quickly (a few 10^8 yr) generated in halos of protogalaxies from a weak seed field by the small-scale dynamo. The turbulent field can become a seed to the large-scale dynamo, and in a Milky Way type galaxy, μG coherent magnetic fields on scales of kpc and tens of kpc are established until $z \sim 3$ and $z \sim 0.5$, respectively, by the large-scale dynamo.

Secondly, MHD simulations of the galactic dynamo have been carried out (e.g., Nishikori et al. 2006; Hanasz et al. 2009). Although the main mechanisms of amplification were not necessarily the same, initial weak magnetic fields can be successfully amplified up to a few μG and the amplified fields are maintained during several billions of years. Gressel, Elstner, and Ziegler (2013) included the effect of the amplification of the supernovae by $\alpha - \Omega$ dynamo terms and turbulent dynamo was treated by MHD (called Hybrid dynamo). They demonstrated a mixture of modes with even and odd parities, which creates a strong localized vertical field on one side of the galactic disk. Machida et al. (2013) presented the all-sky map of *RM* obtained from their numerical simulation, and suggested that the magnetic fields generated by MRI–Parker dynamo explain the tendency of observed *RM* distribution.

Thirdly, cosmological simulations of galaxy formations have been performed by the AREPO group (e.g., Pakmor et al. 2014). They assumed weak random magnetic fields and the standard ΛCDM cosmology. They suggested that ordered magnetic fields of about 6 μG in strength were formed until $z \sim 2$.

Finally, an environmental effect would be another important factor of the cosmological evolution of the GMF. It is well known that galaxies in the Virgo cluster suffer environmental effects such as ram pressure stripping (Cayatte et al. 1990; Nakanishi et al. 2006). Weżgowiec et al. (2012) and Vollmer et al. (2013) investigated magnetic fields of Virgo cluster galaxies based on radio observations with the 100-m Effelsberg telescope and the Jansky Very Large Array. They studied asymmetric polarized emission indicating distorted magnetic field structures. According to their investigations, galaxies such as NGC 4294, NGC 4298, NGC 4302, NGC 4303, NGC 4321, and NGC 4568 seem to have experienced tidal interactions, NGC 4532 and NGC 4808 are likely to have huge accreting H I envelopes, NGC 4388 and NGC 4505 seem to have experienced strong ram-pressure and shearing effects, and NGC 4457 seems to have had a recent minor merger. The magnetic field is a good indicator for tracing even weak interactions, which are difficult to detect with other observations.

7 AGN and jet

Magnetic fields significantly affect the physics of accretion disks, black holes, and jets. They also induce radio emission, which is used to classify AGN and jets. We review a role of magnetic field in AGN and astronomical jets in this section.

7.1 Radio classification of AGN and jets

AGN have been known as a radio source since Cygnus A was detected at 160 MHz in 1944 (Reber 1944) and identified as a radio point source in 1948 (Bolton & Stanley 1948). In the 1950s–60s, radio source catalogs, known as 3C members, were compiled by the group at the University of Cambridge (Edge et al. 1959; Bennett 1962). The catalogs opened the door to the research field of AGN; the generation mechanisms of the energy, the objects responsible for the emission (supermassive black holes), and magnetic fields have been intensively studied. Radio sources 3C 273 and 3C 48 were discovered as enormously high-redshift sources in 1963 (Greenstein 1963; Hazard et al. 1963; Oke 1963; Schmidt 1963), which means that they are very distant objects and are producing a huge amount of energy, and a new classification of "quasars" was established.

One of the classes of AGN is based on radio emission. AGN are classified into two groups, conventionally called "radio-quiet" and "radio-loud." Radio-quiet AGN include low-ionization nuclear emission-line regions (LINERs), Seyfert galaxies, and radio-quiet quasars. Radio-loud AGN include radio galaxies, blazars, and radio-loud quasars. Details of the above classifications can be found in the literature (Netzer 2015). We note that AGN radio emission can be tightly related to magnetic fields. Therefore, the above classification based on radio emission can be influenced by magnetic fields.

AGN often exhibit collimated jets which emit synchrotron radiation over a wide range in radio (Shulevski et al. 2015; Hada et al. 2016). Fanaroff and Riley (1974) measured the distance between two peaks of radio lobes, and suggested that galaxies possessing radio lobes can be classified into two classes based on $R_{\rm FR}$, the ratio of the distance to the extent of the contour of lowest brightness (Fanaroff–Riley classification). Galaxies with $R_{\rm FR} < 0.5$ and

$R_{\rm FR} > 0.5$ are classified into FR I and FR II, respectively. FR II galaxies have relatively larger radio luminosities than FR I galaxies. Jets from FR II galaxies have larger opening angles and have hot spots at their terminal. On the contrary, jets from FR I galaxies have small opening angles and no hot spots are found. Based on observations of synchrotron emission, the typical magnetic field strength inside radio lobes is 3–10 μG (Migliori et al. 2007).

Based on the distribution of *RM*s and the intrinsic polarization angles, Asada et al. (2002) pointed out helical magnetic fields operating along the jet in 3C 273. A few tens of AGN possess such helical magnetic field structures of jets (Gabuzda et al. 2015). VLBI observations show that a jet has a cylindrical structure (Nagai et al. 2014). Proper motions of jet knots were detected through VLBI monitoring observations and super-luminous motions were found in some cases (Asada et al. 2014). Recently, using ALMA, Martí-Vidal et al. (2015) found a strong polarization signal from the jet of a distant AGN, PKS 1830−211. They estimated magnetic fields of at least tens of Gauss on scales of 0.01 pc from observed large *RM*s. Hada et al. (2016) reported a highly polarized (∼20%) feature at about 50 Schwarzschild radii from the core. Because depolarization is expected during the propagation along the LOS, they suggested that the intrinsic polarization degree must be higher than the observed one and hence a well-ordered magnetic field is present in this region.

The current plausible scenarios of the formation of relativistic jets are (1) magnetic acceleration model (Uchida & Shibata 1985; Koide et al. 2002) and (2) radiation-driving model (Iwamoto & Takahara 2004; Asano & Takahara 2009; Toma & Takahara 2012). The origin of AGN activities and jets is considered to occur on the surface of an accretion disk surrounding a central supermassive black hole. According to the standard theory of accretion disks, stable branches of accretion disks can be classified into the radiatively inefficient accretion flows (RIAF), the standard disk, and the slim disk (Abramowicz et al. 1995). Here, the RIAF describes an optically thin disk, and the latter two exhibit optically thick disks. The standard disks are thermal-pressure supported, while slim disks are supported by radiative pressure. A link between AGN activities and the accretion disk state is that the low-luminosity AGN, Seyfert, and narrow-line Seyfert I galaxies possess a RIAF-like disk, a standard disk, and a slim disk, respectively. No drastic difference of magnetic field strength and structure is reported among the three disks. However, the magnetic field plays an essential role in the accretion disk state, in the sense that magnetic turbulence produced by MRI governs the efficiency of viscosity and the viscous energy (e.g., Balbus & Hawley 1991).

7.2 Seyfert galaxies and magnetic fields

According to features of optical and UV absorption lines, some galaxies are classified into Seyfert Types I or II; spectra of Type I show both broad and narrow lines while spectra of Type II show only narrow lines. The broad lines have widths of up to 10^4 km s^{-1} and the narrow lines show much smaller velocities (a few $\times$ 100 km s^{-1}). In addition, about 10%–20% of quasars exhibit "ultra-fast outflow," blue-shifted absorption lines with velocities of about 10000 km s^{-1} with respect to the galaxy's rest frame, and line widths of about 2000 km s^{-1} (Weymann et al. 1991). Similar blue-shifted absorption lines were also observed in X-rays (Pounds et al. 2003; Tombesi et al. 2010).

The "unification scheme" of Seyfert galaxies is often cited to explain the difference between Types I and II (Antonucci & Miller 1985). In this theory, high-velocity clouds are moving around the supermassive black hole and they are responsible for the broad lines. A dusty molecular gas torus partially surrounds the "broad line region." The difference between Types I and II is caused by the direction of the AGN axis with respect to the LOS. In Type II the torus is inclined and blocks the observer's direct view to the broad line region. In Type I the torus is almost face-on and the observer can see the broad line region. Radio-quiet quasars and QSOs are more luminous than Seyferts. Since the optical luminosity is so large, the host galaxy is not visible. Like Seyferts, quasars are classified as Types I and II. The spectra of Type I have both broad and narrow lines, while those of Type II have only narrow lines. In addition, so as to explain the ultra-fast outflow, some theoretical models, e.g., the line-driven acceleration (Nomura et al. 2016) and the magnetic disk wind (Fukumura et al. 2016), have been proposed.

The polarization vector of a Type II Seyfert galaxy tends to be aligned along the rotation axis, and the polarization degree is significant, 1%–10%. On the other hand, a Type I Seyfert galaxy shows low polarization degree (0.1%–1%) and the polarization vector becomes perpendicular to the rotation axis. For example, Smith et al. (2002) observed 36 Seyfert I galaxies with the Willam Hershel and Anglo-Australian Telescopes to obtain the optical spectropolarimetry. They found that 20 out of the 36 Seyfert I galaxies exhibit linear polarization of the broad line region. Marin (2014) compiled 53 AGN from archival data, and suggested that the above tendency could originate from the inclination angle of the AGN.

The magnetic field strength around the emission region is presumed to be about $O(10)$ G (Martí-Vidal et al. 2015). The azimuthal magnetic field is considered to be the dominant component (Silant'ev et al. 2013). The method of black hole mass estimation is proposed using the relation

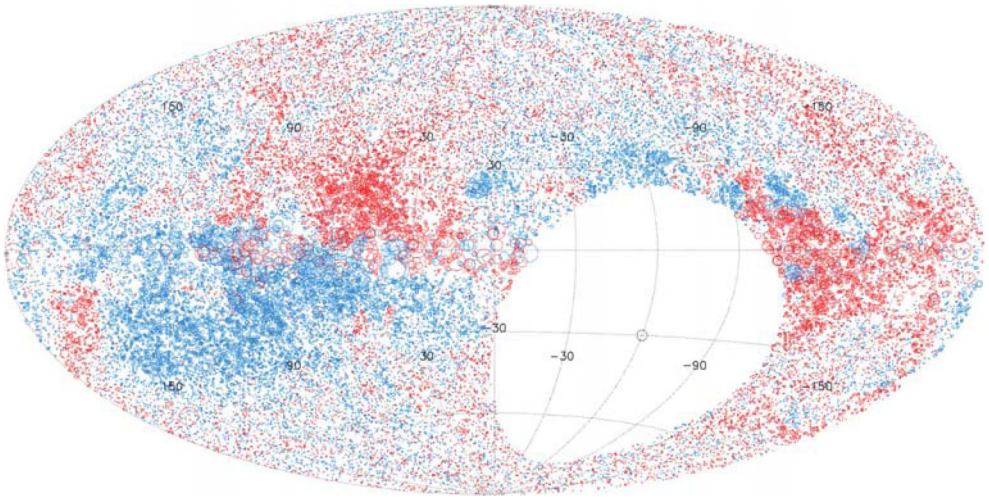

Fig. 9. Longitude–latitude map of *RM*s obtained from the NRAO VLA Sky Survey (NVSS: Taylor et al. 2009). The size and color of each circle shows the amplitude of *RM* and its sign (red: positive; blue: negative), respectively, of each extragalactic source (mostly radio galaxy or quasar, i.e., AGN). (Color online)

between the polarization degree and the inclination angle (Piotrovich et al. 2015).

7.3 Cosmological evolution of AGN magnetic fields

Figure 9 shows the largest (37543) *RM* catalog of extragalactic polarized sources to date (Taylor et al. 2009). Some of the sources are nearby ($z < 0.2$) radio galaxies and others are quasars distributing in a wide range of redshift, $0 < z < 5$ (Hammond et al. 2012). Using such a massive extragalactic *RM* catalog, a number of works have attempted to extract cosmological evolution of magnetic fields associated with AGN and quasars (e.g., Kronberg et al. 2008; Xu & Han 2014). Although these works still suffer from large errors of *RM* measurement, a current consensus would be that at least the standard deviation of the residual (observed − galactic foreground) *RM*s is constant in redshift at a $\sim$10 rad m^{-2} level. Since contributions from DINGs and the IGM can be minor in the nearby universe, the standard deviation for nearby sources can be associated mostly with AGN, AGN host galaxies, or ambient media, and it decreases by $(1+z)^{-2}$ in a passive evolution scenario (Akahori et al. 2014a). Note that careful collection of *RM* data is important because *RM* strongly depends on the frequency and the beam size due to depolarization (e.g., Bernet et al. 2012, 2013; Farnes et al. 2014a, 2014b).

Wide-band polarimetry is powerful for studying structures of AGN jets which are located too far away to be resolved. Figure 10 introduces the result for a distant quasar PKS B1610−771 (O'Sullivan et al. 2012; Gaensler et al. 2015). Vertical dashed lines indicate the 350-MHz bandwidth centered at 1.4 GHz. If the data only in this bandwidth is available, one may notice a simple linear relation between the polarization angle and λ^2, and obtain the best fit of $RM = +135$ rad m^{-2} with a single *RM* component. However, full bandwidth data (1.1–3.1 GHz) reveals that a single *RM* component does not fit the full data well (left-hand panels) and reminds us of the complex *RM* structures. An external Faraday dispersion depolarization model [equation (35)] improves the fit at the short wavelengths but fails to adequately fit the long-wavelength data (middle panels). Accordingly, the full data can be nicely fitted with a two-component model with *RM*s of $+107.1 \pm 0.2$ rad m^{-2} and $+78.7 \pm 0.4$ rad m^{-2} (right-hand panels). O'Sullivan et al. (2012) suggested that these components are polarized knots of unresolved jets.

8 Galaxy clusters

Information on cluster magnetic fields is obtained from observations of polarized radio sources inside or behind galaxy clusters. It is well known that some galaxy clusters contain diffuse synchrotron sources which allows the estimation of the IGMF in the ICM. In addition, since polarization from the polarized radio sources is affected by Faraday rotation due to thermal electrons within magnetic fields in the ICM, we can calculate *RM* and infer properties of the magnetic fields in the ICM. In this section, we review three types of diffuse synchrotron emissions from galaxy clusters, radio halo, radio mini-halo, and radio relic, in that order, and summarize observations of *RM* toward galaxy clusters.

8.1 Radio halo

Radio halos are diffuse synchrotron emission observed in the central region of galaxy clusters. According to the review by Feretti et al. (2012), radio halos have low surface

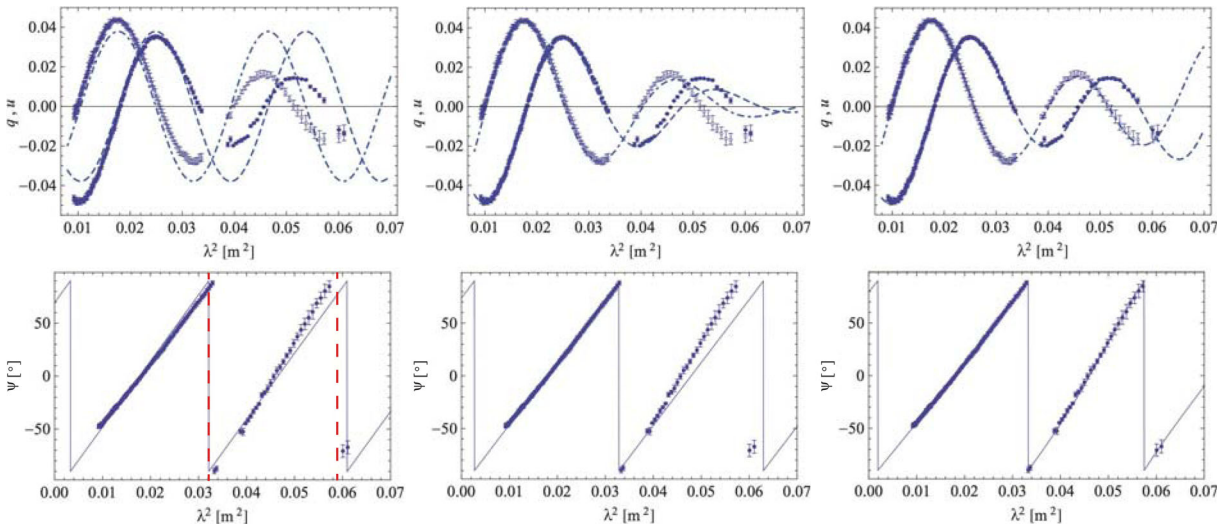

Fig. 10. Polarization spectra of Quasar PKS B1610−771 (O'Sullivan et al. 2012; Gaensler et al. 2015). Top panels show normalized Stokes q (= Q/I, open circles) and u (= U/I, filled circles) and the bottom panels show the polarization angle Ψ (filled circles) against the wavelength squared. Vertical red solid lines indicate the 350 MHz bandwidth centered at 1.4 GHz. Dot–dashed, dashed, and solid lines show the best-fits of q, u, and Ψ, respectively. The panels show the results with a single *RM* component (left), a single depolarization screen (middle), and two *RM* components (right). (Color online)

brightness ($\sim$0.1–1 μJy arcsec^{-2} at 1.4 GHz) and a steep radio spectrum ($\alpha > 1$). Their linear size ranges from several hundred kpc to a few Mpc. A deep survey of X-ray selected galaxy clusters with the GMRT shows that only 30% of clusters with $L_{\rm X} > 5 \times 10^{44}$ erg s^{-1} host radio halos (Cassano et al. 2011). Most radio halos are observed in clusters which are undergoing sub-cluster merging. Several properties from radio and X-ray observations can be interpreted in terms of a merging scenario as will be described below.

It is possible to constrain the magnetic field strength in clusters with radio halos through observations of synchrotron radio and non-thermal X-ray radiation due to inverse Compton (IC) scattering of cosmic microwave background (CMB) photons (for reviews, Rephaeli et al. 2008; Ota 2012). If we detect non-thermal X-ray emission, we can estimate mean field strength for radio halo clusters using the relation between the synchrotron radio flux $F_{\rm radio}$ and the X-ray flux $F_{\rm ICX}$:$F_{\rm radio}/F_{\rm ICX} = U_{\rm mag}/U_{\rm CMB}$, where $U_{\rm mag}$ and $U_{\rm CMB}$ are the energy density of magnetic field and CMB photons, respectively. Suzaku has searched for non-thermal hard X-rays in several clusters hosting radio halos with the Hard X-ray Detector (HXD) which has a low detector background and a narrow field of view.

The Coma radio halo, which has a flux density of $F_\nu \sim 530$ mJy at $\nu = 1.4$ GHz, is a well-known radio halo source. The magnetic field strength is estimated to be a few μG using the *RM*s of the radio emission (Kim et al. 1990). Wik et al. (2009) analyzed hard X-ray observations from the Coma cluster with Suzaku HXD-PIN and XMM-Newton data and failed to find a statistically significant contribution from the non-thermal component. The upper limit they obtained on the flux of the non-thermal component is $F_{\rm X} < 6 \times 10^{-12}$ erg s^{-1} cm^{-2} in the 20–80 keV band, corresponding to the lower limit of the magnetic field of 0.15 μG.

Abell 2319 possesses a giant radio halo ($F_\nu \sim 1$ Jy at 610 MHz, $\alpha \sim 0.92$) which is more powerful than that of the Coma cluster. In this cluster two subgroups are merging almost along the LOS with the velocity difference of $\sim$3000 km s^{-1}. Sugawara, Takizawa, and Nakazawa (2009) found the upper limit of the IC component to be $F_{\rm X} < 2.6 \times 10^{-11}$ erg s^{-1} cm^{-2} in the 10–40 keV band, which means that $B > 0.19$ μG.

Abell 2163 is known as the hottest cluster and also hosts a powerful radio halo ($F_\nu \sim 155$ mJy at 1.4 GHz, $\alpha \sim 1.18$). A complex structure of the hot gas temperature suggests that this cluster is undergoing sub-cluster merging. Weak lensing observation also supports the merging (Okabe et al. 2011). Ota et al. (2013) analyzed the hard X-ray spectrum and concluded that the observed spectrum is well explained by the multi-temperature thermal emission model. The obtained upper limit is $F_{\rm X} < 1.2 \times 10^{-11}$ erg s^{-1} cm^{-2} in the 12–60 keV band, which means that $B > 0.098$ μG.

The origin of CR electrons responsible for the radio halo emission is still under debate. Since the life-time of the CR electrons, mainly due to the IC losses, is short ($\sim 10^7$–10^8 yr), CR electrons have to be injected or (re)accelerated in the clusters which possess radio halos (Sarazin 1999; Brunetti et al. 2001). Shock waves which propagate in the ICM during sub-cluster merging can

accelerate CRs (e.g., Takizawa & Naito 2000; Miniati et al. 2001; Vazza et al. 2009, 2016). Numerical simulations show that MHD turbulence is developed during the sub-cluster merging (Takizawa 2008; Vazza et al. 2011; Beresnyak et al. 2013). Driven MHD turbulence can also accelerate CRs (e.g., Schlickeiser 2002). In addition, inelastic collisions between CR protons and thermal protons generate secondary CR electrons (e.g., Dennison 1980; Blasi & Colafrancesco 1999). Brunetti and Jones (2014) discuss these injections and acceleration mechanisms of CRs in detail.

Radio and X-ray observations for radio halo clusters indicate the correlation of $P_{1.4} \propto L_{\rm X}^{s}$, where $P_{1.4}$ is the monochromatic radio power at 1.4 GHz and $L_{\rm X}$ is the X-ray luminosity, and the index is $s \sim 2$. Cassano, Brunetti, and Setti (2006) and Cassano (2010) interpreted this slope by assuming a magnetic field dependence on the cluster mass. Brunetti et al. (2007) found that upper limits of the radio power for clusters without radio halos lie about one order of magnitude below this correlation, and suggested the bimodal distribution in the $P_{1.4}$–$L_{\rm X}$ plane. Since radio halos are associated with merging clusters and clusters with the upper limits are relaxed clusters, Brunetti et al. (2009) interpreted this bimodality in terms of the turbulent acceleration model during cluster merging as below. Cluster merging can supply energy both to the hot gas and CRs through shocks and/or turbulence. The CR electrons, which are accelerated by turbulence generated through cluster merging, emit synchrotron radiation in radio halo clusters. In relaxed clusters after merging events, the CR electrons lose their energy and then radio halos disappear.

Synchrotron radio spectrum is determined by cosmic-ray acceleration and the acceleration efficiency is affected by the power spectrum of MHD turbulence. Motivated to explain radio spectrum, several attempts have been made to clarify the power spectrum of MHD turbulence in galaxy clusters. MHD turbulence which consists of Alfvén waves or magnetosonic waves has been assumed, because these waves accelerate CRs through resonant interaction (e.g., Petrosian 2001; Fujita et al. 2003; Brunetti et al. 2004; Brunetti & Lazarian 2007, 2011). Ohno et al. (2002) constrained the power spectrum $P(k)$ so as to reproduce the radio spectrum of the Coma radio halo. They obtained $P(k) \propto k^{-2.8}$, which is steeper than the Kolmogorov power spectrum. Recently, Fujita et al. (2015) proposed a model in which turbulence behind a shock re-accelerates CR electrons that had been weakly accelerated at the shock. They applied their model to the clusters 1RXS J0603.3+4214 (the Toothbrush Cluster) and 1E 0657−56 (the Bullet Cluster) and found that the effective mean free path for efficient acceleration must be much smaller than the Coulomb mean free path.

The observed integrated spectra from several radio halos show spectral steepening at high frequency ($\nu \sim 1$ GHz) (Feretti et al. 2012). Also, spatial distribution of the spectral index has been measured from several radio halos. We may investigate MHD turbulence through measurements of spectral steepening at high frequency and spatial variation of the radio spectrum combined with theoretical studies.

8.2 Radio mini-halo

Radio mini-halos are diffuse radio synchrotron emission that are found around the cores of galaxy clusters. They are often observed in non-merging clusters in contrast with cluster-scale giant radio halos (Feretti et al. 2012; Giacintucci et al. 2014). This may indicate that the origin of the mini-halos is different from that of the giant radio halos. The mini-halos are generally dim, which has prevented us from understanding their origin.

Hadronic and leptonic models have been considered as the origin of mini-halos. In hadronic models, synchrotron emissions come from secondary electrons created through *pp*-interaction between CR protons and thermal protons in the ICM (Pfrommer & Enßlin 2004; Fujita et al. 2007; Keshet & Loeb 2010; Fujita & Ohira 2011; Enßlin et al. 2011). In leptonic models, electrons are re-accelerated by turbulence in the ICM (Gitti et al. 2002; ZuHone et al. 2013).

For the hadronic models, the origin of protons are often thought to be the AGN in the core of the cluster. In fact, some studies indicate that jets launched by the AGN have a large fraction of CR protons (Sikora et al. 2005). Moreover, CR protons may be efficiently accelerated in a RIAF disk of the AGN (Kimura et al. 2015). Since most of the AGN at cluster centers at low redshifts are dim and are expected to have RIAFs (Russell et al. 2013), a huge amount of CR protons may be flowing out of them in cluster cores. Those CR protons cannot move freely because they interact with magnetic fields in the ICM. Moreover, they are likely to excite Alfvén waves in the ICM through the streaming instability (Skilling 1975). Since the CR protons are well scattered by the waves, the protons as a whole move slowly with the waves at the Alfvén velocity (CR streaming). The slow bulk motion of the CRs works as a PdV work, for which the heating rate is proportional to the production of the Alfvén velocity and the gradient of CR pressure. Thus, CR streaming effectively heats the ICM and compensates for the radiative ICM cooling in the core (Böhringer & Morfill 1988; Guo & Oh 2008; Fujita et al. 2013; Jacob & Pfrommer 2017).

Since the above heating mechanism does not require turbulence, it is consistent with the results of Hitomi that showed only a low level of turbulence ($\sim$164 km s^{-1}) in the

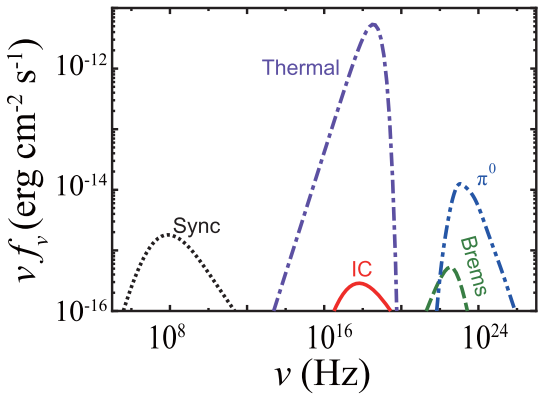

Fig. 11. Predicted broad-band spectra of RX J1347−1145 based on the secondary CR scenario by Fujita and Ohira (2013). Synchrotron radiation (dotted line), inverse Compton scattering off CMB (solid line), and non-thermal bremsstrahlung (dashed line) are of the secondary electrons. The π^0-decay gamma-rays are shown by the double-dot–dashed line. For comparison, the thermal bremsstrahlung from the ICM is shown by the dot–dashed line. Redshift has been corrected. (Color online)

core of the Perseus cluster (Hitomi Collaboration 2016). At the same time, those CR protons create secondary electrons via *pp*-interaction, and they radiate synchrotron radio emissions.

This process proceeds on the timescale of the Alfvén crossing time of the core:

$$T_{\rm A} = L/v_{\rm A} \sim 4.5 \times 10^8 \ {\rm yr} \left(\frac{L}{100 \ {\rm kpc}}\right) \times \left(\frac{n}{10^{-2} \ {\rm cm}^{-2}}\right)^{1/2} \left(\frac{B}{10\mu \ {\rm G}}\right)^{-1}, \quad (47)$$

where L is the core size, $v_{\rm A}$ is the Alfvén velocity, n is the ICM density, and B is the magnetic field strength. The cooling time of the CR protons by the *pp*-interaction is larger than $T_{\rm A}$ and thus the cooling can be ignored. On the other hand, the electrons created via the *pp*-interaction lose their energy by synchrotron radio emission. With the Lorentz factor γ, the synchrotron cooling time is given by

$$T_{\rm s} \sim 2.4 \times 10^7 \ {\rm yr} \left(\frac{\gamma}{10^4}\right)^{-1} \left(\frac{B}{10\mu \ {\rm G}}\right)^{-2}, \quad (48)$$

and is much shorter than $T_{\rm A}$.

This means that the secondary electrons cool almost immediately after their birth ($\sim T_{\rm s}$), while the CR protons injected by the central AGN can exist in the cluster core on a timescale of $\sim T_{\rm A}$. Thus, the synchrotron emissions from the secondary electrons should be generated near the site of the *pp*-interaction, which can be far away from the site of the proton injection (AGN). A prediction of broad-band spectra of an hadronic model is shown in figure 11. In addition to the synchrotron emission, weak gamma-ray emission associated with *pp*-interaction should be generated, although it would be difficult to discriminate it from that from the central AGN in the near future.

In leptonic models, the short cooling time of the CR electrons [equation (48)] means that the synchrotron emission is basically produced where the electrons are re-accelerated, because they do not have enough time to diffuse for a long distance. Thus, the synchrotron emission shows the position of turbulence. The turbulence that Hitomi has found in the core of the Perseus cluster may be strong enough to accelerate electrons to the energies required for the synchrotron emission (Hitomi Collaboration 2016). However, ultimately, the spatial correlation between the synchrotron emission and turbulence must be confirmed to prove the leptonic models. The results of the Hitomi observations suggest that the turbulence in the Perseus cluster is not originated from the central AGN, because it is too weak to propagate from the central AGN. This may show that the turbulence is created via gas sloshing caused by minor cluster mergers (Fujita et al. 2004; Ascasibar & Markevitch 2006).

8.3 Radio relic

Radio relics are diffuse, non-thermal, synchrotron radio-emitting regions, which are often found in the outskirts of merging clusters. They are typically arc-shaped and convex towards the outer regions of the cluster, whereas some of them show linear-shaped or knotty and irregular morphology (Feretti et al. 2012). Such a variety of morphology likely indicates inhomogeneous distribution of CR electrons and/or magnetic fields, and could imply different formation processes. Their radio spectra typically show a power-law shape that has a radio spectral index of $\alpha \sim 1$. However, some relics show significantly steeper spectra. In addition, a curved radio spectrum and spectral break are reported in recent detailed radio observations (Stroe et al. 2013, 2016).

It is believed that CR electrons in radio relics are accelerated at shocks associated with cluster formation, which is consistent with the facts that shock structures are found in the ICM density and temperature distributions near the relics through X-ray observations (Finoguenov et al. 2010; Akamatsu et al. 2012; Akamatsu & Kawahara 2013) and that significant polarization degree is often observed in radio observations (van Weeren et al. 2010, 2012; Ozawa et al. 2015). DSA (diffusive shock acceleration) is the most promising particle acceleration process. Assuming a simple case of DSA, the Mach number of the shocks ($M_{\rm Radio}$) is estimated with the index ($\alpha_{\rm int}$) of integrated radio spectra as follows:

$$M_{\rm Radio}^2 = \frac{2\alpha_{\rm int} + 2}{2\alpha_{\rm int} - 2}. \quad (49)$$

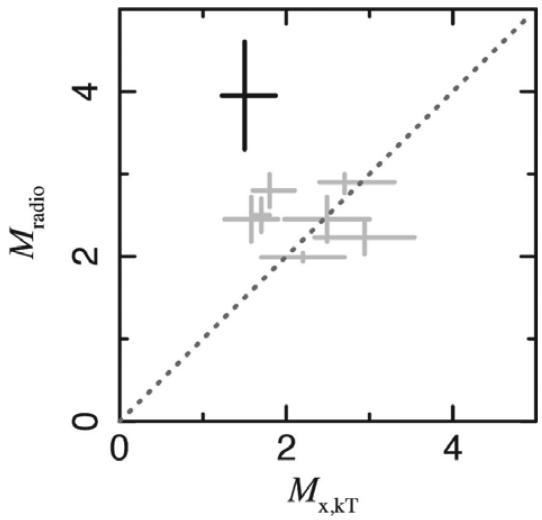

Fig. 12. Mach numbers derived from the radio spectral index (M_{radio}) plotted against those from the X-ray temperature measurements ($M_{X,kT}$) for eight radio relics from Itahana et al. (2015). The gray dotted line represents $M_{radio} = M_{X,kT}$. The result of the "toothbrush" is shown by a black cross, which seems to be a rather extreme case. References for each relic are listed in Itahana et al. (2015).

On the other hand, X-ray observations of the ICM enable us to determine the Mach number (M_X) through a temperature or density jump across the relics with the Rankine–Hugoniot conditions:

$$\frac{T_2}{T_1} = \frac{5M_X^4 + 14M_X^2 - 3}{16M_X^2}, \tag{50}$$

$$\frac{\rho_2}{\rho_1} = \frac{4M_X^2}{M_X^2 + 3}, \tag{51}$$

where T_1 and T_2 (ρ_1 and ρ_2) are the pre- and post-shock temperatures (densities), respectively, assuming a specific heat ratio γ of 5/3. Both methods should lead to results consistent with each other if a simple DSA theory holds. Akamatsu and Kawahara (2013) provided the first systematic study about this issue. The recent results from Itahana et al. (2015) are shown in figure 12, where significant differences between M_{radio} and M_X are seen for some relics. This indicates some hints of the particle acceleration process in the relics.

Non-thermal electrons attributed to radio relics also emit non-thermal hard X-rays through inverse Compton scattering of CMB photons. Comparison of synchrotron and inverse Compton fluxes enables us to estimate the magnetic field strength. However, it is still difficult to detect such emission because thermal emission from the ICM is dominant in the X-ray band though relics are often in the outskirts where thermal emission is fainter. At present, only upper limits of the inverse Compton component and hence lower limits of the field strength are obtained (Ajello et al. 2009, 2010; Kawano et al. 2009; Nakazawa et al. 2009; Itahana et al. 2015).

In a theoretical model based on a simple DSA, the index of integrated radio spectrum α_{int} and that of just behind the shock α_{inj}, which reflect the CR electron energy spectrum just accelerated at the shocks, have a relation of $\alpha_{int} = \alpha_{inj} + 0.5$ because of synchrotron and inverse Compton cooling (Sarazin 1999). However, recent detailed radio observations reveal that such a simple picture cannot explain some relics at least. For example, spectral curvature is found in the "sausage" relic of CIZA J2242.8+5301 (Stroe et al. 2013). In addition, the "toothbrush" relic in 1RXS J0603.3+4214 shows spectral steepening in a higher frequency range, which cannot be explained by the cooling (Stroe et al. 2016). These facts, as well as the Mach number discrepancy mentioned above, mean that we need more elaborate theoretical modeling. For example, in a re-acceleration scenario (Brunetti et al. 2001), where the electrons in the relic have already been accelerated once at shocks with a much higher Mach number, such as virial shocks, the Mach number discrepancy could occur. Interplay between shock and turbulence acceleration is considered in Fujita et al. (2015).

8.4 Cluster *RM* and magnetic turbulence

Polarized emissions from radio sources inside or behind galaxy clusters mainly pass through three different components. Those are the polarized radio source itself, the ICM, and the Milky Way (MW). Hence the total *RM* is the sum of their *RM*s:

$$RM = RM_{source} + RM_{ICM} + RM_{MW}. \tag{52}$$

The first significant detection of the ICM *RM* was made by Lawler and Dennison (1982), using radio galaxies in dozens of clusters. They compared *RM*s of 12 radio galaxies seen in the inner part of the clusters with those of 46 radio galaxies seen in the outer part of the clusters, and found that the distribution of the *RM* values of the former population is broadened. For Abell 2319, Vallée et al. (1986) calculated the *RM*s of 10 radio sources inside and outside of the cluster core, and found that the *RM*s of the sources inside the cluster core show positive values, in contrast to those outside of the core. Both results indicate that the polarization is affected by Faraday rotation in the ICM and clearly suggest the existence of IGMF.

Thanks to high-sensitivity and high-resolution observation instruments, we can unveil the spatial distribution of

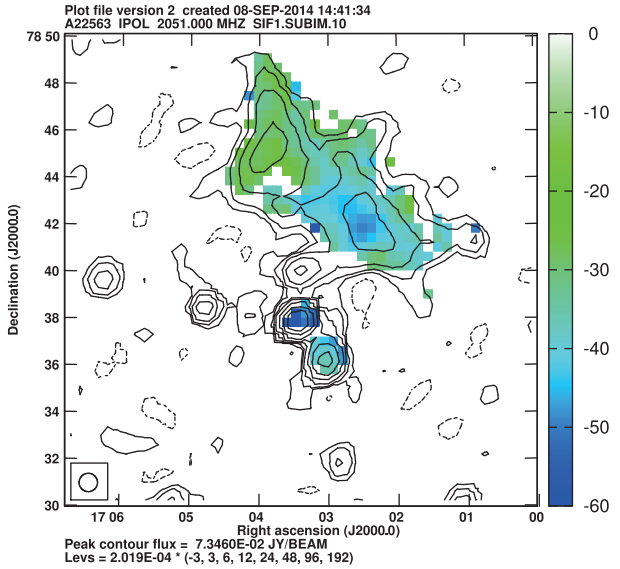

Fig. 13. RM spatial distribution of Abell 2256 observed with the Karl G. Jansky Very Large Array (JVLA). Black contours show the total intensity at 2051 MHz. The emission to the northwest is a radio relic and two polarized radio sources are located near the center of the map. (Color online)

RM using individual polarized sources inside or behind clusters (see figure 13). High-resolution images revealed that *RM* spatial distribution is patchy and *RM* probability distribution is Gaussian, indicating the existence of magnetic turbulence on scales of several kpc (e.g., Bonafede et al. 2010; Govoni et al. 2010; Vacca et al. 2012; Ozawa et al. 2015). Since the probability distribution indicates a non-zero mean *RM*, large-scale magnetic fields would also be expected in addition to the small-scale magnetic fields due to turbulence.

The three-dimensional structure of the IGMF can be complicated due to the magnetic turbulence. In order to derive the profile of the magnetic turbulence, several authors analyzed the ICM *RM*s using a single-scale cell model (e.g., Lawler & Dennison 1982; Tribble 1991; Feretti et al. 1995; Felten 1996; Govoni et al. 2010). The model consists of a lot of cells with a uniform size, and each cell includes electrons with a uniform density and magnetic fields with a uniform strength with a single scale and a random direction. In this case, the *RM* probability distribution becomes a Gaussian with zero mean, and the variance of the *RM* in rad m^{-2} is given by

$$\sigma_{RM}^2 = 812^2 \Lambda_c \int (n_e B_\parallel)^2 dl, \tag{53}$$

where Λ_c represents a single scale of the magnetic field in kpc, n_e is the thermal electron density in cm^{-3}, and $B_\parallel$ is the magnetic field strength along the LOS in μG. For the thermal electron density n_e, we assume the β-model,

$$n_e = n_0 \left(1 + \frac{r^2}{r_c^2}\right)^{-3\beta/2}, \tag{54}$$

where n_0 is the central electron density, r is the distance from the X-ray center, and r_c is the core radius of the ICM. Then, the equation (53) is expressed as

$$\sigma_{RM} = \frac{K B n_0 r_c^{1/2} \Lambda_c^{1/2}}{(1 + r^2/r_c^2)^{(6\beta-1)/4}} \sqrt{\frac{\Gamma(3\beta - 0.5)}{\Gamma(3\beta)}}, \tag{55}$$

where $B = \sqrt{3 B_\parallel}$ and Γ represents the Gamma function. K is the constant, which depends on the integration length over the thermal electron density distribution; $K = 624$ if the radio source is located behind the cluster and $K = 441$ if the radio source is located halfway through the cluster. Hence, we can estimate the magnetic field strength by measuring the standard deviation of the *RM* if we assume the electron density of the ICM and Λ_c.

The above analysis leads to a reliable estimation if we assume the magnetic field correlation length Λ_B as Λ_c (Murgia et al. 2004). However, since the single-scale cell model does not meet div$B = 0$ and MHD simulations require wide-range fluctuations of the spatial scale of the magnetic turbulence (Enßlin & Vogt 2003; Vogt & Enßlin 2003), a more realistic model is required. Murgia et al. (2004) developed the software FARADAY, which simulates a *RM* map from a three-dimensional electron density model and a multi-scale magnetic field model. The model assumes random magnetic fields and a power-law power spectrum $|B_k|^2 \propto k^{-n}$ with cutoffs at the minimum and maximum scales. It also assumes a correlation between the thermal electron density and the magnetic field strength. Comparison between a simulated *RM* map and an observed *RM* map can quantify the profile of the magnetic fields. Guidetti et al. (2008) analyzed magnetic fields in Abell 2382 using FARADAY. They verified the model parameters in order to reproduce the observed *RM* map, and found that the magnetic field power spectrum index is the Kolmogorov one, $n = 11/3$, suggesting the presence of Kolmogorov-like magnetic turbulence.

The Kolmogorov-like magnetic turbulence is predicted in an MHD simulation performed by Ryu et al. (2008). They proposed a scenario that seed magnetic fields are amplified by turbulent-flow motions in the IGM induced by the cascade of vorticity generated at cosmological shock waves during the large-scale structure formation. In this simulation, they found that the turbulence energy $\epsilon_{\rm turb}$ is converted into the magnetic energy ϵ_B as

$$\epsilon_B = \phi \left(\frac{t}{t_{\rm eddy}}\right) \epsilon_{\rm turb}, \tag{56}$$

where ϕ is the conversion factor and $t_{\rm eddy}$ is the eddy turnover time, respectively. The power spectra of the amplified magnetic fields roughly indicated the Kolmogorov-like power spectra. Whatever the origin is, the magnetic fields should be affected by the turbulence in the ICM.

9 The cosmic web

Magnetic fields appear whenever currents can be found. This means that magnetic fields potentially exist in the whole range of the universe from scales of particle physics to cosmology. We expect that cosmological magnetic fields affect a variety of cosmological phenomena, Big Bang nucleosynthesis (BBN), the CMB, the matter power spectrum (MPS), and the large-scale structure formation. In this section, we introduce several theories on the origin of cosmological magnetic fields, and their effects on the early universe and the structure formation. We also summarize the current state of the art in the observations for cosmological magnetic fields.

9.1 Primordial magnetic fields in early universe

Can the early universe create cosmological magnetic fields? Since we have not had any effective methods for observing primordial magnetic fields (PMFs) in the early universe, it has been very hard to answer this question. However, many theorists have aggressively sought to find an answer and break new ground in modern cosmology. In this subsection, we introduce some plausible origins of PMFs in the early universe (see Ryu et al. 2012; Widrow et al. 2012 for details).

It is difficult for the inflation models to provide electromagnetic quantum fluctuation, because the electromagnetic field is invariant in the conformal transformation. Therefore, the generation and evolution of PMFs in the inflation era has been discussed using an additional scalar field; the dilaton (Bamba & Yokoyama 2004) and the Higgs (Prokopec & Puchwein 2004), and the field of gravity (Turner & Widrow 1988). These theories can explain the generations of coherent magnetic fields on cosmological scales. At present, however, these fields have too-small amplitudes of 10^{-15}–10^{-25} G.

When a magnetic field generated during the epoch of the inflation has a stronger energy density than the background inflaton energy density, this magnetic field destroys the cosmological homogeneity and isotropy. This is called the back-reaction problem of the PMF generation. Several Japanese researchers have contributed to building the generation theory of the PMF with consideration of the back-reaction problem (Kanno et al. 2009; Suyama & Yokoyama 2012; Fujita & Yokoyama 2014). Ferreira, Jain, and Sloth (2014) indicated that the simplest gauge invariant models $f^2(\phi)F_{\mu\nu}F^{\mu\nu}$ suppress the generation of a PMF to $B \lesssim 10^{-30}$ G at Mpc. Such suppression can be avoided in PMFs generated by cosmic reheating (Kobayashi 2014) and/or phase transitions (Hogan 1983; Vachaspati 1991).

The quantum chromodynamics and electroweak phase transition models (Kahniashvili et al. 2013) can generate PMFs with an amplitude of 10^{-9} G on a coherence length of 50 kpc, and an amplitude of 10^{-10} G on 0.3 kpc, respectively, all at present ($z = 0$). PMFs generated in the epoch of the inflation tend to affect the cosmological physical processes on larger scales, while those generated by phase transitions tend to affect those on smaller scales.

Finally, in the cosmological recombination era ($z \sim 1100$), there is also a significant generation process of magnetic fields (Takahashi et al. 2005; Ichiki et al. 2006). The external force from CMB photons through Thomson scattering is exerted more preferentially on electrons than protons, which would separate electrons and protons in the primordial plasma. On a cosmological timescale, such external force is balanced with the force from the electric fields induced by the charge separation, and these electric field generate magnetic fields through Maxwell equations.

9.2 Impact of primordial fields on the present universe

9.2.1 Big Bang nucleosynthesis

The abundances of the light elements in the universe are well reproduced by the standard BBN theory, except the ^{7}Li abundance which is inconsistent with the observed one on the surface of metal-poor halo stars. Many researchers have been exploring the solutions for this "^{7}Li problem." Previous studies have proposed three effective solutions to solve it, and one of them focuses on the PMF.

The first is to consider the photon cooling. In this model, the predicted baryon-to-photon ratio ($\eta_{\rm BBN}$) is smaller by a factor of $(2/3)^{3/4}$ before the end of the BBN epoch. In this case, $\eta_{\rm BBN} = (4.57 \pm 0.10) \times 10^{-10}$, and the D, ^{3}He, and ^{6}Li abundances are raised, while ^{4}He and ^{7}Li abundances are suppressed. The ^{7}Li abundance predicted by the photon cooling model is consistent with the observed results, except that the D abundance is overproduced (Erken et al. 2012).

The second is to consider the decay of a long-lived X particle. Non-thermal photons are produced by the radiative decay of a long-lived massive X particle after the end of the BBN (Lindley 1979; Ellis et al. 1985; Kawasaki & Moroi 1995a, 1995b). The nuclei of ^{7}Be and D produced in BBN are disintegrated by the non-thermal photons (Lindley 1979; Ellis et al. 1985; Cyburt et al. 2003; Kawasaki et al. 2005; Jedamzik 2006; Kusakabe et al. 2006). Considering the photon cooling and the decay

particle model simultaneously (a previous hybrid model), we may solve the problem of deuterium overproduction.

The third is to consider the PMF. The cosmic expansion becomes faster if we consider the ensemble energy density of the PMF, ρ_B. Also, the weak reactions can freeze out earlier. Consequently, the neutron abundance increases. Since the faster cosmic expansion leads to a shorter time interval from the freeze-out to ^{4}He production, more neutrons can survive from the β-decay before the epoch of ^{4}He production. Therefore, the energy density of the PMF increases the ^{4}He abundance significantly. On the other hand, the D and ^{3}He abundances rise moderately, the ^{6}Li abundance rises slightly, and the ^{7}Li abundance is suppressed (Kawasaki & Kusakabe 2012; Yamazaki & Kusakabe 2012; Yamazaki et al. 2014).

Yamazaki et al. (2014) extended the standard BBN to a new hybrid BBN by taking into account the above three possible effects simultaneously. They used the maximum likelihood analysis to constrain the energy density of the PMF by the observed abundances of light elements up to Li. They found that the BBN model with a PMF gives a better likelihood than that without a PMF, and the best-fitting PMF energy density is given by

$$\rho_B(a) = \frac{\rho_B(a_0)}{a^4} = 6.82 \times 10^{-52} a^{-4}\,\mathrm{GeV}^4, \tag{57}$$

where a is the scale factor and $a_0 = 1$ is the present value. This best-fitting value corresponds to $B(a) = 1.89 a^{-2}\mu$G, where $\rho_B = B^2/8\pi = 1.9084 \times 10^{-40}\ (B/1\ \mathrm{G})\,\mathrm{GeV}^4$. An upper bound on the PMF energy density is also obtained, $\rho_B(a) < 1.45 \times 10^{-51} a^{-4}\,\mathrm{GeV}^4$ (95% C.L.). This upper bound corresponds to $B(a) < 3.05 a^{-2}\,\mu$G (95 % C.L.).

9.2.2 CMB and MSP

The CMB temperature fluctuations and polarization anisotropies provide information on the cosmological parameters, e.g., the baryon and the dark matter abundances, the age of the universe, the epoch of the reionization, and the neutrino mass (Lewis et al. 2000; Lewis & Bridle 2002; Hinshaw et al. 2013; Planck Collaboration 2016). The MPS shows the spatial distribution of the matter density fluctuation in the universe. The time evolutions of MPS can be reproduced by theoretical estimations (Lewis et al. 2000) and observing the distributions of galaxies and clusters of galaxies with respect to each redshift z (Cole et al. 2005; Tegmark et al. 2006). Since we can also extract important information on the evolutions of the large-scale structures and the cosmological parameters by the MPS (Lewis & Bridle 2002; Cole et al. 2005; Tegmark et al. 2006), we can obtain the constrained cosmological parameters with a better likelihood using the CMB and MPS observation data simultaneously.

There are two main PMF effects in the cosmological linear perturbation theory. The first is the perturbative PMF effects (Yamazaki et al. 2005, 2006a, 2010, 2012). Those effects cause the other fluctuations of the CMB and the MPS. The strengths of the perturbative PMF at each wavenumber k are given by the power-law spectrum $\langle B(k)B^*(k)\rangle \propto k^{n_B}$, where n_B is the power spectrum index of the PMF. We assume that the local energy densities of the perturbative PMF are comparable to or less than the energy densities of the perturbative CMB photons at each k. The perturbative PMFs produce other perturbations of the ionized baryons by the Lorentz force before the recombination era. Since those baryons affect the CMB photons through Thomson scattering, and they also affect the dark matter through the gravity, the perturbative PMF can also produce the density fluctuations of the CMB photons and the dark matter indirectly (Yamazaki et al. 2005, 2006a, 2010). Furthermore, the perturbative PMF makes the polarization isotropies of the CMB (Yamazaki et al. 2006a, 2008). The perturbative PMF effects tend to contribute to the CMB and the MPS in smaller-scale regions, e.g., wavenumber $k > 0.1\,h\,\mathrm{Mpc}^{-1}$, where h is the Hubble parameter (Yamazaki et al. 2006b, 2008).

The second is the background PMF effects (e.g., Yamazaki et al. 2011). The PMF given by the power-law spectrum has background (ensemble) energy density ρ_B as follows (Yamazaki 2014, 2016),

$$\rho_B \sim \frac{1}{8\pi a^4}\frac{B_\lambda^2}{\Gamma\left[(n_B+5)/2\right]}(\lambda k_{\max})^{n_B+3}, \tag{58}$$

where $B_\lambda = |\mathbf{B}_\lambda|$ is the comoving field strength found by smoothing over Gaussian sphere of radius $\lambda = 1\,\mathrm{Mpc}$ ($k_\lambda = 2\pi/\lambda$), $\Gamma(x)$ is the gamma function, $k_{\max}$ is the cut-off scale defined by the PMF damping (Jedamzik et al. 1998; Subramanian & Barrow 1998; Mack et al. 2002). The background PMF effects due to ρ_B change the features of the CMB and the MPS through the Meszaros (Meszaros 1974) and the potential damping (Ma & Bertschinger 1995) effects. The CMB temperature fluctuations are suppressed around the first peak and their peaks are shifted to larger scales (smaller multipoles) by the background PMF (Yamazaki 2014). The background PMF effects also suppress the amplitudes of the MPS in $k > 0.02\,\mathrm{Mpc}^{-1}$ (Yamazaki 2016).

The CMB polarization anisotropies have an odd parity (curl) component. This is called the "B" mode. The B mode of the CMB polarizations provide important information on the background gravitational wave, the inflation theory, and the reionizations. The B mode is affected by the weak lensing effects, which can be derived by the MPS. Since the PMF affects the MPS as mentioned above (Yamazaki 2016), the PMF affects the B mode, as seen in figure 14.

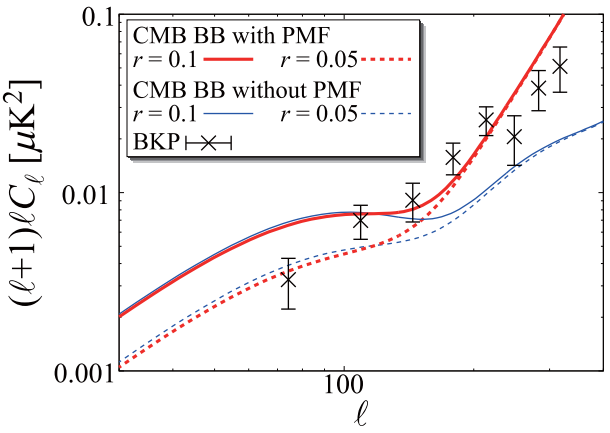

Fig. 14. Total effects of the PMF on the CMB BB mode. In this figure, the power spectral index, n_B, and the amplitude of the PMF, B_λ, are (n_B, B_λ) = (0.0, 3.0 nG). The bold solid and dotted curves are the theoretical results with PMF on $r = 0.1$ and 0.05, respectively. The thin solid and dotted curves are the theoretical results without the PMF on $r = 0.1$ and 0.05, respectively. The points with the error bars are analysis results from (BICEP2/Keck & Planck Collaborations 2015). (Color online)

9.3 Structure formation and magnetic fields

9.3.1 Epoch of reionization

After recombination, the gas in the universe had become almost neutral with a degree of ionization $x_e \sim 10^{-4}$. As the structure of the universe evolved through gravitational instability, the gas was ionized first by luminous sources, and the electromagnetic action has become effective again. Possible mechanisms for generating magnetic fields during this epoch have been intensively discussed in the literature. These mechanisms are mainly based on two effects.

One is the anisotropic radiation pressure preferentially exerted on free electrons, which would separate positive and negative charges in the IGM. Anisotropic UV radiation fields are naturally realized in this epoch because neutral hydrogen clouds can absorb UV photons effectively, and therefore the magnetic fields are mostly generated behind the clouds (Langer et al. 2005; Ando et al. 2010). On cosmological timescales, the force of pressure gradient caused by UV photons from first-generation stars as well as CRs from supernovae explosions is balanced with the force of electric fields induced by the charge separation, and so the rotation component of those fields induces magnetic fields (Langer et al. 2003, 2005; Chuzhoy 2004; Ando et al. 2010; Miniati & Bell 2011; Shiromoto et al. 2014; Durrive & Langer 2015). The field amplitude through these mechanisms in the IGM ranges from $\sim 10^{-19}$ G to $\sim 10^{-16}$ G, depending on the model parameters. Stronger fields can be locally expected near luminous sources. Based on radiation hydrodynamics simulations of proto-first-star formation, Durrive and Langer (2015) found that $\sim 10^{-9}$ G fields are generated on the surface of the accretion disk around a proto-first-star. These fields would be blown out from the disk and diffuse into the low-density regions, which may affect the next generation star-formation activities (Durrive & Langer 2015).

The other is based on the Biermann battery effect (Gnedin et al. 2000; Doi & Susa 2011; Shiromoto et al. 2014). The effect is expressed as $\dot{\mathbf{B}} \sim (ck_B/en_e)\nabla T_e \times \nabla n_e$, and therefore it takes place under non-adiabatic conditions where directions of temperature and density gradients are different from each other. Typical sites are ionization fronts in the vicinities of protogalaxies and those propagating through the high-density filaments of the cosmological large-scale structure. Gnedin, Ferrara, and Zweibel (2000) estimated the amplitude of magnetic fields through the Biermann battery effect at the epoch of reionization by post-processing their reionization simulation data. They found that magnetic fields can be as large as 10^{-19} G by $z \sim 5$, and those fields are highly ordered on Mpc scales. The field amplitude should be considered as a lower limit because of a finite spatial resolution of the simulation. These fields may be responsible for the magnetic fields in the IGM, the existence of which has been suggested from the recent gamma-ray observations (Neronov & Vovk 2010).

9.3.2 Shocks and magnetic turbulence

Cosmological shock waves in the structure formation can generate seed magnetic fields by the Biermann battery (Ryu et al. 1998), the Wibel instability (Okabe & Hattori 2003), and plasma instability (Fujita & Kato 2005). Gregori et al. (2012) carried out plasma experiments for shock waves in galaxy clusters and claimed that the Biermann buttery effect can be an influential candidate of the seed magnetic fields. Seed magnetic fields of any origin could be further amplified through compression and eddy cascading (turbulence dynamo) in the cosmic web (e.g., Ryu et al. 2008; Dubois & Teyssier 2008; see also Vazza et al. 2017). Therefore, the cosmic web is thought to be filled with the IGMF (intergalactic magnetic field).

In galaxy clusters, it is well-studied that the IGMF attracts CRs and causes synchrotron radio emission (see section 8). The IGMF, particularly magnetic turbulence, is important in understanding the thermal balance in cool-core clusters (e.g., Fujita & Ohira 2012, 2013) and structures of merging clusters (e.g., Asai et al. 2005; Takizawa 2008).

Meanwhile, the IGMF in filaments of galaxies is not well known. A conservative range of the IGMF strength in filaments is $O(1\text{–}100)$ nG (Ryu et al. 2008). The amplitude, growth timescale, and characteristic scale of the IGMF was studied by means of MHD turbulence simulations (Cho & Ryu 2009). It was suggested that turbulence is in the linear-growth and the saturation stages in filaments and clusters,

respectively, based on the expected eddy turnover time. The integral scales, which is one of the possible quantifications of the coherence length of magnetic fields, are 1/15 and 1/5 of the energy injection scales in filaments and galaxy clusters. Supposing an electron density of $10^{-5}\,\mathrm{cm}^{-3}$, an rms magnetic field strength of 300 nG, an integral scale of 300 kpc, and the depth of a filament set as 5 Mpc, the standard deviation of *RM* through the filament is estimated to be $\sim$1.5 rad m^{-2}.

Very recently, Hitomi observed the core region of the Perseus galaxy cluster (Hitomi Collaboration 2016) and discovered the turbulence velocity of $\sim$150 km s^{-1} at $\sim$10 kpc scales (the inertial range of turbulence expected in galaxy clusters). Such a velocity seems to be smaller than that expected (e.g., Heinz et al. 2010), implying a relatively low Reynolds number ($Re \sim 100$–200), i.e., a high viscosity, of the IGM (Reynolds et al. 2005; see also Ruszkowski et al. 2007). Examining such key turbulence parameters (see subsection 1.4) is crucially important to understand the significance of turbulence dynamo in the large-scale structure formation.

9.3.3 Galaxies

Physical processes in the early universe are not the only possibilities of generating the IGMF; large-scale outflows from magnetized galaxies at late times could be an alternative (Rees 1987; Durrer & Neronov 2013). Magnetic fields in galaxies can be transported outside them in some ways. For instance, Ensslin et al. (1997) had an analytic discussion whether radio galaxies in clusters can inject magnetic fields to the ICM, and found that fields can be transported to the ICM by jets within a radius of 1 Mpc. Furlanetto and Loeb (2001) studied the possibility that the quasar outflow pollutes the IGM with a magnetic field. They found that a magnetized quasar bubble can further expand after the quasar activity has ceased due to overpressure, and that about 5%–20% of the IGM volume is filled with a magnetic field by $z \sim 3$, the strength of which is at the level of 10% of the thermal energy density of the IGM with temperature 10^4 K.

Kronberg et al. (2001) analytically demonstrated how magnetic fields ejected by AGN contribute to the IGM for the two cases: cluster-embedded AGN and those outside of clusters. They suggested that 10–100 of the former type of AGN can transport sufficient magnetic energy to the level observationally found ($\sim 10^{61}$ erg) beyond the inner cores of clusters, and that the expansion of lobes from the latter type of AGN can magnetize a significant fraction of the IGM. Xu et al. (2009, 2012) performed cosmological MHD simulations and showed that the magnetic fields ejected by AGN can be transported throughout clusters. The radial profiles of the synthetic $|RM|$ and σ_{RM} made from the simulation agree with observations.

Magnetic fields spread into the IGM by supernovae-driven galactic winds might be another possibility (Kronberg et al. 1999). Völk and Atoyan (2000) analytically estimated that typical field strength in clusters can be $\geq 10^{-7}$ G by magnetized galactic winds. Donnert et al. (2009) extended a semi-analytic study by Bertone, Vogt, and Enßlin (2006) and performed cosmological MHD simulations to study the contribution of galactic outflows to the ICM magnetic fields. They showed that the galactic outflows can explain the properties of the μG-scale fields observed in galaxy clusters.

The magnetization of the void by galaxies in the void has also been studied. Bertone, Vogt, and Enßlin (2006) evaluated the effect of galactic winds on the IGM in voids and found that most regions affected by the winds have magnetic fields between 10^{-12} to 10^{-8} G. Beck et al. (2013b) analytically discussed the transport of magnetic energy by CRs from galaxies and contributions of strong AGN bordering the voids. They argued that the lower limit on the void magnetic field claimed from observational results (e.g., Neronov & Vovk 2010; Takahashi et al. 2012), $\gtrsim 10^{-15}$ G, can be recovered by the galaxies and AGN.

9.4 Can we observe the cosmic web?

9.4.1 RM grids

The IGMF strength of $B \sim$ 1–100 nG is expected from cosmological simulations (e.g., Ryu et al. 2008). Such a small field gives the rms value of *RM* of only $\sim$1 rad m^{-2} for a single filament (Akahori & Ryu 2010). The smallness is the main reason for the lack of IGMF detection. However, Akahori and Ryu (2011) demonstrated that the *RM* due to the IGMF for several filaments up to $z \sim$ a few becomes several rad m^{-2}, which is comparable to *RM*s associated with the Milky Way (section 5), DINGs (section 6), and AGN (section 7).

The *RM* grid approach can be a powerful tool to prove such a small fields statistically (Oppermann et al. 2015; Johnston-Hollitt et al. 2015). Akahori, Gaensler, and Ryu (2014a) developed a method to estimate the statistics of *RM*s due to the IGMF from observed *RM*s. The simulation predicts that the IGMF in filaments would be distinguished from the GMF by $S_{2,RM}$ (see sub-subsection 5.2.2), and such a study is possible using RM grids in the SKA era. Similarly, the Bayesian approach allows us to detect $\sim$ nG magnetic fields using the SKA (Vacca et al. 2016).

Linearly-polarized fast radio bursts (FRBs) would be a new probe of the IGMF in filaments. Akahori, Ryu, and Gaensler (2016) pointed out that the classical estimator of

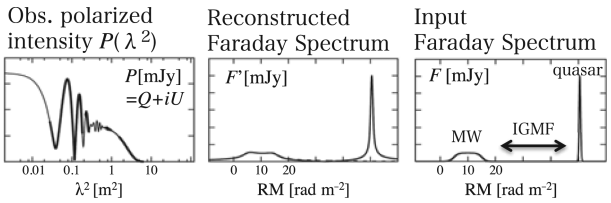

Fig. 15. Exploring the IGMF by means of Faraday tomography. (Left) Mock polarized intensity spectrum. (Middle) Reconstructed Faraday spectrum with the SKA2. (Right) Input Faraday spectrum. See Akahori et al. (2014b) for details.

the mean magnetic field strength, $B_{||}^{\dagger} \sim RM/DM$, is incorrect in the cosmological context. They suggested the use of $B_{||}^{\ddagger} \sim \langle 1+z \rangle B_{||}^{\dagger}/f_{DM}$, where $\langle 1+z \rangle$ is the redshift of intervening gas weighted by the gas density in filaments, f_{DM} is the fraction of total DM due to the gas in filaments, and the redshift of the FRB is not required to be known. Recently, Ravi et al. (2016) reported from FRB 150807 analysis that the net magnetization of the cosmic web along the LOS is constrained to be $<21\,\mu$G with their estimation of the negligible magnetization of plasma around the source.

9.4.2 Faraday tomography

There are few attempts to explore the possibility of proving the IGMF in the cosmic web with direct usage of the Faraday tomography. Akahori et al. (2014b) first investigated the potential of the RM synthesis to find the IGMF. They developed a strategy where two polarized sources along a LOS were observed and tried to find the IGMF as a "gap" between the two sources in Faraday depth space (figure 15). They found that the gap is detectable with the SKA if the RM due to the IGMF is $\sim$10 rad m^{-2}.

Ideguchi et al. (2014a) followed the strategy of Akahori et al. (2014b) and studied the potential of the QU-fitting technique to find the IGMF. They found that an IGMF with RM of $\sim$3 rad m^{-2} can be detected with the combination of the radio telescopes, ASKAP, LOFAR, and GMRT. The strategy they adopted may be a rare situation, but we may find LOSs with such situations in the SKA era, when we would obtain a large amount of polarized sources, i.e., a few hundred of them per square degree (Johnston-Hollitt et al. 2015). Since robust detection of real components is essential to find the gap, it is also important to develop reliable Faraday tomography codes (e.g., Miyashita et al. 2016).

9.4.3 Cross correlation

There are few works studying the cross-correlation (CC) between synchrotron emission and large-scale structure (LSS). For instance, Brown, Farnsworth, and Rudnick (2010) performed a CC between synchrotron emission observed with the 1.4 GHz Bonn survey with galaxies as a tracer of the LSS for two redshifts slices ($0.03 < z < 0.04$ and $0.06 < z < 0.07$) using a $34^\circ \times 34^\circ$ area of the Two-Micron All-Sky-Survey (2MASS). Also, very recently, Vernstrom et al. (2017) explored a CC using Murchison Widefield Array (MWA) for synchrotron emission and 2MASS and the Widefield InfraRed Explorer for tracers of the LSS using a $21.^\circ76 \times 21.^\circ76$ area. Both works provided a null correlation.

The assumption of perfect correspondence between the distribution of galaxies and IGM synchrotron radiation is, however, over-simplification, as mentioned in those two papers. Indeed, it has been reported that the synchrotron radiation associates with shock in LSS, not with matter structure, basically because electrons emitting synchrotron radiation are accelerated at shocks via DSA process (e.g., Hong et al. 2015). On the other hand, since it is known that RM associates with matter structure in LSS (Akahori & Ryu 2010, 2011), a CC between RM and LSS can be promising, as long as the removal of the galactic foreground can be achieved (Stasyszyn et al. 2010).

10 Summary

The origin and evolution of cosmic magnetism is one of the fundamental questions in modern astrophysics. MHD simulations of global and turbulent magnetic fields have advanced our understanding of the physics underlying cosmic magnetism. Centimeter and meter radio observations of synchrotron emission and Faraday rotation measurements are some of only a few established methods which allow us to measure magnetic fields in both galactic and extragalactic objects. In this review paper, we have reviewed the progress of the study of cosmic magnetism mainly driven by centimeter and meter radio observations. We have highlighted magnetic fields in the ISM, the Milky Way Galaxy, external galaxies, AGN and jets, clusters of galaxies, and the cosmic web.

There are three key points that should be considered in future studies of cosmic magnetism by centimeter and meter radio observations. The first one is to understand total radio intensity more precisely. The intensity gives basic information on the magnetic field strength. Moreover, its spectrum provides information on CR energy distribution and will give a clue towards understanding particle acceleration mechanisms. The second one is to understand depolarization. Depolarization is tightly related to magnetic field structure, thus it will give a hint of the nature of both the regular and random magnetic fields. The third one is to understand Faraday tomography. Faraday tomography has the potential to deproject the LOS structure of magnetized plasma, so that it will give new discoveries of unknowns such as the IGMF. A successful observation

Table 1. Expected density of *RM* grids at 1.4 GHz with the SKA.

Polarized intensity	Counts*	Reference
4 μJy	~230–450 deg^2	Johnston-Hollitt et al. (2015)
0.75 μJy	~5000 deg^2	Taylor et al. (2015)

*The number of extragalactic polarized sources.

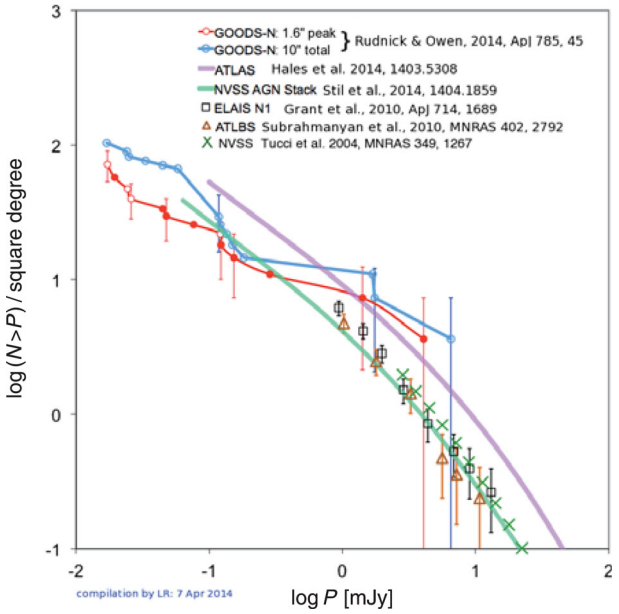

Fig. 16. Population of polarized sources observed at 1.4 GHz (Rudnick & Owen 2014; Taylor et al. 2015). The red and blue, purple, and green lines are based on the deep observations of the ~0.2 deg^2 VLA GOODS-N field (Rudnick & Owen 2014), the ~6 deg^2 ATCA ATLAS field (Hales et al. 2014), and the all-sky VLA NVSS survey (Stil et al. 2014), respectively. (Color online)

for confronting the above three subjects would be ultra-wideband polarimetric observation. The UHF (300 MHz–3 GHz) band would be promising, based on the *RM* range that we are interested in and corresponding energy range of CR electrons.

One of the advantages of centimeter and meter radio observations for the study of cosmic magnetism is a survey speed. All-sky polarization surveys can provide "RM grid" maps, which are useful for studying spatial structures of magnetic fields. Increasing the number of sources, i.e., denser *RM* grids, can reveal smaller spatial structures. Moreover, it can provide more observation points in redshift space, allowing us to study the population of AGN and the cosmic evolution of magnetic fields. Table 1 lists the expected density of *RM* grids to be obtained with the SKA1. These estimations are basically derived from figure 16, which summarizes plots of observed source populations (mostly FR galaxies and quasars) at 1.4 GHz. Because the measured populations have a large scatter, there is still a factor of four uncertainty in the estimation of *RM* grids (Govoni et al. 2014); the population below 10 μJy is not well known. Faint components such as star-forming galaxies, ULIRGs, merging galaxies, and quiet spiral galaxies, would be more important in the low-luminosity regime (Taylor et al. 2015). Deep pilot observations (figure 16) are useful in foreseeing the density of *RM* grids in the SKA era.

In conclusion, the magnetic field is fundamental physics and ubiquitous in the universe. It has been revealed that the magnetic field plays key roles in the formation and evolution of the universe. The importance of understanding cosmic magnetism will increase more and more. Future centimeter and meter radio observations will allow us to adopt new breakthrough techniques, and will be essential in elucidating the origin and nature of cosmic magnetism in coming decades.

Acknowledgments

The authors would like to thank Japan SKA Consortium Cosmic Magnetism Science Working Group members for their contributions to magnetism sciences and their useful comments, suggestions, and encouragements. This article is in part motivated by the archival white book "*Resolving 4-D Nature of Magnetism with Depolarization and Faraday Tomography*" (arXiv:1603.01974) written by the members. The authors are also grateful very much to International SKA Cosmic Magnetism Science Working Group members for providing us opportunities of open discussion and cooperation. This work was supported in part by JSPS KAKENHI Grants: 26400218 (MT), 15H03639 (TA), 15K05080 (YF), 15H05896 (KT), 15K17614 (TA), 16H05999 (KT), 16K20927 (DGY), 17H01110 (TA, KI, KT), and by the National Research Foundation of Korea through grant: 2007-0093860 (SI).

References

Abramowicz, M. A., Chen, X., Kato, S., Lasota, J.-P., & Regev, O. 1995, ApJ, 438, L37
Ajello, M., et al. 2009, ApJ, 690, 367
Ajello, M., Rebusco, P., Cappelluti, N., Reimer, O., Böhringer, H., La Parola, V., & Cusumano, G. 2010, ApJ, 725, 1688
Akahori, T., et al. 2016, arXiv:1611.06647
Akahori, T., Gaensler, B. M., & Ryu, D. 2014a, ApJ, 790, 123
Akahori, T., Kumazaki, K., Takahashi, K., & Ryu, D. 2014b, PASJ, 66, 65
Akahori, T., & Ryu, D. 2010, ApJ, 723, 476
Akahori, T., & Ryu, D. 2011, ApJ, 738, 134
Akahori, T., Ryu, D., & Gaensler, B. M. 2016, ApJ, 824, 105
Akahori, T., Ryu, D., Kim, J., & Gaensler, B. M., 2013, ApJ, 767, 150
Akamatsu, H., & Kawahara, H. 2013, PASJ, 65, 16
Akamatsu, H., Takizawa, M., Nakazawa, K., Fukazawa, Y., Ishisaki, Y., & Ohashi, T. 2012, PASJ, 64, 67
Altenhoff, W. J., Downes, D., Pauls, D., & Schraml, J. 1978, A&AS, 35, 23

Alves, F. O., Franco, G. A. P., & Girart, J. M. 2008, A&A, 486, L13
Anantharamaiah, K. R., Pedlar, A., Ekers, R. D., & Goss, W. M. 1991, MNRAS, 249, 262
Ando, M., Doi, K., & Susa, H. 2010, ApJ, 716, 1566
Antonucci, R. R. J., & Miller, J. S. 1985, ApJ, 297, 621
Arshakian, T. G., & Beck, R. 2011, MNRAS, 418, 2336
Arshakian, T. G., Beck, R., Krause, M., & Sokoloff, D. 2009, A&A, 494, 21
Asada, K., Inoue, M., Uchida, Y., Kameno, S., Fujisawa, K., Iguchi, S., & Mutoh, M. 2002, PASJ, 54, L39
Asada, K., Nakamura, M., Doi, A., Nagai, H., & Inoue, M. 2014, ApJ, 781, L2
Asai, N., Fukuda, N., & Matsumoto, R. 2005, Adv. Space Res., 36, 636
Asano, K., & Takahara, F. 2009, ApJ, 690, L81
Ascasibar, Y., & Markevitch, M. 2006, ApJ, 650, 102
Balbus, S. A., & Hawley, J. F. 1991, ApJ, 376, 214
Bamba, A., Yamazaki, R., Ueno, M., & Koyama, K. 2003, ApJ, 589, 827
Bamba, K., & Yokoyama, J. 2004, Phys. Rev. D, 69, 043507
Bandiera, R., & Petruk, O. 2016, MNRAS, 459, 178
Barniol Duran, R., Whitehead, J. F., & Giannios, D. 2016, MNRAS, 462, 31
Basu, S., & Ciolek, G. E. 2004, ApJ, 607, L39
Basu, S., & Mouschovias, T. Ch., 1994, ApJ, 432, 720
Basu, A., Roy, S., & Mitra, D. 2012, ApJ, 756, 141
Beck, A. M., Dolag, K., Lesch, H., & Kronberg, P. P. 2013a, MNRAS, 435, 3575
Beck, A. M., Hanasz, M., Lesch, H., Remus, R.-S., & Stasyszyn, F. A. 2013b, MNRAS, 429, L60
Beck, M. C., Beck, A. M., Beck, R., Dolag, K., Strong, A. W., & Nielaba, P. 2016, JCAP, 5, 56
Beck, R. 2001, Space Sci. Rev., 99, 243
Beck, R. 2007, A&A, 470, 539
Beck, R. 2015, A&A, 578, A93
Beck, R., Fletcher, A., Shukurov, A., Snodin, A., Sokoloff, D. D., Ehle, M., Moss, D., & Shoutenkov, V. 2005, A&A, 444, 739
Beck, R., Frick, P., Stepanov, R., & Sokoloff, D. 2012, A&A, 543, 113
Beck, R., Loiseau, N., Hummel, E., Berkhuijsen, E. M., Grave, R., & Wielebinski, R. 1989, A&A, 222, 58
Beck, R., Shoutenkov, V., Ehle, M., Harnett, J. I., Haynes, R. F., Shukurov, A., Sokoloff, D. D., & Thierbach, M. 2002, A&A, 391, 83
Bell, A. R. 2004, MNRAS, 353, 550
Bell, M. R., Junklewitz, H., & Enßlin, T. A. 2011, A&A, 535, A85
Bennett, A. S. 1962, Mem. R. Astron. Soc., 68, 163
Beresnyak, A., Xu, H., Li, H., & Schlickeiser, R. 2013, ApJ, 771, 131
Berkhuijsen, E. M., Mitra, D., & Mueller, P. 2006, AN, 327, 82
Bernet, M. L., Miniati, F., & Lilly, S. J. 2012, ApJ, 761, 144
Bernet, M. L., Miniati, F., & Lilly, S. J. 2013, ApJ, 772, L28
Bernet, M. L., Miniati, F., Lilly, S. J., Kronberg, P. P., & Dessauges-Zavadsky, M. 2008, Nature, 454, 302
Bertone, S., Vogt, C., & Enßlin, T. 2006, MNRAS, 370, 319
BICEP2/Keck & Planck Collaborations 2015, Phys. Res. Lett., 114, 101301
Biermann, L. 1950, Z. Naturforsch., A, 5, 65
Blandford, R., & Eichler, D. 1987, Phys. Rep., 154, 1
Blasi, P. 2013, A&AR, 21, 70
Blasi, P., & Colafrancesco, S. 1999, Astroparticle Phys., 12, 169
Bogdanov, S. V., Archibald, A. M., Hessels, J. W. T., Kaspi, V. M., Lorimer, D., McLaughlin, M. A., Ransom, S. M., & Stairs, I. H. 2011, ApJ, 742, 97
Böhringer, H., & Morfill, G. E. 1988, ApJ, 330, 609
Bolton, J. G., & Stanley, G. J. 1948, Australian J. Sci. Res. A Phys. Sci., 1, 58
Bonafede, A., Feretti, L., Murgia, M., Govoni, F., Giovannini, G., Dallacasa, D., Dolag, K., & Taylor, G. B. 2010, A&A, 513, A30
Bower, G. C., Falcke, H., Wright, M. C., & Backer, D. C. 2005, ApJ, 618, L29
Brandenburg, A., Donner, K. J., Moss, D., Shukurov, A., Sokoloff, D. D., & Tuominen, I. 1993, A&A, 271, 36
Brandenburg, A., & Nordlund, Å. 2011, Rep. Prog. Phys., 74, 046901
Brandenburg, A., & Stepanov, R. 2014, ApJ, 786, 91
Brentjens, M. A., & de Bruyn, A. G. 2005, A&A, 441, 1217
Brown, J. C., Haverkorn, M., Gaensler, B. M., Taylor, A. R., Bizunok, N. S., McCLure-Griffiths, N. M., Dickey, J. M, & Green, A. J. 2007, ApJ, 663, 258
Brown, J. C., & Taylor, A. R. 2001, ApJ, 563, L31
Brown, S., Farnsworth, D., & Rudnick, L. 2010, MNRAS, 402, 2
Brunetti, G., Blasi, P., Cassano, R., & Gabici, S. 2004, MNRAS, 350, 1174
Brunetti, G., Cassano, R., Dolag, K., & Setti, G. 2009, A&A, 507, 661
Brunetti, G., & Jones, T. W. 2014, Int. J. Mod. Phys. D, 23, 1430007
Brunetti, G., & Lazarian, A. 2007, MNRAS, 378, 245
Brunetti, G., & Lazarian, A. 2011, MNRAS, 410, 127
Brunetti, G., Setti, G., Feretti, L., & Giovannini, G. 2001, MNRAS, 320, 365
Brunetti, G., Venturi, T., Dallacasa, D., Cassano, R., Dolag, K, Giacintucci, S., & Setti, G. 2007, ApJ, 670, L5
Burkhart, B., Lazarian, A., & Gaensler, B. M. 2012, ApJ, 749, 145
Burn, B. J. 1966, MNRAS, 133, 67
Cassano, R. 2010, A&A, 517, A10
Cassano, R., Brunetti, G., & Setti, G. 2006, MNRAS, 369, 1577
Cassano, R., Brunetti, G., & Venturi, T. 2011, J. Astrophys. Astron., 32, 519
Cayatte, V., van Gorkom, J. H., Balkowski, C., & Kotanyi, C. 1990, AJ, 100, 604
Chandrasekhar, S., & Fermi, E. 1953, ApJ, 118, 113
Chapman, N. L., Goldsmith, P. F., Pineda, J. L., Clemens, D. P., Li, D., & Krčo, M. 2011, ApJ, 741, 21
Cho, J., & Ryu, D. 2009, ApJ, 705, L90
Chomiuk, L., et al. 2012, ApJ, 761, 173
Chuzhoy, L. 2004, MNRAS, 350, 761
Chyży, K. T., Beck, R., Kohle, S., Klein, U., & Urbanik, M. 2000, A&A, 355, 128
Chyży, K. T., Knapik, J., Bomans, D. J., Klein, U., Beck, R., Soida, M., & Urbanik, M. 2003, A&A, 405, 513
Clarke, D. A., Burns, J. O., & Norman, M. L. 1992, ApJ, 395, 444
Clegg, A. W., Cordes, J. M., Simonetti, J. H., & Kulkarni, S. R. 1992, ApJ, 386, 143
Cole, S., et al. 2005, MNRAS, 362, 505
Condon, J. J., Anderson, M. L., & Helou, G. 1991, ApJ, 376, 95

Conway, R. G., & Kronberg, P. P. 1969, MNRAS, 142, 11
Cordes, J. M., & Lazio, T. J. W. 2002, arXiv:astro-ph/0207156
Cordes, J. M., & Lazio, T. J. W. 2003, arXiv:astro-ph/0301598
Crutcher, R. M. 1999, ApJ, 520, 706
Crutcher, R. M. 2012, ARA&A, 50, 29
Cyburt, R. H., Ellis, J. R., Fields, B. D., & Olive, K. A. 2003, Phys. Rev. D, 67, 103521
Das, K., Roy, A. L., Keller, R., & Tuccari, G. 2010, A&A, 509, A23
de Jager, O. C., & Djannati-Ataï, A. 2009, in Neutron Stars and Pulsars, ed. W. Becker (Berlin: Springer), 451
Dennison, B. 1980, ApJ, 239, L93
Diamond, P. H., Garbet, X., Ghendrih, P., & Sarazin, Y. 2010, Relaxation Dynamics in Laboratory and Astrophysical Plasmas: Biennial Reviews of the Theory of Magnetized Plasmas, Vol. 1 (Singapore: World Scientific Publishing Co., Pte. Ltd.), ch. 4
Doi, K., & Susa, H. 2011, ApJ, 741, 93
Dolag, K., Bykov, A. M., & Diaferio, A. 2008, Space Sci. Rev., 134, 311
Dolag, K., & Stasyszyn, F. 2009, MNRAS, 398, 1678
Donnert, J., Dolag, K., Lesch, H., & Müller, E., 2009, MNRAS, 392, 1008
Drzazga, R. T., Chyży, K. T., Heald, G. H., Elstner, D., & Gallagher, J. S. 2016, A&A, 589, A12
Dubois, Y., & Teyssier, R., 2008, A&A, 482, L13
Durrer, R., & Neronov, A. 2013, A&AR, 21, 62
Durrive, J.-B., & Langer, M. 2015, MNRAS, 453, 345
Eatough, R., et al. 2013a, Astronomer's Telegram, 5040
Eatough, R. P., et al. 2013b, Nature, 501, 391
Edge, D. O., Shakeshaft, J. R., McAdam, W. B., Baldwin, J. E., & Archer, S. 1959, Mem. R. Astron. Soc., 68, 37
Ellis, J. R., Nanopoulos, D. V., & Sarkar, S. 1985, Nucl. Phys. B, 259, 175
Enßlin, T., Pfrommer, C., Miniati, F., & Subramanian, K. 2011, A&A, 527, A99
Enßlin, T. A., & Vogt, C. 2003, A&A, 401, 835
Ensslin, T. A., Biermann, P. L., Kronberg, P. P., & Wu, X.-P. 1997, ApJ, 477, 560
Erken, O., Sikivie, P., Tam, H., & Yang, Q. 2012, Phys. Rev. D, 85, 063520
Fanaroff, B. L., & Riley, J. M. 1974, MNRAS, 167, 31p
Farnes, J. S., Gaensler, B. M., & Carretti, E. 2014a, ApJS, 212, 15
Farnes, J. S., O'Sullivan, S. P., Corrigan, M. E., & Gaensler, B. M. 2014b, ApJ, 795, 63
Fatuzzo, M., & Adams, F. C. 2002, ApJ, 570, 210
Felten, J. E. 1996, in ASP Conf. Ser., 88, Clusters, Lensing, and the Future of the Universe, ed. V. Trimble & A. Reisenegger (San Francisco: ASP), 271
Feretti, L., Dallacasa, D., Giovannini, G., & Tagliani, A. 1995, A&A, 302, 680
Feretti, L., Giovannini, G., Govoni, F., & Murgia, M. 2012, A&AR, 20, 54
Ferreira, R. J. Z., Jain, R. K., & Sloth, M. S. 2014, JCAP, 6, 53
Field, G. B., Goldsmith, D. W., & Habing, H. J., 1969, ApJ, 155, L149
Finoguenov, A., Sarazin, C. L., Nakazawa, K., Wik, D. R., & Clarke, T. E. 2010, ApJ, 715, 1143
Fletcher, A., Beck, R., Shukurov, A., Berkhuijsen, E. M., & Horellou, C. 2011, MNRAS, 412, 2396
Franco, G. A. P., & Alves, F. O. 2015, ApJ, 807, 5
Frick, P., Sokoloff, D., Stepanov, R., & Beck, R. 2011, MNRAS, 414, 2540
Fujishita, M., et al. 2009, PASJ, 61, 1039
Fujita, T., & Yokoyama, S. 2014, JCAP, 3, 13
Fujita, Y., & Kato, T. N. 2005, MNRAS, 364, 247
Fujita, Y., Kimura, S., & Ohira, Y. 2013, MNRAS, 432, 1434
Fujita, Y., Kohri, K., Yamazaki, R., & Kino, M. 2007, ApJ, 663, L61
Fujita, Y., Matsumoto, T., & Wada, K. 2004, ApJ, 612, L9
Fujita, Y., & Ohira, Y. 2011, ApJ, 738, 182
Fujita, Y., & Ohira, Y. 2012, ApJ, 746, 53
Fujita, Y., & Ohira, Y. 2013, MNRAS, 428, 599
Fujita, Y., Takizawa, M., & Sarazin, C. L. 2003, ApJ, 584, 190
Fujita, Y., Takizawa, M., Yamazaki, R., Akamatsu, H., & Ohno, H. 2015, ApJ, 815, 116
Fukui, Y., et al. 2006, Science, 314, 106
Fukumura, K., Tombesi, F., Kazanas, D., Shrader, C., Behar, E., & Contopoulos, I. 2016, Astron. Nachr., 337, 454
Furlanetto, S. R., & Loeb, A. 2013, ApJ, 556, 619
Gabuzda, D. C., Knuettel, S., & Reardon, B. 2015, MNRAS, 450, 2441
Gaensler, B. M., et al. 2011, Nature, 478, 214
Gaensler, B. M., et al. 2015, in Proc. Advancing Astrophysics with the Square Kilometre Array, ed. T. L. Bourke et al. (Trieste: SISSA), 103
Gaensler, B. M., Haverkorn, M., Staveley-Smith, L., Dickey, J. M., McClure-Griffiths, N. M., Dickel, J. R., & Wolleben, M. 2005, Science, 307, 1610
Gaensler, B. M., Madsen, G. J., Chatterjee, S., & Mao, S. A. 2008, PASA, 25, 184
Gammie, C. F., McKinney, J. C., & Tóth, G. 2003, ApJ, 589, 444
Gao, X. Y., et al. 2010, A&A, 515, 64
Gardner, F. F., & Whiteoak, J. B. 1966, ARA&A, 4, 245
Gelfand, J., Breton, R., Ng, C.-Y., Hessels, J., Stappers, B., Roberts, M., & Possenti, A. 2015, in Proc. Advancing Astrophysics with the Square Kilometre Array, ed. T. L. Bourke et al. (Trieste: SISSA), 46
Gendelev, L., & Krumholz, M.R. 2012, ApJ, 745, 158
Ghez, A. M., et al. 2008, ApJ, 689, 1044
Giacinti, G., Kachelrieß, M., Semikoz, D. V., & Sigl, G. 2010, JCAP, 8, 36
Giacintucci, S., Markevitch, M., Venturi, T., Clarke, T. E., Cassano, R., & Mazzotta, P. 2014, ApJ, 781, 9
Gillessen, S., Eisenhauer, F., Trippe, S., Alexander, T., Genzel, R., Martins, F., & Ott, T. 2009, ApJ, 692, 1075
Ginzburg, V. L., & Syrovatskii, S. I. 1965, ARA&A, 3, 297
Ginzburg, V. L., & Syrovatskii, S. I. 1969, ARA&A, 7, 375
Girart, J. M., Rao, R., & Marrone, D. P. 2006, Science, 313, 812
Gitti, M., Brunetti, G., & Setti, G. 2002, A&A, 386, 456
Gnedin, N. Y., Ferrara, A., & Zweibel, E. G. 2000, ApJ, 539, 505
Goldreich, P., & Sridhar, S. 1995, ApJ, 438, 763
Goldreich, P., & Sridhar, S. 1997, ApJ, 485, 680
Goodman, A. A., Bastien, P., Menard, F., & Myers, P. C. 1990, ApJ, 359, 363
Govoni, F., et al. 2010, A&A, 522, A105
Govoni, F., et al. 2014, in Square Kilometre Array Organisation Science Working Group Assessment Workshop Summary, no. 6, Cosmic Magnetism (Cheshire: SKA Organisation)
Graeve, R., & Beck, R. 1988, A&A, 192, 66

Gray, A. D., Landecker, T. L., Dewdney, P. E., Taylor, A. R., Willis, A. G., & Normandeau, M. 1999, ApJ, 514, 221
Green, D. A. 2009, Bull. Astron. Soc. India, 42, 47
Greenstein, J. L. 1963, Nature, 197, 1041
Gregori, G., et al. 2012, Nature, 481, 480
Gressel, O., Elstner, D., & Ziegler, U. 2013, A&A, 560, 93
Guidetti, D., Murgia, M., Govoni, F., Parma, P., Gregorini, L., de Ruiter, H. R., Cameron, R. A., & Fanti, R. 2008, A&A, 483, 699
Guo, F., & Oh, S. P. 2008, MNRAS, 384, 251
Hada, K., et al. 2016, ApJ, 817, 131
Hales, C. A., Norris, R. P., Gaensler, B. M., & Middelberg, E. 2014, MNRAS, 440, 3113
Hammond, A. M., Robishaw, T., & Gaensler, B. M. 2012, arXiv:1209.1438
Han, J. L., et al. 2015, in Proc. Advancing Astrophysics with the Square Kilometre Array, ed. T. L. Bourke et al. (Trieste: SISSA), 41
Han, J. L., Ferriere, K., & Manchester, R. N. 2004, ApJ, 610, 820
Han, J. L., Manchester, R. N., Lyne, A. G., Qiao, G. J., & van Straten, W. 2006, ApJ, 642, 868
Han, J. L., & Wielebinski, R. 2002, Chin. J. Astron. Astrophys., 2, 293
Hanasz, M., Wóltański, D., & Kowalik, K. 2009, ApJ, 706, L155
Harvey-Smith, L., Madsen, G. J., & Gaensler, B. M., 2011, ApJ, 736, 83
Haugen, N. E. L., Brandenburg, A., & Dobler, W. 2003, ApJ, 597, L141
Haverkorn, M. 2015, in Magnetic Fields in Diffuse Media, ed. A. Lazarian et al. (Berlin: Springer-Verlag), 483
Haverkorn, M., et al. 2015, in Proc. Advancing Astrophysics with the Square Kilometre Array, ed. T. L. Bourke et al. (Trieste: SISSA), 96
Haverkorn, M., Brown, J. C., Gaensler, B. M., & McClure-Griffiths, N. M. 2008, ApJ, 680, 362
Haverkorn, M., Katgert, P., & de Bruyn, A. G. 2004, A&A, 427, 169
Hawley, J. F., Gammie, C. F., & Balbus, S. A. 1995, ApJ, 440, 742
Hazard, C., Mackey, M. B., & Shimmins, A. J. 1963, Nature, 197, 1037
Heald, G., Braun, R., & Edmonds, R. 2009, A&A, 503, 409
Heesen, V., Krause, M., Beck, R., & Dettmar, R.-J. 2009, A&A, 506, 1123
Heiles, C. 1984, ApJS, 55, 585
Heiles, C., & Chu, Y.-H. 1980, ApJ, 235, L105
Heiles, C., Chu, Y.-H., & Troland, T. H. 1981, ApJ, 247, L77
Heinz, S., Brüggen, M., & Morsony, B. 2010, ApJ, 708, 462
Herron, C. A., Burkhart, B., Lazarian, A., Gaensler, B. M., & McClure-Griffiths, N. M. 2016, ApJ, 822, 13
Hezareh, T., Houde, M., McCoey, C., & Li, H.-b. 2010, ApJ, 720, 603
Hill, A. S., Benjamin, R. A., Kowel, G., Reynolds, R. J., Haffner, L. M., & Lazarian, A. 2008, ApJ, 686, 363
Hinshaw, G., et al. 2013, ApJS. 208, 19
Hitomi Collaboration, 2016, Nature, 535, 117
Hogan, C. J. 1983, Phys. Res. Lett., 51, 1488
Hong, S. E., Kang, H., & Ryu, D. 2015, ApJ, 812, 49
Horiuchi, S., Beacom, J. F., Kochanek, C. S., Prieto, J. L., Stanek, K. Z., & Thompson, T. A. 2011, ApJ, 738, 154
Houde, M., Fletcher, A., Beck, R., Hildebrand, R. H., Vaillancourt, J. E., & Stil, J. M. 2013, ApJ, 766, 49
Iacobelli, M., et al. 2014, A&A, 566, 5
Ichiki, K., Takahashi, K., Ohno, H., Hanayama, H., & Sugiyama, N. 2006, Science, 311, 827
Ideguchi, S., Takahashi, K., Akahori, T., Kumazaki, K., & Ryu, D. 2014a, PASJ, 66, 5
Ideguchi, S., Tashiro, Y., Akahori, T., Takahashi, K., & Ryu, D. 2014b, ApJ, 792, 51
Ideguchi, S., Tashiro, Y., Akahori, T., Takahashi, K., & Ryu, D. 2017, ApJ, 843, 146
Inoue, M., Takahashi, T., Tabara, H., Kato, T., & Tsuboi, M. 1984, PASJ, 36, 633
Inoue, T., & Inutsuka, S. 2016, ApJ, 833, 10
Inoue, T., Yamazaki, R., Inutsuka, S., & Fukui, Y. 2012, ApJ, 744, 71
Iroshnikov, P. S. 1964, Sov. Astron., 7, 566
Itahana, M., Takizawa, M., Akamatsu, H., Ohashi, T., Ishisaki, Y., Kawahara, H., & Van Weeren, R. J. 2015, PASJ, 67, 113
Iwamoto, S., & Takahara, F. 2004, ApJ, 601, 78
Jacob, S., & Pfrommer, C. 2017, MNRAS, 467, 1449
Jaffe, T. R., Leahy, J. P., Banday, A. J., Leach, S. M., Lowe, S. R., & Wilkinson, A. 2010, MNRAS, 401, 1013
Jansson, R., & Farrar, G. R. 2012, ApJ, 757, 14
Jedamzik, K. 2006, Phys. Rev. D, 74, 103509
Jedamzik, K., Katalinić, V., & Olinto, A. V. 1998, Phys. Rev. D, 57, 3264
Johnson, M. D., et al. 2015, Science, 350, 1242
Johnston-Hollitt, M., et al. 2015, in Proc. of Advancing Astrophysics with the Square Kilometre Array, ed. T. L. Bourke et al. (Trieste: SISSA), 92
Jokipii, J. R., & Lerche, I. 1969, ApJ, 157, 1137
Kahn, F. D., & Breitschwedt, D. 1989, MNRAS, 242, 209
Kahniashvili, T., Tevzadze, A. G., Brandenburg, A., & Neronov, A. 2013, Phys. Rev. D, 87, 083007
Kamaya, H., Mineshige, S., Shibata, K., & Matsumoto, R. 1996, ApJ, 458, L25
Kanno, S., Soda, J., & Watanabe, M.-a. 2009, JCAP, 12, 9
Käpylä, P. J., Korpi, M. J., & Brandenburg, A. 2008, A&A, 491, 353
Kawano, N., et al. 2009, PASJ, 61, S377
Kawasaki, M., Kohri, K., & Moroi, T. 2005, Phys. Rev. D, 71, 083502
Kawasaki, M., & Kusakabe, M. 2012, Phys. Rev. D, 86, 063003
Kawasaki, M., & Moroi, T. 1995a, ApJ, 452, 506
Kawasaki, M., & Moroi, T. 1995b, Prog. Theor. Phys., 93, 879
Kawashima, T., Matsumoto, Y., & Matsumoto, R. 2017, PASJ, 69, 43
Kennea, J. A., et al. 2013, ApJ, 770, L24
Keshet, U., & Loeb, A. 2010, ApJ, 722, 737
Kim, K.-T., Kronberg, P. P., Dewdney, P. E., & Landecker, T. L. 1990, ApJ, 355, 29
Kim, W.-T., & Stone, J. M. 2012, ApJ, 751, 124
Kimura, S. S., Murase, K., & Toma, K. 2015, ApJ, 806, 159
Kobayashi, T. 2014, JCAP, 5, 40
Kobayashi, T., Maartens, R., Shiromizu, T., & Takahashi, K. 2007, Phys. Rev. D, 75, 103501
Koide, S., Shibata, K., Kudoh, T., & Meier, D. L. 2002, Science, 295, 1688

Kolmogorov, A. 1941, Doklady Akademiia Nauk SSSR, 30, 301
Kothes, R., Fedotov, K., Foster, T. J., & Uyanıker, B. 2006, A&A, 457, 1081
Koyama, K., Petre, R., Gotthelf, E. V., Hwang, U., Matsuura, M., Ozaki, M., & Holt, S. S. 1995, Nature, 378, 255
Kraichnan, R. H. 1965, Phys. Fluids, 8, 1385
Kronberg, P. P., Bernet, M. L., Miniati, F., Lilly, S. J., Short, M. B., & Higdon, D. M. 2008, ApJ, 676, 70
Kronberg, P. P., Dufton, Q. W., Li, H., & Colgate, S. A. 2001, ApJ, 560, 178
Kronberg, P. P., Lesch, H., & Hopp, U. 1999, ApJ, 511, 56
Kronberg, P. P., & Newton-McGee, K. J. 2011, PASA, 28, 171
Krumholz, M. R., Stone, J. M., & Gardiner, T. A. 2007, ApJ, 671, 518
Kudo, N., et al. 2011, PASJ, 63, 171
Kudoh, T., & Basu, S. 2011, ApJ, 728, 123
Kudoh, T., Basu, S., Ogata, Y., & Yabe, T. 2007, MNRAS, 380, 499
Kudoh, T., Matsumoto, R., & Shibata, K. 1998, ApJ, 508, 186
Kulesza-Żydzik, B., Kulpa-Dybeł, K., Otmianowska-Mazur, K., Kowal, G., & Soida, M. 2009, A&A, 498, L21
Kulesza-Żydzik, B., Kulpa-Dybeł, K., Otmianowska-Mazur, K., Soida, M., & Urbanik, M. 2010, A&A, 522, A61
Kulpa-Dybeł, K., Nowak, N., Otmianowska-Mazur, K., Hanasz, M., Siejkowski, H., & Kulesza-Żydzik, B. 2015, A&A, 575, A93
Kulpa-Dybeł, K., Otmianowska-Mazur, K., Kulesza-Żydzik, B., Hanasz, M., Kowal, G., Wóltański, D., & Kowalik, K. 2011, ApJ, 733, L18
Kumazaki, K., Akahori, T., Ideguchi, S., Kurayama, T., & Takahashi, K. 2014, PASJ, 66, 61
Kusakabe, M., Kajino, T., & Mathews, G. J. 2006, Phys. Rev. D, 74, 023526
Laing, R. A., & Bridle, A. H. 1987, MNRAS, 228, 557
Langer, M., Aghanim, N., & Puget, J.-L. 2005, A&A, 443, 367
Langer, M., Puget, J.-L., & Aghanim, N. 2003, Phys. Rev. D, 67, 043505
LaRosa, T. N., Kassim, N. E., Lazio, T. J. W., & Hyman, S. D. 2000, ApJ, 119, 207
Lawler, J. M., & Dennison, B. 1982, ApJ, 252, 81
Lazarian, A., & Pogosyan, D. 2016, ApJ, 818, 178
Leahy, J. P., Pooley, G. G., & Jagers, W. J. 1986, A&A, 156, 234
Lewis, A., & Bridle, S. 2002, Phys. Rev. D, 66, 103511
Lewis, A., Challinor, A., & Lasenby, A. 2000, ApJ, 538, 473
Li, H.-b., Dowell, C. D., Goodman, A., Hildebrand, R., & Novak, G. 2009, ApJ, 704, 891
Li, H.-b., & Houde, M. 2008, ApJ, 677, 1151
Li, Z.-Y., & Nakamura, F. 2004, ApJ, 609, L83
Lindley, D. 1979, MNRAS, 188, 15p
Ma, C.-P., & Bertschinger, E. 1995, ApJ, 455, 7
Machida, M., et al. 2009, PASJ, 61, 411
Machida, M., Nakamura, K. E., Kudoh, T., Akahori, T., Sofue, Y., & Matsumoto, R. 2013, ApJ, 764, 81
Machida, M. N., Inutsuka, S., & Matsumoto, T. 2008, ApJ, 676, 1088
Mack, A., Kahniashvili, T., & Kosowsky, A. 2002, Phys. Rev. D, 65, 123004
Macquart, J.-P., Bower, G. C., Wright, M. C. H., Backer, D. C., & Falcke, H. 2006, ApJ, 646, L111
Manchester, R. N. 1974, ApJ, 188, 637
Mao, S. A., et al. 2012a, ApJ, 755, 21
Mao, S. A., et al. 2012b, ApJ, 759, 25
Mao, S. A., Gaensler, B. M., Haverkorn, M., Zweibel, E. G., Madsen, G. J., McClure-Griffiths, N. M., Shukurov, A., & Kronberg, P. P. 2010, ApJ, 714, 1170
Mao, S. A., Gaensler, B. M., Stanimirović, S., Haverkorn, M., McClure-Griffiths, N. M., Staveley-Smith, L., & Dickey, J. M. 2008, ApJ, 688, 1029
Marin, F. 2014, MNRAS, 441, 551
Marinacci, F., Vogelsberger, M., Mocz, P., & Pakmor, R. 2015, MNRAS, 453, 3999
Marrone, D. P., Moran, J. M., Zhao, J.-H., & Rao, R. 2007, ApJ, 654, L57
Martí-Vidal, I., Muller, S., Vlemmings, W., Horellou, C., & Aalto, S. 2015, Science, 348, 311
Matsumoto, R., Horiuchi, T., Shibata, K., & Hanawa, T. 1988, PASJ, 40, 171
Matsumoto, Y., et al. 2016, arXiv:1611.01775
Men, H., Ferrière, K., & Han, J. L. 2008, A&A, 486, 819
Mestel, L., & Spitzer, L., Jr. 1956, MNRAS, 116, 503
Meszaros, P. 1974, A&A, 37, 225
Mezger, P. G., Duschl, W. J., & Zylka, R. 1996, A&AR, 7, 289
Migliori, G., Grandi, P., Palumbo, G. G. C., Brunetti, G., & Stanghellini, C. 2007, ApJ, 668, 203
Miniati, F., & Bell, A. R. 2011, ApJ, 729, 73
Miniati, F., Jones, T. W., Kang, H., & Ryu, D. 2001, ApJ, 562, 233
Minter, A. H., & Spangler, S. R. 1996, ApJ, 458, 194
Mitra, D., Wielebinski, R., Kramer, M., & Jessner, A. 2003, A&A, 398, 993
Miyashita, Y., Ideguchi, S., & Takahashi, K. 2016, PASJ, 68, 44
Mizuno, I., et al. 2014, J. Astron. Instrum., 3, 1450010
Mori, K., et al. 2013, ApJ, 770, L23
Morris, M., Davidson, J. A., Werner, M., Dotson, J., Figer, D. F., Hildebrand, R., Novak, G., & Platt, S. 1992, ApJ, 399, L63
Morris, M., & Serabyn, E. 1996, ARA&A, 34, 645
Morris, M., Uchida, K., & Do, T. 2006, Nature, 440, 308
Moss, D., & Shukurov, A. 1993, MNRAS, 279, 229
Mouschovias, T. Ch., & Ciolek, G. E. 1999, in The Origin of Stars and Planetary Systems, ed. C. J. Lada & N. D. Kylafis (Dordrecht: Kluwer), 305
Mouschovias, T. Ch., & Paleologou, E. V. 1980, ApJ, 237, 877
Murgia, M., Govoni, F., Feretti, L., Giovannini, G., Dallacasa, D., Fanti, R., Taylor, G. B., & Dolag, K. 2004, A&A, 424, 429
Murphy, E. J. 2009, ApJ, 706, 482
Nagai, H., et al. 2014, ApJ, 785, 53
Nakamura, F., & Li, Z.-Y. 2007, ApJ, 662, 395
Nakanishi, H., et al. 2006, ApJ, 651, 804
Nakano, T. 1989, MNRAS, 241, 495
Nakano, T., & Nakamura, T. 1978, PASJ, 30, 681
Nakazawa, K., et al. 2009, PASJ, 61, 339
Neronov, A., & Vovk, I. 2010, Science, 328, 73
Netzer, H. 2015, ARA&A, 53, 365
Niklas, S., & Beck, R. 1997, A&A, 320, 54
Nishikori, H., Machida, M., & Matsumoto, R. 2006, ApJ, 641, 862
Nishiyama, S., et al. 2009, ApJ, 690, 1648
Nishiyama, S., et al. 2010, ApJ, 722, L23

Nomura, M., Ohsuga, K., Takahashi, H. R., Wada, K., & Yoshida, T. 2016, PASJ, 68, 16
Nota, T., & Katgert, P. 2010, A&A, 513, A65
Noutsos, A., Johnston, S., Kramer, M., & Karasterigou, A. 2008, MNRAS, 386, 1881
O'Dea, C. P., & Owen, F. N. 1987, ApJ, 316, 95
Ohno, H., & Shibata, S. 1993, MNRAS, 262, 953
Ohno, H., Takizawa, M., & Shibata, S. 2002, ApJ, 577, 658
Okabe, N., Bourdin, H., Mazzotta, P., & Maurogordato, S. 2011, ApJ, 741, 116
Okabe, N., & Hattori, M. 2003, ApJ, 599, 964
Oke, J. B. 1963, Nature, 197, 1040
Oppermann, N., et al. 2015, A&A, 575, A118
Oppermann, N., Junklewitz, H., Robbers, G., & Enßlin, T. A. 2011, A&A, 530, A89
O'Sullivan, S. P., et al. 2012, MNRAS, 421, 3300
Ota, N. 2012, Res. Astron. Astrophys., 12, 973
Ota, N., Nagayoshi, K., Pratt, G. W., Kitayama, T., Oshima, T., & Reiprich, T. H. 2013, A&A, 562, 60
Ozawa, T., et al. 2015, PASJ, 67, 110
Pakmor, R., Marinacci, F., & Springel, V. 2014, ApJ, 783, L20
Pandey, K. L., Choudhury, T. R., Sethi, S. K., & Ferrara, A. 2015, MNRAS, 451, 1692
Parker, E. N. 1971, ApJ, 163, 255
Pavel, M. D. 2011, ApJ, 740, 21
Pavel, M. D., Clemens, D. P., & Pinnick, A. F. 2012, ApJ, 749, 71
Pellegrini, E., et al. 2007, ApJ, 658, 1119
Perley, R. A., Bridle, A. H., & Willis, A. G. 1984, ApJS, 54, 291
Peterson, J. D., & Webber, W. R. 2002, ApJ, 575, 217
Petrosian, V. 2001, ApJ, 557, 560
Pfrommer, C., & Enßlin, T. A. 2004, A&A, 413, 17
Piotrovich, M. Y., Gnedin, Y. N., Silant'ev, N. A., Natsvlishvili, T. M., & Buliga, S. D. 2015, MNRAS, 454, 1157
Planck Collaboration 2016, A&A, 594, A13
Plante, R. L., Lo, K. Y., & Crutcher, R. M. 1995, ApJ, 445, L113
Pounds, K. A., Reeves, J. N., King, A. R., Page, K. L., O'Brien, P. T., & Turner, M. J. L. 2003, MNRAS, 345, 705
Prokopec, T., & Puchwein, E. 2004, Phys. Rev. D, 70, 043004
Prouza, M., & Šmída, R. 2003, A&A, 410, 1
Pshirkov, M. S., Tinyakov, P. G., Kronberg, P. P., & Newton-McGee, K. J. 2011, ApJ, 738, 192
Pudritz, R. E., & Norman, C. A. 1986, ApJ, 301, 571
Purcell, C. R., et al. 2015, ApJ, 804, 22
Rand, R. J., & Kulkarni, S. R. 1989, ApJ, 343, 760
Rao, R., Crutcher, R. M., Plambeck, R. L., & Wright, M. C. H. 1998, ApJ, 502, L75
Ravi, V., et al. 2016, Science, 354, 1249
Reber, G. 1944, ApJ, 100, 279
Rees, M. J. 1987, QJRAS, 28, 197
Reich, W. 2007 in Mapping the Galaxy and Nearby Galaxies, ed. K. Wada & F. Combes (New York: Springer), 63
Rephaeli, Y., Nevalainen, J., Ohashi, T., & Bykov, A. M. 2008, Space Sci. Rev., 134, 71
Ressler, S. M., Katsuda, S., Reynolds, S. P., Long, K. S., Petre, R., Williams, B. J., & Winkler, P. F. 2014, ApJ, 790, 85
Reynolds, C. S., McKernan, B., Fabian, A. C., Stone, J. M., & Vernaleo, J. C. 2005, MNRAS, 357, 242
Reynolds, S. P., Gaensler, B. M., & Bocchino, F. 2012, Space Sci. Rev., 166, 231
Rodríguez, L. F., Gómez, Y., & Tafoya, D. 2012, MNRAS, 420, 279
Rudnick, L., & Owen, F. N. 2014, ApJ, 785, 45
Russell, H. R., McNamara, B. R., Edge, A. C., Hogan, M. T., Main, R. A., & Vantyghem, A. N. 2013, MNRAS, 432, 530
Ruszkowski, M., Enßlin, T. A., Brüggen, M., Heinz, S., & Pfrommer, C. 2007, MNRAS, 378, 662
Rybicki, G. B., & Lightman, A. P. 1979, Radiation Processes in Astrophysics (New York: Wiley-Interscience)
Ryu, D., Kang, H., & Biermann, P. L. 1998, A&A, 335, 19
Ryu, D., Kang, H., Cho, J., & Das, S. 2008, Science, 320, 909
Ryu, D., Schleicher, D. R. G., Treumann, R. A., Tsagas, C. G., & Widrow, L. M. 2012, Space Sci. Rev., 166, 1
Sarazin, C. L. 1999, ApJ, 520, 529
Schekochihin, A. A., Haugen, N. E. L., Brandenburg, A., Cowley, S. C., Maron, J. L., & McWilliams, J. C. 2005, ApJ, 625, L115
Schleicher, D. R. G., Banerjee, R., Sur, S., Arshakian, T. G., Klessen, R. S., Beck, R., & Spaans, M. 2010, A&A, 522, A115
Schlickeiser, R. 2002, Cosmic Ray Astrophysics (Berlin: Springer-Verlag)
Schmidt, M. 1963, Nature, 197, 1040
Schnitzeler, D. H. F. M. 2010, MNRAS, 409, L99
Schnitzeler, D. H. F. M. 2012, MNRAS, 427, 664
Serabyn, E., & Gusten, R. 1991, A&A, 242, 376
She, Z., & Leveque, E. 1994, Phys. Res. Lett., 72, 336
Shibata, M., & Sekiguchi, Y.-I. 2005, Phys. Rev. D, 72, 044014
Shibata, K., & Uchida, Y. 1987, PASJ, 39, 559
Shiromoto, Y., Susa, H., & Hosokawa, T. 2014, ApJ, 782, 108
Shulevski, A., et al. 2015, A&A, 579, A27
Sikora, M., Begelman, M. C., Madejski, G. M., & Lasota, J.-P. 2005, ApJ, 625, 72
Silant'ev, N. A., Gnedin, Y. N., Buliga, S. D., Piotrovich, M. Y., & Natsvlishvili, T. M. 2013, Astrophys. Bull., 68, 14
Simard-Normandin, M., & Kronberg, P. P. 1980, ApJ, 242, 74
Simonetti, J. H., Cordes, J. M., & Spangler, S. R. 1984, ApJ, 284, 126
Skilling, J. 1975, MNRAS, 173, 255
Smith, J. E., Young, S., Robinson, A., Corbett, E. A., Giannuzzo, M. E., Axon, D. J., & Hough, J. H. 2002, MNRAS, 335, 773
Sofue, Y. 1989, in IAU Symp. 136, The Center of the Galaxy, ed. M. Morris (Dordrecht: Kluwer Academic Publishers), 213
Sofue, Y. 2017, Galactic Radio Astronomy (Singapore: Springer Nature), ch. 6
Sofue, Y., & Fujimoto, M. 1983, ApJ, 265, 722
Sofue, Y., Fujimoto, M., & Wielebinski, R. 1986, ARA&A, 24, 459
Sofue, Y., & Handa, T. 1984, Nature, 310, 568
Sofue, Y., Machida, M., & Kudoh, T. 2010, PASJ, 62, 1191
Sofue, Y., & Nakanishi, H. 2017, MNRAS, 464, 783
Sofue, Y., Reich, W., Inoue, M., & Seiradakis, J. H. 1987, PASJ, 39, 95
Sofue, Y., & Takano, T. 1981, PASJ, 33, 47
Sofue, Y., Takano, T., & Fujimoto, M. 1980, A&A, 91, 335
Sofue, Y., Wakamatsu, K.-I., & Malin, D. F. 1994, AJ, 108, 2102
Sokoloff, D. D., Bykov, A. A., Shukurov, A., Berkhuijsen, E. M., Beck, R., & Poezd, A. D. 1998, MNRAS, 299, 189

Stasyszyn, F., Nuza, S. E., Dolag, K., Beck, R., & Donnert, J. 2010, MNRAS, 408, 684
Stepanov, R., Arshakian, T. G., Beck, R., Frick, P., & Krause, M. 2008, A&A, 480, 45
Stepanov, R., Shukurov, A., Fletcher, A., Beck, R., La Porta, L., & Tabatabaei, F. 2014, MNRAS, 437, 2201
Stil, J. M., Keller, B. W., Geoge, S. J., & Taylor, A. R. 2014, ApJ, 787, 99
Stil, J. M., Taylor, A. R., & Sunstrum, C. 2011, ApJ, 726, 4
Stone, J. M., Gardiner, T. A., Teuben, P., Hawley, J. F., & Simon, J. B. 2008, ApJS, 178, 137
Stone, J. M., & Norman, M. L. 1992, ApJS, 80, 791
Stroe, A., et al. 2016, MNRAS, 455, 2402
Stroe, A., van Weeren, R. J., Intema, H. T., Röttgering, H. J. A., Brüggen, M., & Hoeft, M. 2013, A&A, 555, 110
Strom, R. G., & Jaegers, W. J. 1988, A&A, 194, 79
Subramanian, K. 2016, Rep. Prog. Phys., 79, 076901
Subramanian, K., & Barrow, J. D. 1998, Phys. Rev. D, 58, 083502
Sugawara, C., Takizawa, M., & Nakazawa, K. 2009, PASJ, 61, 1293
Sun, X. H., et al. 2015a, AJ, 149, 60
Sun, X. H., et al. 2015b, ApJ, 811, 40
Sun, X. H., Han, J. I., Reich, W., Reich, P., Shi, W. B., Wielebinski, R., & Fürst, E. 2007, A&A, 463, 993
Sun, X. H., & Reich, W. 2009, A&A, 507, 1087
Sun, X. H., & Reich, W. 2010, Res. Astron. Astrophys., 10, 1287
Sun, X. H., Reich, W., Waelkens, A., & Enßlin, T. A. 2008, A&A, 477, 573
Suyama, T., & Yokoyama, J. 2012, Phys. Rev. D, 86, 023512
Takahashi, H. R., Ohsuga, K., Kawashima, T., & Sekiguchi, Y. 2016, ApJ, 826, 23
Takahashi, K., et al. 2009, PASJ, 61, 957
Takahashi, K., Ichiki, K., Ohno, H., & Hanayama, H. 2005, Phys. Rev. Lett., 95, 121301
Takahashi, K., Mori, M., Ichiki, K., & Inoue, S. 2012, ApJ, 744, L7
Takami, H., & Sato, K. 2010, ApJ, 724, 1456
Takizawa, M. 2008, ApJ, 687, 951
Takizawa, M., & Naito, T. 2000, ApJ, 535, 586
Tanaka, S. J., & Takahara, F. 2010, ApJ, 715, 1248
Taylor, A. R., Stil, J. M., & Sunstrum, C. 2009, ApJ, 702, 1230
Taylor, G. B., Perley, R. A., Inoue, M., Kato, T., Tabara, H., & Aizu, K. 1990, ApJ, 360, 41
Taylor, R., et al. 2015, in Proc. Advancing Astrophysics with the Square Kilometre Array, ed. T. L. Bourke et al. (Trieste: SISSA), 113
Tegmark, M., et al. 2006, Phys. Rev. D, 74, 123507
Thomson, R. C., & Nelson, A. H. 1980, MNRAS, 191, 863
Toma, K., & Takahara, F. 2012, ApJ, 754, 148
Tombesi, F., Cappi, M., Reeves, J. N., Palumbo, G. G. C., Yaqoob, T., Braito, V., & Dadina, M. 2010, A&A, 521, A57
Tomisaka, K. 2002, ApJ, 575, 306
Torii, K., et al. 2010, PASJ, 62, 675
Tosa, M., & Fujimoto, M. 1978, PASJ, 30, 315
Tribble, P. C. 1991, MNRAS, 250, 726
Troland, T. H., & Crutcher, R. M. 2008, ApJ, 680, 457
Tsuboi, M., et al. 2015, ApJ, 798, L6
Tsuboi, M., Inoue, M., Handa, T., Tabara, H., Kato, T., Sofue, Y., & Kaifu, N. 1986, AJ, 92, 818
Turner, M. S., & Widrow, L. M. 1988, Phys. Rev. D, 37, 2743
Turner, N. J. 2004, ApJ, 605, L45
Uchida, Y., & Shibata, K. 1984, PASJ, 36, 105
Uchida, Y., & Shibata, K. 1985, PASJ, 37, 515
Uchida, Y., Sofue, Y., & Shibata, K. 1985, Nature, 317, 699
Uchiyama, Y., Aharonian, F. A., Tanaka, T., Takahashi, T., & Maeda, Y. 2007, Nature, 449, 576
Ugai, M., & Tsuda, T. 1977, J. Plasma Phys., 17, 337
Uyaniker, B., Kothes, R., & Brunt, C. M. 2002, ApJ, 565, 1022
Vacca, V., et al. 2016, A&A, 591, A13
Vacca, V., Murgia, M., Govoni, F., Feretti, L., Giovannini, G., Perley, R. A., & Taylor, G. B. 2012, A&A, 540, A38
Vachaspati, T. 1991, Phys. Lett. B, 265, 258
Vallée, J. P. 2005, ApJ, 619, 297
Vallée, J. P. 2008, ApJ, 681, 303
Vallée, J. P., MacLeod, M. J., & Broten, N. W. 1986, A&A, 156, 386
Van Eck, C. L., et al. 2011, ApJ, 728, 97
van Weeren, R. J., Röttgering, H. J. A., Brüggen, M., & Hoeft, M. 2010, Science, 330, 347
van Weeren, R. J., Röttgering, H. J. A., Intema, H. T., Rudnick, L., Brüggen, M., Hoeft, M., & Oonk, J. B. R. 2012, A&A, 546, 124
Vazza, F., Brüggen, M., Wittor, D., Gheller, C., Eckert, D., & Stubbe, M. 2016, MNRAS, 459, 70
Vazza, F., Brunetti, G., Brüggen, M., & Bonafede, A. 2017, MNRAS, in press (arXiv:1711.02673)
Vazza, F., Brunetti, G., & Gheller, C. 2009, MNRAS, 395, 1333
Vazza, F., Brunetti, G., Gheller, C., Brunino, R., & Brüggen, M. 2011, A&A, 529, 17
Vernstrom, T., Gaensler, B. M., Brown, S., Lenc, E., & Norris, R. P. 2017, MNRAS, 467, 4914
Voelk, H. J. 1989, A&A, 218, 67
Vogt, C., & Enßlin, T. A. 2003, A&A, 412, 373
Völk, H. J., & Atoyan, A. M. 2000, ApJ, 541, 88
Vollmer, B., Soida, M., Beck, R., Chung, A., Urbanik, M., Chyży, K. T., Otmianowska-Mazur, K., & Kenney, J. D. P. 2013, A&A, 553, A116
Waelkens, A., Jaffe, T., Reinecke, M., Kitaura, F. S., & Enßlin, T. A. 2009, A&A, 495, 697
West, J. L., Safi-Harb, S., Jaffe, T., Kothes, R., Landecker, T. L., & Foster, T. 2016, A&A, 587, 148
Weymann, R. J., Morris, S. L., Foltz, C. B., & Hewett, P. C. 1991, ApJ, 373, 23
Weżgowiec, M., Urbanik, M., Beck, R., Chyży, K. T., & Soida, M. 2012, A&A, 545, 69
Widrow, L. M., Ryu, D., Schleicher, D. R. G., Subramanian, K., Tsagas, C. G., & Treumann, R. A., 2012, Space Sci. Rev., 166, 37
Wik, D. R., Sarazin, C. L., Finoguenov, A., Matsushita, K., Nakazawa, K., & Clarke, T. E. 2009, ApJ, 696, 1700
Wilson, A. S., & Weiler, K. W. 1976, A&A, 53, 89
Xu, H., et al. 2012, ApJ, 759, 40
Xu, H., Li, H., Collins, D. C., Li, S., & Norman, M. L. 2009, ApJ, 698, L14
Xu, J., & Han, J. L. 2014, MNRAS, 442, 3329
Yamazaki, D. G. 2014, Phys. Rev. D, 89, 083528
Yamazaki, D. G. 2016, Phys. Rev. D, 93, 043004
Yamazaki, D. G., Ichiki, K., & Kajino, T. 2005, ApJ, 625, L1

Yamazaki, D. G., Ichiki, K., Kajino, T., & Mathews, G. J. 2006a, ApJ, 646, 719
Yamazaki, D. G., Ichiki, K., Kajino, T., & Mathews, G. J. 2008, Phys. Rev. D, 77, 043005
Yamazaki, D. G., Ichiki, K., Kajino, T., & Mathews, G. J. 2010, Phys. Rev. D, 81, 023008
Yamazaki, D. G., Ichiki, K., & Takahashi, K. 2011, Phys. Rev. D, 84, 123006
Yamazaki, D. G., Ichiki, K., Umezu, K., & Hanayama, H. 2006b, Phys. Rev. D, 74, 123518
Yamazaki, D. G., Kajino, T., Mathews, G. J., & Ichiki, K. 2012, Phys. Rep., 517, 141
Yamazaki, D. G., & Kusakabe, M. 2012, Phys. Rev. D, 86, 123006
Yamazaki, D. G., Kusakabe, M., Kajino, T., Mathews, G. J., & Cheoun, M. K. 2014, Phys. Rev. D, 90, 023001
Yusef-Zadeh, F. 1986, PhD thesis, Columbia University
Yusef-Zadeh, F., & Morris, M. 1988, ApJ, 329, 729
Yusef-Zadeh, F., Morris, M., & Chance, D. 1984, Nature, 310, 557
Zhang, J., Lazarian, A., Lee, H., & Cho, J. 2016, ApJ, 825, 154
Zhu, G., & Ménard, B. 2013, ApJ, 770, 130
ZuHone, J. A., Markevitch, M., Brunetti, G., & Giacintucci, S. 2013, ApJ, 762, 78